Design of antenna-coupled lumped-element titanium nitride KIDs for long-wavelength multi-band continuum imaging

Thesis by

Chenguang Ji

In Partial Fulfillment of the Requirements

for the Degree of

Doctor of Philosophy

California Institute of Technology

Pasadena, California

2015

(Defended May 18th, 2015)

Dedicated to everyone who accompanied me through the ups and downs along the way

Acknowledgments

First and foremost I would like to express the deepest gratitude to my advisor, Sunil Golwala. Thank you for creating such a relaxed and positive atmosphere to discuss science and for granting me the freedom to pursue my interest in research. I have great appreciation for your unfailing encouragement during the many hardships and respect for your perseverance and tenacity for leading our project through the tough times.

I am also extremely grateful to Jonas Zmuidzinas. Jonas introduced me the TLS noise project in late 2012 and we had a series of very interesting talks since then despite his heavy obligation at JPL. Also, as the founder of MKID, Jonas provided me with critical comments on the LWCam design work at different stages.

I am really thankful to David Rutledge, Bill Johnson, and Bill Goddard for serving on my thesis defense committee and the valuable comments from an interdisciplinary perspective.

I am very fortunate to have been working in a highly supportive environment in the submillimeter/millimeter observational astronomy group. Chris McKinney, back then, was one of Jonas' postdocs working on another subproject MAKO for CCAT. We got paired up to experimentally determine the TLS noise properties in the parallel-plate structure MKID. Chris turned out to be an amazing mentor and I benefited so much by working closely with such an enthusiastic and excellent experimentalist. I was also later granted with the privilege to use his privately (and secretly) owned drills. Erik Shirokoff, another postdoc working on Superspec, has always been very patient in listening to my problems with Sonnet simulation and good at suggesting smart solutions. Matt Hollister, the mechanical engineer, successfully maintained the old blue dewar to work for the hot/cold measurement on the antenna. Mark Gonzales, the shop course instructor, taught me the "nice and easy" machining skills hand by hand meticulously. Andrew Beyer, our collaborator at JPL, fabricated the device for LWCam. Seth Siegel, my fellow graduate student, shared with me his powerful MCMC code for detector efficiency characterization. Bade Uzgil, my officemate, said hello to me everyday with a bright smile. Albert Lam, an undergraduate, renovated the dewar and took turns with me to

do the refills and never complained. Ran Duan, a senior graduate student, helped me to ease into the role during my early stage of research. I am also indebted to Jiansong Gao, a previous graduate student of the group. Though we only got the chance to chat over the phone, Jiansong gave me lots of sincere advices. He is also the person who laid the groundbreaking foundation work about MKID TLS noise theory, the basis of Chapter 2 of this thesis.

Among the many courses I took over the years at Caltech, some made a huge impact on me. Thanks to these outstanding lecturers. You not only transfered knowledge and skills but also imparted wisdom, fostered the passion for science and changed my way of thinking. They are Brent Fultz, Sossina Haile, Matthew Fisher, Sergei Gukov, and Alexei Kitaev.

During my PhD I've also been teaching undergraduate courses as an assistant and meet a few fantastic persons. Thanks Jessica Hsu, Julia Su, and Pinting Chen for being my faithful (and amazing) audiences in physics 2 a and b at Caltech. It was a very delighted experience to have you all as my students. Thanks Frank Rice for being such an awesome leader in physics 6 and 7. As somebody who is witty, remarkably fond of his job, and professional in detail, you left a very deep impression on me. Thanks Rebecca Wernis, Daniel DeFelippis, and Nico Salzetta. I greatly enjoyed your partnership.

I also want to mention some of my best friends who make my Caltech life fun and unforgettable. They are Ding Ding, Yinglu Tang, Xiaowei Deng, Jing Zhang, Jonathan Hood, Andres Goza, and the whole 2009 class of Caltech C members. I will cherish the friendship I have with you all.

Lastly I would like to thank my parents and members in my extended family. Thank you for always being with me in such a long journey. Without your sacrifice and unconditional love, this thesis would never be possible.

Abstract

Many applications in cosmology and astrophysics at millimeter wavelengths including CMB polarization, studies of galaxy clusters using the Sunyaev-Zeldovich effect (SZE), and studies of star formation at high redshift and in our local universe and our galaxy, require large-format arrays of millimeter-wave detectors. Feedhorn and phased-array antenna architectures for receiving mm-wave light present numerous advantages for control of systematics, for simultaneous coverage of both polarizations and/or multiple spectral bands, and for preserving the coherent nature of the incoming light. This enables the application of many traditional "RF" structures such as hybrids, switches, and lumped-element or microstrip band-defining filters.

Simultaneously, kinetic inductance detectors (KIDs) using high-resistivity materials like titanium nitride are an attractive sensor option for large-format arrays because they are highly multiplexable and because they can have sensitivities reaching the condition of background-limited detection. A KID is a LC resonator. Its inductance includes the geometric inductance and kinetic inductance of the inductor in the superconducting phase. A photon absorbed by the superconductor breaks a Cooper pair into normal-state electrons and perturbs its kinetic inductance, rendering it a detector of light. The responsivity of KID is given by the fractional frequency shift of the LC resonator per unit optical power.

However, coupling these types of optical reception elements to KIDs is a challenge because of the impedance mismatch between the microstrip transmission line exiting these architectures and the high resistivity of titanium nitride. Mitigating direct absorption of light through free space coupling to the inductor of KID is another challenge. We present a detailed titanium nitride KID design that addresses these challenges. The KID inductor is capacitively coupled to the microstrip in such a way as to form a lossy termination without creating an impedance mismatch. A parallel-plate capacitor design mitigates direct absorption, uses hydrogenated amorphous silicon, and yields acceptable noise. We show that the optimized design can yield expected sensitivities very close to the fundamental limit for a long wavelength imager (LWCam) that covers six spectral bands from

90 to 400 GHz for SZE studies.

Excess phase (frequency) noise has been observed in KID and is very likely caused by two-level systems (TLS) in dielectric materials. The TLS hypothesis is supported by the measured dependence of the noise on resonator internal power and temperature. However, there is still a lack of a unified microscopic theory which can quantitatively model the properties of the TLS noise. In this thesis we derive the noise power spectral density due to the coupling of TLS with phonon bath based on an existing model and compare the theoretical predictions about power and temperature dependences with experimental data. We discuss the limitation of such a model and propose the direction for future study.

Contents

List of Figures

List of Tables

Chapter 1

Background

1.1 Scientific Motivation

1.1.1 Introduction to mm/submm astrophysics

Most of the submillimeter- and millimeter- wave photons in the universe are emitted by the dense interstellar gases and dusts, which are the "cradles" of new stars[1]. Interestingly, these interstellar materials are almost transparent to the sub/millimeter waves, but many orders more opaque for the optical wave bands. Therefore the sub/millimeter wave astronomy is an important platform to study star and galaxy formations.

Deep surveys at sub/millimeter wavelengths also make it possible to study the characteristics of galaxies as a function of the red shift. Figure 1.1 shows a typical spectra of emission from the galaxies. The discovery that the radiation intensity is a fast increasing function of frequency at sub/millimeter wavelength ($\sim$200-1000 μm) establishes the fact that the flux intensity of emission from a galaxy measured in this wave band is almost independent of the redshift, which is considerably different from other wavelengths and opens up the possibility of discovering and studying very distant galaxies.

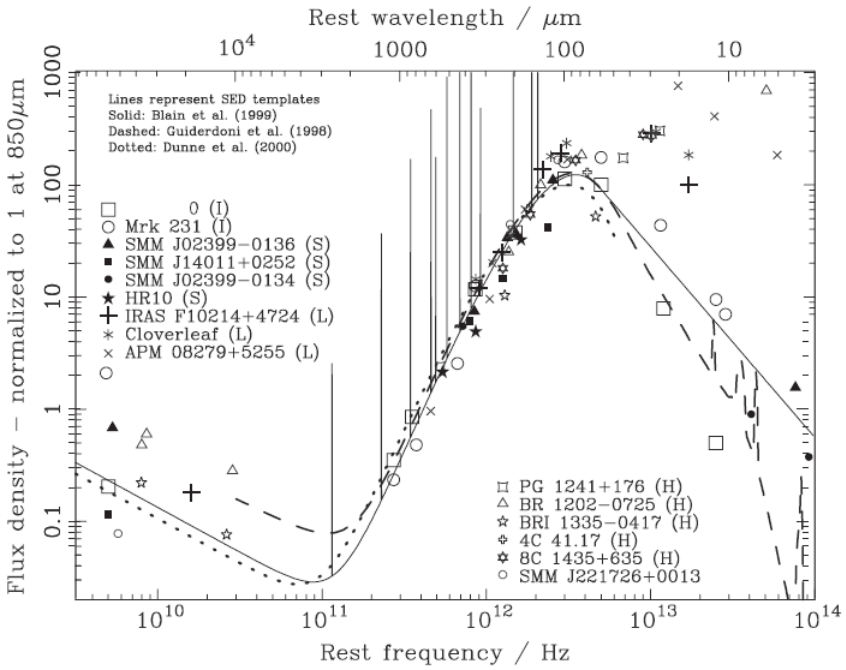

Figure 1.1: Typical (normalized) spectra of galaxy emission at frequencies from the radio to IR wave bands[2].

Moreover, observations at sub/millimeter wavelengths provide important information about CMB physics. The cosmic microwave background (CMB), which peaks at 2 mm, is the thermal radiation left over from the Big Bang of the universe. The tiny anisotropy or temperature fluctuation corresponds to regions of slightly different densities, which evolved into the stars and galaxies of today. Study of CMB physics provides a crucial test of the cosmological models.

Another important application of sub/millimeter wave astronomy is through the Sunyaev-Zeldovich effect (SZE). SZE states that the CMB photons are inverse Compton scattered to high energy state when interacting with hot electron gases, resulting in a decrease in the CMB intensity below 218 GHz and a corresponding increase at higher frequencies. This phenomenon is shown in Figure 1.2. The SZE consists of the thermal component, kinetic correction, and relativistic correction. The kinetic component of SZE is due to the relative motion of the cluster with respect to the rest frame of the CMB, so it can provide measurements of cluster peculiar velocities. The thermal SZ spectrum is temperature-independent in non-relativistic limit (only the amplitude depends on temperature), but relativistic correction makes its shape temperature dependent. The relativistic SZE correction therefore provides measurements of cluster temperature.

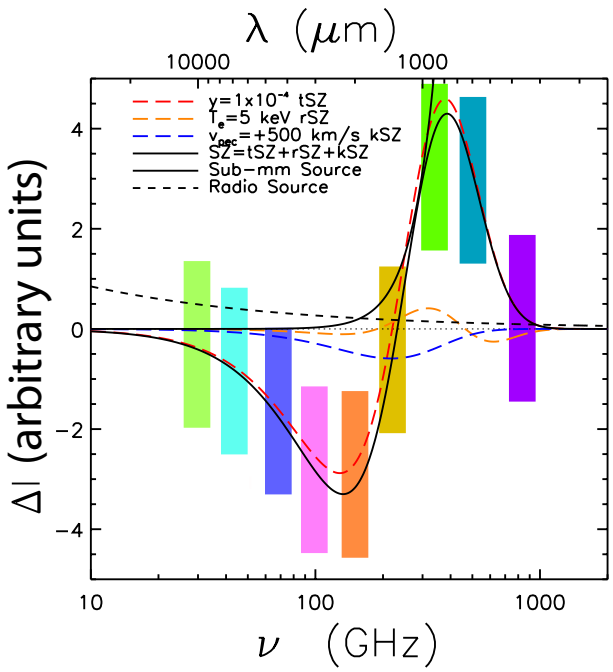

Figure 1.2: Thermal SZE model spectra (dashed red line) (credit to Mike Zemcov) with y=1×10^{-4}. The Kompaneets y parameter is defined as $y = \tau \times (k_B T/mc^2)$, where τ is the optical depth or the fraction of photons scattered and $(k_B T/mc^2)$ is the electron temperature in unit of the rest mass of the electron. Also shown is the distorted spectrum (solid black line) after the addition of relativistic corrections with $T_e = 5$ keV (dashed orange line), and kinetic SZE corrections with v_{pec}=+500 km/s (dashed blue line). The sub-mm source line (another solid black line) refers to the typical spectrum of the dust-obscured galaxies. The radio source line (dashed black line) refers to the galaxies that are bright at radio wavelengths, due usually to large amounts of synchrotron radiation from electrons accelerated by energetic phenomena like shock waves and active galactic nuclei (super massive black holes at the centers of galaxies). The color bars refer to typical spectral bands based on the atmospheric transmission windows.

1.1.2 Scientific motivation of long wavelength imager

We propose a design study for the long-wavelength imager for Cerro Chajnantor Atacama Telescope (CCAT): LWCam. CCAT is a 25 meter telescope at an excellent cite in Chile and would be one of the highest permanent, ground-based telescopes in the world. LWCam will cover a 20′ field-of-view in six spectral bands (required for subtraction of radio and mm/submm galaxy foregrounds) from 0.75 to 3.3 mm. The six bands are expected to have 14080, 14080, 3520, 3520, 880, and 880 pixels with per-pixel sensitivities of 5.9, 3.7, 1.6, 1.8, 1.7, 1.8 mJy $s^{1/2}$. The fine angular resolution (0.24′ at 1.1 mm), wide field-of-view, broad spectral coverage, and large mapping speed of LWCam will enable a variety of scientific studies, including the dusty star-forming galaxy (DSFG) population and the intra-cluster medium (ICM) in galaxy clusters.

The dusty star-forming galaxy population plays a crucial role in galaxy evolution over cosmic

time. It is known that the flux ratio of wavelengths 350 μm to 850 μm S_{350}/S_{850} drops from 4-7 at z (redshift)$\sim$2 to 2-4 at z$\sim$4 and 1-2 at z$\sim$6. Therefore only with the 850 μm data from LWCam, low-luminosity z$\sim$2 DSFG, and ultra-luminous higher-z sources can be distinguished. Also, the large pixel counts and high mapping speed of LWCam would yield thousands of z>4 DSFG and enable the first measurement of high-z clustering, which is to be compared with strong clustering of lower z-DSFG, and hundreds of z>5 DSFGs that can connect the epoch of dusty star formation with the end of re-ionization. Finally, the multiple spectral bands of LWCam provide approximate redshift information and probe the highest redshifts that can most incisively test models of galaxy formation because of the wavelength-dependent nature of the emissivity history, as shown in Figure 1.3. Note that those sources are so optically obscured that one cannot obtain the redshift by optical spectroscopy. Submm spectroscopy is quite difficult though, and it is only possible with the Atacama Large Millimeter/submillimeter Array (ALMA) and on small samples of sources so far.

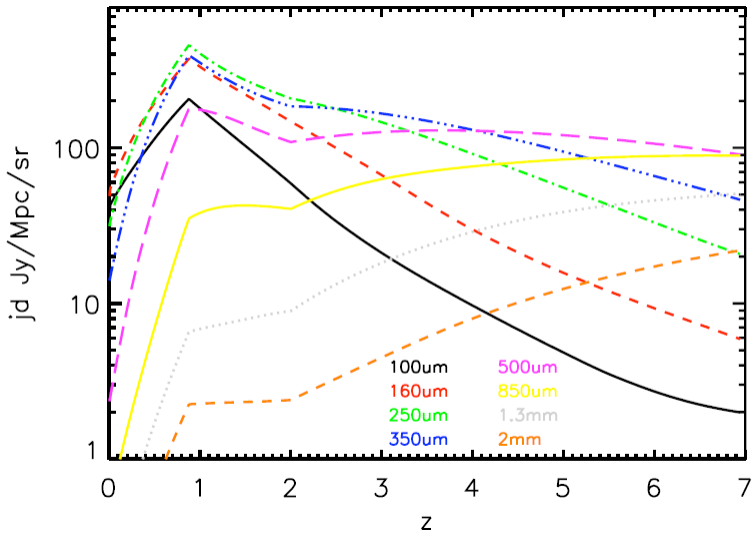

Figure 1.3: The emissivity history of the universe as a function of redshift at a range of wavelengths[4].

Imaging in multiple spectral bands in the 80-420 GHz (0.715 to 3.75 mm) range will also enable new studies of the ICM in galaxy clusters via SZ effects, specifically the mapping of thermal and non-thermal pressure using the thermal SZ effect, the detection and study of high temperature regions using its relativistic corrections, and the study of unvirialized bulk velocities in the ICM and the peculiar motions of entire galaxy clusters using the kinetic SZ effect.

1.2 Review of light-coupling architectures

In this section we consider the way in which the mm/submm radiation described in the previous section can be coupled to the detectors. Among the many existing coupling architectures (direct absorption, lens-coupled dual-slot-dipole antenna, sinuous antenna, etc.), we will briefly review feed-horn and phased-array antenna.

1.2.1 Feedhorn

A horn antenna is an antenna consisting of a flaring structure that directs the waves in a beam. The smooth-walled horn can accommodate a wide spectrum of signals since it does not contain any resonant elements. Horns have the advantages of moderate directivity, simple construction, and adjustment. The different flare angles and expansion curves also make possible a variety of different beam profiles. The common types of horns include pyramidal horns, sectoral horns, conical horns, exponential horns, and corrugated horns. Figure 1.4 shows a picture of a corrugated horn. There are two techniques for the horn to couple light to the detector: direct absorption and microstrip coupling. In the direct absorption scheme the absorber/detector is placed in a cavity behind the horn. In the microstrip coupling scheme, waveguide probes are placed at the output of the horn and connect to the microstrip that terminates in a detector.

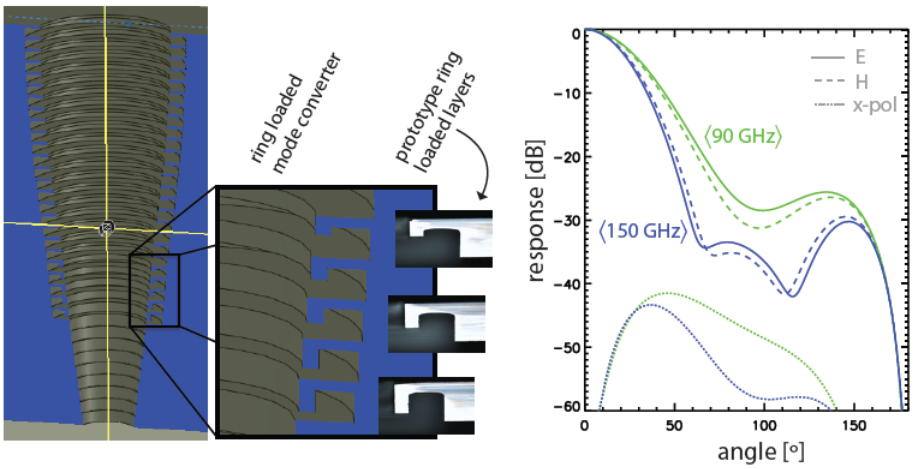

Figure 1.4: Left: A drawing of a preliminary horn design incorporating ring loaded slots[5]. The zoom shows the geometry of the ring-loaded grooves more clearly. Three photographs show prototype layers etched using a three layer mask and a deep reactive ion-etch (DRIE) machine. Right: The predicted band-averaged beam pattern in both the 90 and 150 GHz bands. These patterns were constructed by simulating the beam pattern at 5 GHz increments and averaging these results within the predicted detector passband. These simulations show the input reflection to be below -20 dB and the cross-polarization below -30 dB across both bands.

1.2.2 Phased array antenna

A phased array antenna is an array of antenna, the signal phases of which are varied spatially so that the combined radiation pattern is reinforced in one direction and suppressed in other directions. There are dual-polarization single band designs and single-polarization multi-band designs. In both cases, the light is received through the silicon substrate. The advantages of phased array antenna include great directivity and excellent steering ability. Figure 1.5 (Left) shows an array of single-scale slot antennas.

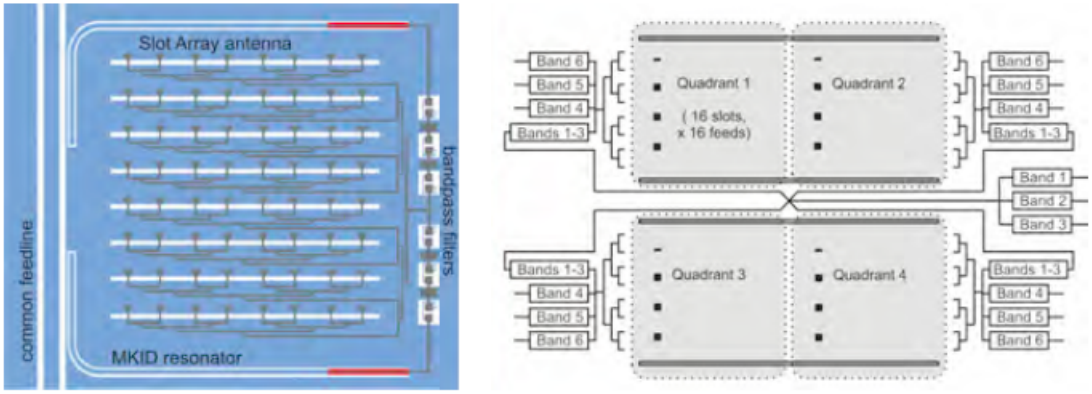

Figure 1.5: Left: schematic layout of single-scale phased-array antenna array showing slot dipoles, taps, summing tree, bandpass filters, and coplanar waveguide microwave kinetic inductance detectors. Right: conceptual design of multi-scale phased array.

A multi-scale phased array antenna as shown in Figure 1.5 (Right) is an extension of the above mentioned single-scale phased array antenna. To match the pixel size to the wavelength, larger pixels at longer wavelengths can be synthesized from the smaller pixels matched to the shortest wavelengths. For LWCam, it would be optimal to have three scales of pixel size to ensure good Airy function matching. The bandwidth of the antenna is set by the feed density (smallest wavelength) and the slot length (largest wavelength). The width of the microstrip at the slots is about 1 μm to match the slot impedance. The width expands in the summing tree (not trivially: every summing junction doubles the width, but then it is tapered back down before the next summing junction so that the tree does not get too wide). The microstrip transmission line at the output of the antenna is 4 μm wide.

LWCam will use multi-scale phased array antenna for the following reasons.

- The phased array can be fabricated on the same substrate as the detectors so that a separate light coupling structure is not required.

- One can cover many spectral bands with the same focal plane because the array can be designed to have a very broad intrinsic bandwidth (up to 10:1).

1.3 Introduction to kinetic inductance detector

Light received at the antenna is transferred to the photon detector. The design of LWCam is based on the concept of the kinetic inductance detector (KID) due to the excellent multiplexability, which motivates their use in applications that require a large arrays of detectors. In this section we will review KID's principles of operation, limiting factors of sensitivity, and applications.

1.3.1 Principles of operation

Superconductors have zero dc resistance below the transition temperature T_c. At absolute zero temperature electrons in the superconducting phase stay in the form of Cooper pairs with a bonding energy 2Δ via phonon mediated attractive interaction. The Cooper pairs accelerate under an external electric field like free electrons and acquire a kinetic energy. Such an energy can be retrieved by reversing the direction of the electric field. Therefore the exchange between electron kinetic energy and the electromagnetic energy induces a reactive impedance for an ac field, called the kinetic inductance L_k. On the other hand, the excitations of the BCS ground state, the quasiparticles, experience dissipation as normal-state electrons, resulting in a real part of the impedance.

The superconductor can be engineered to form the inductor of a LC resonator, whose resonant frequency f_0 and quality factor Q_r are determined by the ac impedance Z. When a photon with sufficient energy $h\nu > 2\Delta$ is absorbed by the superconductor, Cooper pairs will be broken and quasiparticles are created, altering both the imaginary and real parts of the impedance. The change δZ is therefore translated into a shift δf_0 and δQ_r, which can be read out by examining the transmission of the probe signal (normally in the microwave band). Such a photon detector is called the kinetic inductance detector (KID)[6].

The most attractive part of KID is its multiplexing ability. The traditional cryogenic detectors like transition-edge sensor are generally used with individual preamplifiers and wiring for the output. Multiplexing schemes have been developed along the way but require complex, custom-designed superconducting electronics, located close to the detector array. In contrast, KID allows a straightforward frequency domain approach to multiplexing. This results in a dramatic simplification of the detector arrays and the associated cryogenic electronics, making it possible to produce a large

format array involving thousands of detectors.

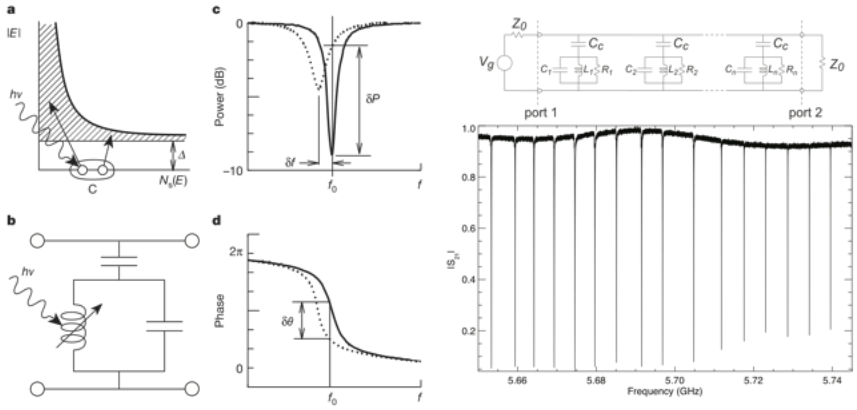

Figure 1.6: Left: The basic operation of a KID[6]. (a) Photons with energy $h\nu$ are absorbed in a superconducting film, producing a number of excitations, called quasiparticles. (b) To sensitively measure these quasiparticles, the film is placed in a high frequency planar resonant circuit. (c) The increase in the kinetic inductance and surface resistance of the film following a photon absorption event pushes the resonance to lower frequency and changes its amplitude. (d) If the detector (resonator) is excited with a constant on-resonance microwave signal, the energy of the absorbed photon can be determined by measuring the degree of phase and amplitude shift. Right: An example of frequency domain multiplexed (FDM) KIDs.

1.3.2 Sensitivity

There are generally four types of noises in the kinetic inductance detectors[7, 8]. The first is the photon noise. The incident millimeter wave photons from the background (dewar, telescope, and sky) obey Bose-Einstein statistics and have an intrinsic fluctuation in each mode. The second is the quasiparticle generation-recombination noise. In the steady state under optical loading the detector maintains a dynamic equilibrium of the quasiparticles. The quasiparticles can recombine to emit phonons, which is a point Poisson process and induces the fluctuation in quasiparticle density and recombination noise. The reverse process, in which thermal phonons break Cooper pairs, gives the generation noise. The first two types of noise are called fundamental noise. The third is the amplifier noise. KID uses a cryogenic low noise amplifier, either a high-electron-mobility transistor (HEMT) or a silicon-germanium bipolar-junction transistor (BJT), to amplify the transmitted signal. The amplifier adds voltage fluctuations to the probe signal when amplifying it, which is usually characterized by a noise temperature of a few Kelvin. The fourth is the two-level-system (TLS) noise. There exist extensively the two-level states in amorphous materials, which respond to the external field and contribute to the dielectric constant. A certain mechanism regarding the TLS, which is conjectured to be TLS-TLS interaction in the most recent studies[11, 12, 13], causes the fluctuation in the corresponding dielectric constant and leads to a jittering of KID's resonant frequency[9]. Since

we are interested in the noise in the measurement of the incoming optical power, we convert all these four types of noises to"noise-equivalent power" (NEP) or the effective noise on the incoming power measurement due to each noise component, so that they can be compared with each other. Our goal is to make the amplifier noise and TLS noise subdominant to the fundamental noise. Experiments have shown that the amplifier noise can be well suppressed by using a strong probe signal. So the difficult part is the TLS noise. Various methods have been developed along the way for its reduction[10].

Initially, KIDs were fabricated from aluminium since it is a simple, well-behaved, and easy-to-fabricate superconductor. The kinetic inductance fraction of Al was low ($\sim 5\%$) and so was the responsivity, which led to the TLS noise that is substantially larger than fundamental noises in noise-equivalent power unit. While it became clear one could reduce TLS noise using large capacitors, this presented engineering challenges for detectors. So new materials were sought out that could offer a larger kinetic inductance signal. Recently titanium nitride (TiN) arises as an excellent candidate for KID materials since it promises greatly improved sensitivity relative to aluminum for a given resonator geometry as discussed in [31]. Specifically:

- The kinetic inductance of a superconductor is proportional to its normal-state resistivity. The highly resistive material TiN has a nearly unity kinetic inductance fraction α and leads to a lower resonant frequency f_0 for the resonator:

$$\alpha = \frac{L_k}{L_{tot}} = \frac{L_k}{L_k + L_g} \sim 1 \tag{1.1}$$

$$f_0 = (L_{tot}C)^{-1/2} = ((L_k + L_g)C)^{-1/2} \ll (L_g C)^{-1/2} \tag{1.2}$$

  where L_g is the geometric inductance which results from the magnetic energy stored in the structure. MKID's responsivity benefits from both the larger α and lower f_0[7], rendering TLS noise equivalent power much smaller for fixed resonator quality factor Q_r.

- TiN's high resistivity is a better match to the wave impedance of silicon $\sqrt{\mu/\epsilon_{Si}}$ than aluminum or other low resistivity materials, making it much easier to build free space coupled KID[15, 16].

Because of these advantages, this thesis focuses on a design for LWCam that uses TiN KIDs[1].

[1]It is worth pointing out that the metallic glass, for example NbSi[33], might be a better KID material than TiN. NbSi has a normal-state resistivity several times larger than TiN. NbSi can make perfect thin film down to 10 nm free of inhomogeneity (a common problem for TiN KID). The T_c is tunable: 15% silicon might reduce T_c down to 1 K. We use TiN since its fabrication and testing techniques had been mature at JPL when this design work was carried out.

1.3.3 Applications

The KID technology have been most intensively applied and tested in the area of sub/millimeter imaging. The multi-wavelength sub/millimeter inductance camera (MUSIC) is designed to have 2304 detectors in 576 spatial pixels and four spectral bands at 0.87, 1.04, 1.33, and 1.98 mm[14]. The KIDs are made of Al and operate at several GHz. MUSIC is used to to study dusty star-forming galaxies, galaxy clusters via the Sunyaev-Zeldovich effect and star formation in our own and nearby galaxies. MUSIC has been deployed since 2012 at Caltech Submillimeter Observatory (CSO). MAKO is a scalable 350 μm pathfinder instrument with a prototype of couple of hundreds of pixels[15, 16]. MAKO uses lumped element kinetic inductance detectors (LEKID) patterned from TiN films. The resonators are designed to operate at 100 MHz, which presents numerous advantages, including an improved pixel noise equivalent power, a simplified analog readout circuit, and a higher achievable multiplexing density. MAKO saw the first light in 2013 at CSO and reached the condition of photon-noise-limited detection in 2014. Superspec is a ultra-compact spectrometer-on-a-chip for high redshift observations[17, 18]. It applied the LEKID technology to R$\sim$500 spectrometers covering the 190-310 GHz band. Both MAKO and Superspec are originally proposed for CCAT too, aiming ultimately towards 10^6 detector arrays. KID is also under development for other applications such as optical/X-ray detection[19] and dark matter search[20, 21].

Chapter 2

Study of two-level-system noise in dielectric materials

In Chapter 1 we discussed the fact that TLS noise is an important contributor to total NEP for KIDs. While its behavior is by now well understood phenomenologically[8], providing engineering recipes for its minimization, a fundamental understanding of TLS noise is desirable. In this chapter we will first go through the experimentally established properties of TLS noise in KID and introduce the standard tunneling model that serves historically as the theoretical basis for the many TLS-relevant phenomenons. We will then relate the dielectric constant to the state of each individual TLS and derive an expression for its power spectral density (PSD). The evolution of individual TLS that takes into account of the interaction with the phonon bath is subsequently elaborated. Finally we carry out numerical analysis of the frequency dependence, power dependence, and temperature dependence of TLS frequency noise and compare it with the data.

2.1 General properties of TLS noise in KID

2.1.1 Noise measurement

A diagram of the experimental set-up for noise measurement in KID is shown in Figure 2.1. A synthesizer generates a microwave signal with frequency f as the probe. Part of the signal couples with KID in the fridge, gets amplified (by a HEMT and a room temperature amplifier), and feeds into the RF (radio frequency) port of an IQ mixer. The rest of the signal goes directly into the LO (local oscillator) port of the mixer. The output I and Q (audio frequency ports) voltages are proportional to the in-phase and in-quadrature amplitudes of the transmitted signal.

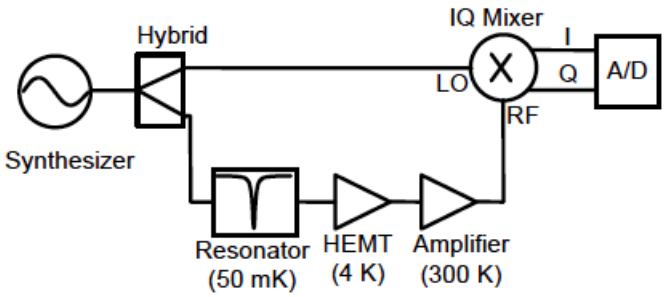

Figure 2.1: A diagram of the homodyne readout system used for the noise measurement.

When f is varied, the output $\xi = [I, Q]^T$ traces a circle in the 2D IQ plane called the resonance circle as shown in figure 2.2. With f fixed, ξ is seen to fluctuate around its mean and the fluctuations $\delta\xi(t) = [\delta I(t), \delta Q(t)]^T$ are digitized for noise analysis. $\delta\xi(t)$ can be projected onto two directions: the one that is tangent to the circle $\delta\xi_{\parallel}(t)$ and the one in the orthogonal direction $\delta\xi_{\perp}(t)$. $\delta\xi_{\parallel}(t)$ and $\delta\xi_{\perp}(t)$ correspond to the fluctuations of the phase and amplitude of the resonator's electric field $\vec{E}$. Their power spectral densities $S_{ff}(\nu)$ and $S_{aa}(\nu)$ are therefore measures of the phase (frequency) and amplitude noises in KID.

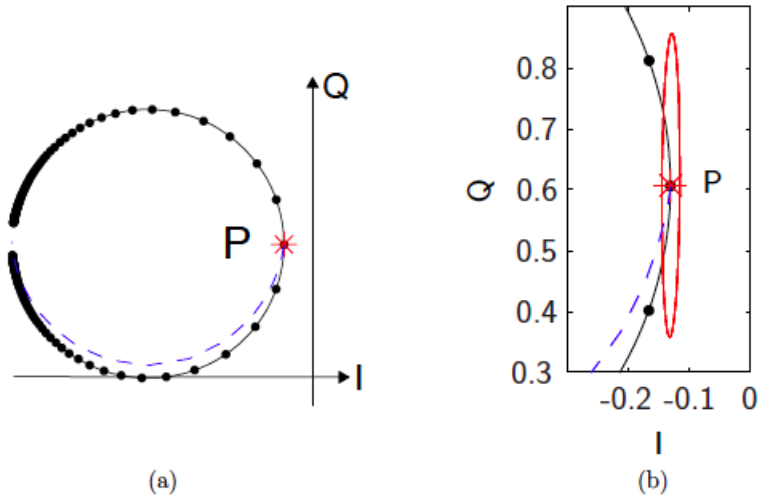

Figure 2.2: (a) Resonance circle of a 200 nm Nb on Si resonator at 120 mK (solid line)[8], quasiparticle trajectory calculated from the Mattis-Bardeen theory (dashed line). For this figure, the readout point $\xi = [I, Q]^T$ is located at the resonance frequency f_r. (b) Noise ellipse (magnified by a factor of 30). Other parameters are $f_r = 4.35$ GHz, $Q_r = 3.5 \times 10^5$ (coupling limited), readout power $P_r \approx$-84 dBm, and internal power $P_{int} \approx$-30 dBm.

2.1.2 Experimental results of TLS noise in KID

Experiments have revealed several characteristic properties of TLS noise in KID[27, 28, 29]: the frequency noise has a power law dependence on the noise frequency $S_{ff}(\nu) \sim \nu^{-1/2}$; the frequency noise has a power law dependence on the amplitude of the electric field $S_{ff}(\nu) \sim P_{int}^{-1/2} \sim |\vec{E}|^{-1}$; the frequency noise has a power law dependence on the temperature $S_{ff}(\nu) \sim T^{-2}$ for $T > 100$ mK; the frequency noise is several orders of magnitude stronger than the amplitude noise $S_{ff}(\nu) \gg S_{aa}(\nu)$. The data are shown in Figure 2.3 to Figure 2.5.

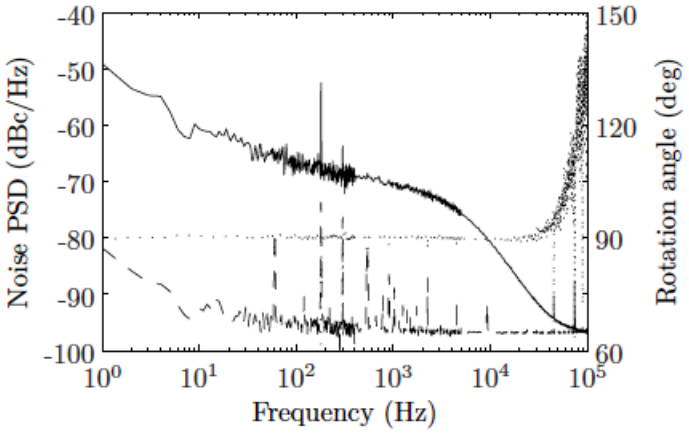

Figure 2.3: Noise spectra[8] of a 200 nm Nb on Si resonator at 120 mK in the phase (frequency) (solid line) and amplitude (dashed line) directions. Other parameters are $f_r = 4.35$ GHz, $Q_r = 3.5 \times 10^5$, readout power $P_r \approx -84$ dBm, and internal power $P_{int} \approx -30$ dBm.

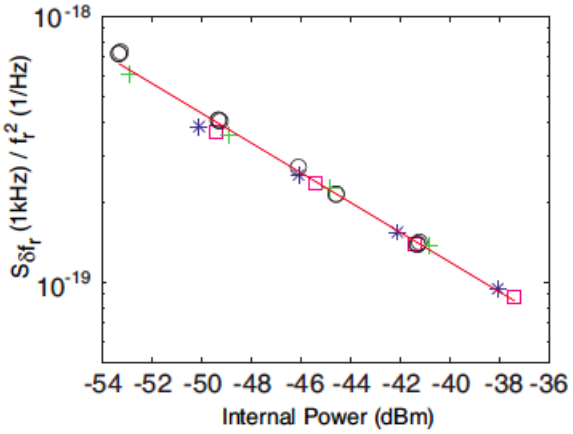

Figure 2.4: Frequency noise[8] at 1kHz $S_{\delta f_r}(1\text{kHz})/f_r^2$ vs. internal power P_{int} falls on to straight lines of slope -1/2 in the log-log plot, indicating a power law dependence: $S_{\delta f_r/f_r} \propto P_{int}^{-1/2}$. Data points marked "+", "□" and "*" indicate the on-resonance ($f = f_r$) noise of three different resonators (with different f_r and Q_r on the same chip) under four different readout power $P_{\mu\omega}$. Data points marked with "○" indicate the noise of resonator (marked with "*") measured at half-bandwidth away from the resonant frequency ($f = f_r \pm f_r/2Q_r$) under the same four $P_{\mu\omega}$. The data is measured from a 200 nm thick Al on sapphire device.

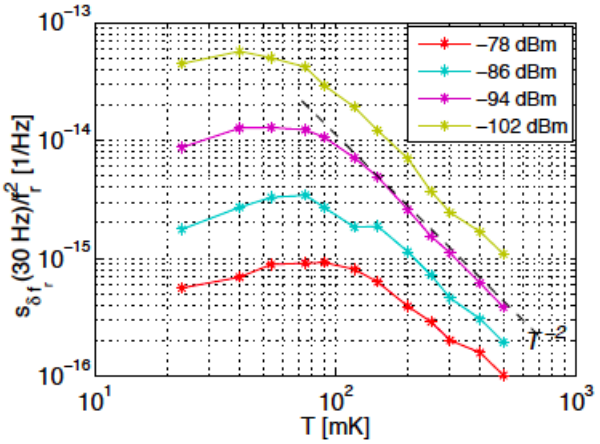

Figure 2.5: Frequency noise at 30 Hz as a function of temperature measured at P_{int}=-78, -86, -94, and -102 dBm from Nb on sapphire with SiO_2 dielectric microstrip device. At $T > 100$ mK, the noise roughly scales as T^{-2}.

2.2 Standard model of two level systems

With the goal of explaining the TLS noise observed in KIDs, we will develop a model for the fluctuations in the dielectric properties of a medium containing TLS and their impact on the resonator frequency and dissipation fluctuation spectra.

2.2.1 Localized representation and energy representation

Various experiments regarding the thermal properties and response to external electric field have shown that the glass can behave in a substantially different manner compared with perfect crystal at low temperature. The two-level-state tunneling model[22] was initially proposed in 1970s and subsequently achieved huge success in explaining the experimental results. Such a model postulates that a broad spectrum of two level systems extensively exists in glass, in which an atom or group of atoms can occupy one of the two potential minima. The Hamiltonian of the system can be conveniently expressed using the basis set ϕ_1 and ϕ_2 in the localized representation, where ϕ_1 and ϕ_2 are the ground state wave functions of the two adjacent potential wells:

$$H_0 = \frac{1}{2}\begin{pmatrix} -\Delta & \Delta_0 \\ \Delta_0 & \Delta \end{pmatrix} \tag{2.1}$$

where Δ is the asymmetric energy which equals the energy difference between the right and left potential wells and Δ_0 is the tunneling energy.

In the standard TLS model, a uniform distribution in Δ and a log uniform distribution in Δ_0 is usually assumed:

$$P(\Delta, \Delta_0)d\Delta d\Delta_0 = \frac{P_0}{\Delta_0}d\Delta d\Delta_0 \tag{2.2}$$

where P_0 is the two level density of states found to be on the order of $10^{44}/\text{J}\cdot\text{m}^3$. The Hamiltonian can be diagonalized to obtain the eigenstates. The wave functions of these eigenstates in the position representation, ψ_1 and ψ_2, are shown in Figure 2.6.

$$H_0 = \frac{1}{2}\epsilon\sigma_z \tag{2.3}$$

$$\epsilon = (\Delta^2 + \Delta_0^2)^{-1/2} \tag{2.4}$$

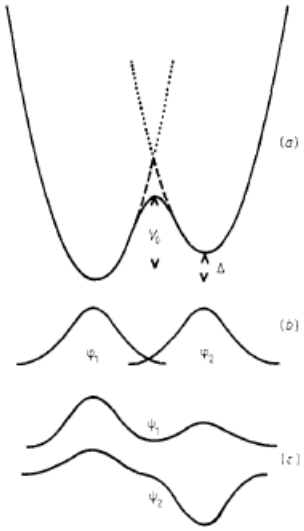

Figure 2.6: Double potential wells, localized wave functions ϕ_1 and ϕ_2, and eigenstates ψ_1 and ψ_2 of a two-level system

2.2.2 Analysis of interaction with external fields

TLS can interact with the external electric field and strain field through the perturbation of the asymmetric energy Δ.

In the **electric problem**, we can define the electric dipole moments of the two localized states ϕ_1 (lower energy state) and ϕ_2 (higher energy state) as $\mp\vec{d_0}$ where $\vec{d_0} = -\frac{1}{2}\nabla_{\vec{E}}\Delta(\vec{E})$, though the atom or group of atoms under investigation has no net charge. Here $\nabla_{\vec{E}}\Delta(\vec{E})$ represents the gradient of the asymmetric energy Δ in the parametric space spanned by the electric field $\vec{E}$. Note the consistency between the definitions of ϕ_1, ϕ_2, and $\vec{d_0}$: when $\vec{E}$ is anti-parallel with $\vec{d_0}$, the asymmetric energy Δ is increased by $\vec{d_0} \cdot \vec{E}$ (by the definition of gradient). The interaction Hamiltonian has a simple form in the localized representation:

$$H^e_{int} = -\sigma_z \vec{d_0} \cdot \vec{E} \tag{2.5}$$

The same Hamiltonian has a slightly different form in the energy representation:

$$H^e_{int} = -\left[\frac{\Delta}{\epsilon}\sigma_z + \frac{\Delta_0}{\epsilon}\sigma_x\right]\vec{d_0} \cdot \vec{E} = -(\frac{1}{2}\sigma_z\vec{d'} + \sigma_x\vec{d}) \cdot \vec{E} \tag{2.6}$$

$\vec{d'} = 2\vec{d_0}\frac{\Delta}{\epsilon}$ is called the permanent electric dipole moment. It is "permanent" because it appears in the thermodynamic equilibrium state of the TLS, which is a classical state, or in other words, a

mixed state with absolutely no coherence. $\vec{d'}$ can be also expressed as $\vec{d'} = -\nabla_{\vec{E}}\epsilon(\vec{E})$ and $\mp\frac{1}{2}d'$ can be regarded in the same fashion as the electric dipole moments of the two eigenstates ψ_1 (ground state) and ψ_2 (excited state). $\vec{d} = \vec{d_0}\frac{\Delta_0}{\epsilon}$ is called the transition electric dipole moment. The transition dipole moment only appears when the TLS is driven to be in a superposition of ψ_1 and ψ_2 (so that $\langle\sigma_x\vec{d}\rangle$ is not vanishing). The factors $\frac{\Delta}{\epsilon}$ and $\frac{\Delta_0}{\epsilon}$ in $\vec{d'}$ and $\vec{d}$ come from the change of basis from localized representation to energy representation.

In the **acoustic** problem, the interaction Hamiltonian can be similarly written as

$$H^a_{int} = -\left[\frac{\Delta}{\epsilon}\sigma_z + \frac{\Delta_0}{\epsilon}\sigma_x\right]\gamma e \tag{2.7}$$

where γ is the elastic dipole moment and e is the strain field. The interaction H^a_{int} with phonon bath can both relax the TLS back to its thermodynamic equilibrium state (the mixed state mentioned above) and cause it to lose the coherence (mathematically $\langle\sigma_x\rangle$) between ground state and excited state (real dephasing effect). We characterize the strength of the relaxation by rate T_1^{-1}. The real dephasing rate is therefore $\frac{1}{2}T_1^{-1}$ according to the master equation. Then, in the absence of any electric field, we have

$$\frac{d\langle\sigma_z(t)\rangle}{dt} = -\frac{\langle\sigma_z(t)\rangle - \sigma_z^{eq}(\epsilon)}{T_1} \tag{2.8}$$

$$\sigma_z^{eq}(\epsilon) = -\tanh(\frac{\epsilon}{2kT}) \tag{2.9}$$

$$\frac{d\langle\sigma_+(t)\rangle}{dt} = -\frac{\langle\sigma_+(t)\rangle}{2T_1} \tag{2.10}$$

$$\frac{d\langle\sigma_-(t)\rangle}{dt} = -\frac{\langle\sigma_-(t)\rangle}{2T_1} \tag{2.11}$$

where the time-dependent operators are in the Heisenberg picture, σ_z represents the difference of the probabilities in the excited state and ground state, σ_+ and σ_- represent the coherence. The solutions are simply exponential decays.

Next we analyze how the state of the TLS would physically evolve under an external **electric** field $\vec{E}(t) = \vec{E}_0(e^{i\omega t} + e^{-i\omega t})$. We consider two toy Hamiltonian $H^{rel}_{int} = -\frac{1}{2}\sigma_z d'\cdot\vec{E}$ and $H^{res}_{int} = -\sigma_x d\cdot\vec{E}$, the two components of the interaction Hamiltonian in Eq. 2.6 in the electric problem.

- H^{rel}_{int}: H^{rel}_{int} causes the eigenenergy of the TLS to oscillate with time sinusoidally with a small amplitude $\epsilon(t) = \epsilon - 2\vec{d'}\cdot\vec{E}_0\cos(\omega t)$. The TLS would be simultaneously relaxed by the interaction with the phonon bath H^a_{int} toward the instantaneous equilibrium state, which results in a delayed oscillation of the permanent dipole moment $\langle\vec{d'}\hat{\sigma}_z\rangle$ also with angular frequency ω. In the low

frequency regime $\omega \ll T_1^{-1}$, the phase delay is approximately zero since the TLS relaxes relatively fast. In the high frequency regime $\omega \gg T_1^{-1}$, in analogy to a classical damped harmonic oscillator, the phase delay should approach $\pi/2$. The amplitude of the oscillation of $\langle \vec{d}'\hat{\sigma}_z \rangle$ would, however, become increasingly small as the frequency ω goes up since there is not enough time for the TLS to relax to the instantaneous equilibrium state corresponding to $\epsilon(t)$. We call such a response the relaxation response.

- H_{int}^{res}: This is the standard Rabi problem if we do not take into account of the acoustic relaxation induced by H_{int}^{a}. The TLS is driven coherently by the external electric field to oscillate between the ground state and excited state in a harmonic manner with frequency $\Omega_R = \sqrt{\Omega^2 + \Delta_d^2}$, where $\Omega = 2\vec{E}_0 \cdot \vec{d}/\hbar$ is the Rabi frequency and $\Delta_d = \omega_L - \omega_{TLS} = \omega - \epsilon/\hbar$ is the detuning of the electric field with respect to the TLS. During the Rabi oscillation, the amplitude of the transition dipole moment of the TLS $\langle \vec{d}\hat{\sigma}_x \rangle$ also swings harmonically between zero (in either ground state or excited state) and the maximum (equal superposition between the ground state and excited state). The Rabi oscillation will be modified but still continue if H_{int}^{a} is incorporated. We call such a response the resonance response.

Let's move back to the full interaction Hamiltonian H_{int}^{e}. Since the perturbation in ϵ provided by H_{int}^{rel} is so small that the Rabi oscillation is affected very little, the state of TLS would evolve basically as there is only H_{int}^{res}. Although H_{int}^{rel} still induces the oscillation in the permanent dipole moment $\langle \vec{d}'\hat{\sigma}_z \rangle$, it is actually minuscule because the microwave signal used by KID is in the high frequency regime $f_L \sim 1$ GHz with respect to the dielectric materials with $T_1 > 1$ μs.

2.2.3 Rigorous solution of electric susceptibiities

We can solve the equations of motion of the TLS with the full interaction Hamiltonian H_{int}^{e} rigorously. Note that the Hamiltonian of TLS in an external electric field

$$H = H_0 + H_{int}^{e} \tag{2.12}$$

has a formal analogy to that of a spin 1/2 system in a magnetic field

$$H = -\hbar\gamma\vec{B} \cdot \vec{S} = -\hbar\gamma(\vec{B}_0 \cdot \vec{S}) - \hbar\gamma(\vec{B}' \cdot \vec{S}) \tag{2.13}$$

where $\vec{B}_0$ is the static magnetic field, $\vec{B}'$ is the oscillating perturbation field, and $\vec{S} = \vec{\sigma}/2$. We can identify the following correspondence:

$$-\hbar\gamma\vec{B}_0 = (0, 0, \epsilon) \tag{2.14}$$

$$-\hbar\gamma\vec{B}' = (-2\vec{d}\cdot\vec{E}, 0, -\vec{d}'\cdot\vec{E}) \tag{2.15}$$

Without any relaxation or dephasing process, the dynamic equation for a free spin in a magnetic field is

$$\frac{d}{dt}\vec{S}(t) = \gamma\vec{S}\times\vec{B} \tag{2.16}$$

where $\vec{S}(t)$ can be interpreted as the spin operator in Heisenberg picture.

In order to precisely describe the evolution of the state of TLS, the relaxation process, real dephasing process, and ensemble dephasing process must all be incorporated. The relaxation process and real dephasing process have been discussed above. We will focus on the ensemble dephasing process here. It is known that TLS can interact with each other via strain field. The interaction leads to a random fluctuation of the eigenenergy $\delta\epsilon(t)$. The coherence operator in the Heisenberg picture of a free TLS evolves as $\hat{\sigma}_+(t) = \hat{\sigma}_+(0)\exp(-j\frac{\epsilon}{\hbar}t)$. When the TLS-TLS interaction is incorporated, the independent fluctuations $\delta\epsilon(t)$ will cause destructive interferences among the TLS if we consider the ensemble average, which can be regarded as an effective dephasing process. We characterize the strength of such a process by rate $(T_2^{ens})^{-1} \sim \Delta\epsilon/\hbar$, where $\Delta\epsilon$ is the amplitude of the fluctuation. We use $T_2^{-1} = (2T_1)^{-1} + (T_2^{ens})^{-1}$ to denote the total dephasing rate.

Having all the three processes included, the evolution of the ensemble average of spin operator $\langle S_i\rangle$ can be described by the following Bloch equations:

$$\begin{aligned}
\frac{d}{dt}\langle S_x(t)\rangle &= \gamma(\langle S_y\rangle B_z - \langle S_z\rangle B_y) - \frac{\langle S_x\rangle}{T_2} = 0\\
\frac{d}{dt}\langle S_y(t)\rangle &= \gamma(\langle S_z\rangle B_x - \langle S_x\rangle B_z) - \frac{\langle S_y\rangle}{T_2} = 0\\
\frac{d}{dt}\langle S_z(t)\rangle &= \gamma(\langle S_x\rangle B_y - \langle S_y\rangle B_x) - \frac{\langle S_z\rangle - S_z^{eq}[B_z(t)]}{T_1} = 0
\end{aligned} \tag{2.17}$$

where

$$S_z^{eq}[B_z(t)] = \frac{1}{2}\tanh(\frac{\hbar\gamma B_z(t)}{2kT}) \tag{2.18}$$

is the instantaneous equilibrium value of S_z.

The electric susceptibility tensors for the relaxation response $\overline{\overline{\chi}}_{rel}(\omega)$ and resonance response $\overline{\overline{\chi}}_{res}(\omega)$ can be calculated by solving the Bloch equations[8] and substitute the B field components by their counterparts in the electric problem:

$$\langle \vec{d'} \rangle = \overline{\overline{\chi}}_{rel}(\omega) \cdot \vec{E}_0 \tag{2.19}$$

$$\langle \vec{d} \rangle = \overline{\overline{\chi}}_{res}(\omega) \cdot \vec{E}_0 \tag{2.20}$$

$$\overline{\overline{\chi}}_{rel}(\omega) = -\frac{d\sigma_z^{eq}(\epsilon)}{d\epsilon} \frac{1 - j\omega T_1}{1 + \omega^2 T_1^2} \vec{d'}\vec{d'} \tag{2.21}$$

$$\overline{\overline{\chi}}_{res}(\omega) = -\frac{\sigma_z^0}{\hbar} \left[\frac{1}{\omega_\epsilon - \omega + jT_2^{-1}} + \frac{1}{\omega_\epsilon + \omega - jT_2^{-1}} \right] \vec{d}\vec{d} \tag{2.22}$$

where $\frac{1}{2}\langle \vec{d'} \rangle$ is the induced oscillation of the permanent dipole moment and $\langle \vec{d} \rangle$ is the induced oscillation of the transition dipole moment. Both $\frac{1}{2}\langle \vec{d'} \rangle$ and $\langle \vec{d} \rangle$ have the same angular frequency ω as the driving field. $\sigma_z^{eq}(\epsilon)$ and σ_z^0 are the expectation values of $\hat{\sigma}_z$ in the steady state without and with the driving field.

$$\sigma_z^{eq}(\epsilon) = -\tanh(\frac{\epsilon}{2kT}) \tag{2.23}$$

$$\sigma_z^0 = \frac{1 + (\omega_\epsilon - \omega)^2 T_2^2}{1 + \Omega^2 T_1 T_2 + (\omega_\epsilon - \omega)^2 T_2^2} \sigma_z^{eq}(\epsilon) \tag{2.24}$$

where $\omega_\epsilon = \epsilon/\hbar$ and $\Omega = 2\vec{d} \cdot \vec{E}_0/\hbar$ is the Rabi frequency. When the drive amplitude goes to zero, the Rabi frequency vanishes and $\sigma_z^0 \to \sigma_z^{eq}$. When the drive amplitude gets large, $\sigma_z^0 \to 0$ indicating equal probability in the excited and ground states.

The susceptibility $\overline{\overline{\chi}}_{res}(\omega) \sim \vec{d}\vec{d}$ is a tensor. One of $\vec{d}$ determines the strength of the coupling with external electric field $\sim \vec{d} \cdot \vec{E}_0/\hbar(\omega_\epsilon - \omega + jT_2^{-1})$ and the other $\vec{d}$ is a measure of the transition dipole moment of the particular TLS. For the same TLS, $\vec{d}$ is fixed and its resonance response is always along this direction, and the magnitude of the response depends on the alignment between $\vec{d}$ and $\vec{E}_0$ via $\vec{d} \cdot \vec{E}_0$. Similar physical meanings hold for $\overline{\overline{\chi}}_{rel}(\omega)$ and $\vec{d'}$.

The forms of $\overline{\overline{\chi}}_{rel}(\omega)$ in the low and high frequency limits are consistent with the analysis in section 2.2.2:

$$\overline{\overline{\chi}}_{rel}(\omega \to 0) \to \left| \frac{d\sigma_z^{eq}(\epsilon)}{d\epsilon} \right| \vec{d'}\vec{d'} \tag{2.25}$$

$$\overline{\overline{\chi}}_{rel}(\omega \gg T_1^{-1}) = -j \left| \frac{d\sigma_z^{eq}(\epsilon)}{d\epsilon} \right| \frac{1}{\omega T_1} \vec{d'}\vec{d'} \to 0 \tag{2.26}$$

where in the low frequency limit, the phase delay is zero, in the high frequency limit the phase delay is $\pi/2$ and the amplitude of response is vanishing.

The first term $\sim (\omega_\epsilon - \omega + jT_2^{-1})^{-1}$ and second term $\sim (\omega_\epsilon + \omega - jT_2^{-1})^{-1}$ of $\overline{\overline{\chi}}_{res}(\omega)$ correspond to the contributions from rotating wave and counter rotating wave components in the precession of the Bloch vector $\vec{r} = (r_x, r_y, r_z)$, where $r_x = 2\mathrm{Re}(\rho_{12})$, $r_y = 2\mathrm{Im}(\rho_{12})$, $r_z = \rho_{22} - \rho_{11}$. ρ_{ij} with $i = 1, 2$ and $j = 1, 2$ are the elements of the density matrix of the TLS. Geometrically, $r_x(t)$ and $r_y(t)$ are the projection of $\vec{r}(t)$ in the $x - y$ plane whose amplitude $|\vec{r}|$ is mainly determined by its z component r_z. That is why the susceptibility $\overline{\overline{\chi}}_{res}(\omega)$ is proportional to the expectation value of $\hat{\sigma}_z$.

We are exploring the hypothesis that TLS noise in resonators comes from the fluctuation of the dielectric constant due to TLS of the KID's capacitor. We therefore want to consider the electric susceptibility due to TLS and its fluctuation.

2.3 Model of TLS noise spectral density

In Gao's thesis[8], the power and temperature dependences of MKID's resonant frequency f_0 and internal quality factor Q_i have been successfully explained with the standard TLS model we reviewed in the last section. In that work, it is also speculated that the observed TLS noise should be attributed to the contribution from each individual independently fluctuating TLS and the TLS-TLS interaction is weak enough that it does not produce noticeable correlation between different TLS's responses to the external electric field. The random state switching of each TLS comes from either the coupling with phonon bath or some other mechanisms. A specific form for the operator of the dielectric constant due to TLS $\hat{\varepsilon}_{TLS}$ was suggested. Instead of deriving the noise spectral density from $\hat{\varepsilon}_{TLS}$, Gao proposed an empirical ansatz as the solution, which well matched the experimental data in some aspects. In this thesis we will examine the validity of $\hat{\varepsilon}_{TLS}$ and explore its theoretical implications for the case that the fluctuation of individual TLS is entirely due to the coupling with phonon bath.

2.3.1 Model of the dielectric constant due to TLS

We use ε_{TLS} to represent the contribution to the overall dielectric constant from the TLS, that is

$$\varepsilon_{tot} = \varepsilon_{other} + \varepsilon_{TLS} \tag{2.27}$$

where ε_{other} include the contribution from vaccum (1) and from the non-TLS dielectrics present. In Gao's thesis the dielectric constant operator $\hat{\varepsilon}_{TLS}(\omega, \vec{r}, t)$ due to TLS is defined by extending Eq. 2.22 as:

$$\hat{\varepsilon}_{TLS}(\omega, \vec{r}, t) = -\sum_{\vec{r}_\alpha \in V_h} \vec{d}_\alpha \vec{d}_\alpha \delta(\vec{r} - \vec{r}_\alpha) \left[\frac{1}{\epsilon_\alpha - \hbar\omega + j\Gamma_\alpha} + \frac{1}{\epsilon_\alpha + \hbar\omega - j\Gamma_\alpha} \right] \hat{\sigma}_{z,\alpha}(\omega, t) \tag{2.28}$$

$\hat{\varepsilon}_{TLS}(\omega, \vec{r}, t)$ is the dielectric constant operator due to TLS for an external electric field with angular frequency ω at position $\vec{r}$ and time t. α is the label of the particular TLS. $\vec{r}_\alpha$ indicates the position of the TLS. V_h is the TLS-host volume. $\epsilon_\alpha = (\Delta_\alpha^2 + \Delta_{0,\alpha}^2)^{1/2}$ is the energy level separation. $\vec{d}_\alpha = \hat{d}_\alpha d_0 \Delta_{0,\alpha}/\epsilon_\alpha$ is the transition dipole moment where $\hat{d}_\alpha$ is the dipole orientation unit vector which is assumed to be random and isotropically distributed. Γ_α is the real dephasing rate of the TLS: $\Gamma_\alpha = \frac{1}{2} T_{1,\alpha}^{-1}$. $T_\alpha = \Gamma_\alpha^{-1}$ instead is used in the following derivation. We assume T_α is the same for all the TLS.

There is, however, an obvious problem with such a definition. Note that Eq. 2.22 only applies for an ensemble average of TLS in the steady state. Therefore, the abstraction from the steady state solution for the ensemble average of TLS as given by Eq. 2.22 to the instantaneous operator relation for a set of individual TLS shown in Eq. 2.28 is mathematically insuffucient and physically incorrect. Mathematically, when we have an equality between the expectation values for two operators $\langle \hat{A} \rangle = \langle \hat{B} \rangle$, one may not conclude that the two operators are equal. To demonstrate this point from a physics point of view, let's consider the evolution of a single TLS starting in its ground state for a time scale that is much longer than the period of the electric field but much shorter than the period of Rabi oscillation. First, we know that the dielectric constant due to the single TLS is physically well-defined and measurable. Secondly, the TLS can be simply treated as being in the ground state all the time by the assumption (no time allowed to go through the full Rabi oscillation). Eq. 2.28 gives a finite value for $\langle \hat{\varepsilon}(\omega, \vec{r}, t) \rangle$ since $\langle \hat{\sigma}_z(t) \rangle = -1$. But physically the induced transition dipole moment is vanishing since the TLS is not in any superposition of the ground state and excited state. Such an obvious discrepancy is just an example of why the definition in Eq. 2.28 is wrong and should not be used to compute $\varepsilon(\omega, \vec{r}, t)$'s time correlation (TLS noise). The right way to define the instantaneous dielectric constant operator should be through the transition dipole moment operator of TLS $\hat{\sigma}_x$ rather than $\hat{\sigma}_z$, which, however, we won't be able to further study in this thesis.

While there are physical deficiencies of the above choice of operator, we pursue a derivation of TLS noise expectations for it for two reasons: 1) these deficiencies were not recognized initially and 2) it is valuable to see what this model predicts (and how it fails) so that we may obtain some

guidance as to how a correct and complete model of TLS noise can be constructed. So we ignore the above problem and stick with the definition in Eq. 2.28, from which we can derive the power spectral density of TLS noise with some straightforward algebra.

Define the average dielectric constant operator due to TLS over the region V_h as

$$\hat{\varepsilon}^{ave}_{TLS}(\omega,t) = \frac{1}{V_h}\int_{V_h}\hat{\epsilon}_{TLS}(\omega,\vec{r},t)d\vec{r} \tag{2.29}$$

$$= -\frac{1}{V_h}\sum_{\vec{r}_\alpha\in V_h}\vec{d}_\alpha\vec{d}_\alpha\left[\frac{1}{\epsilon_\alpha-\hbar\omega+j\Gamma_\alpha}+\frac{1}{\epsilon_\alpha+\hbar\omega-j\Gamma_\alpha}\right]\hat{\sigma}_{z,\alpha}(\omega,t) \tag{2.30}$$

$$= -\frac{1}{V_h}\sum_{\vec{r}_\alpha\in V_h}\vec{d}_\alpha\vec{d}_\alpha\chi_\alpha(\omega_\epsilon,\omega)\hat{\sigma}_{z,\alpha}(\omega,t) \tag{2.31}$$

$$\chi_\alpha(\omega_\epsilon,\omega) = \frac{1}{\hbar(\omega_\epsilon-\omega+jT_\alpha^{-1})}+\frac{1}{\hbar(\omega_\epsilon+\omega-jT_\alpha^{-1})} \tag{2.32}$$

The power spectral density of $\hat{\varepsilon}^{ave}_{TLS}(\omega,t)$ is defined as

$$S_{\varepsilon^{ave}_{TLS}}(\nu) = \lim_{T\to\infty}\frac{1}{2T}\int_{-T}^{T}dt\int_{-\infty}^{\infty}d\tau e^{-i\nu\tau}\left\langle\hat{\varepsilon}^{ave\dagger}_{TLS}(\omega,t+\tau)\hat{\varepsilon}^{ave}_{TLS}(\omega,t)\right\rangle_{ss} \tag{2.33}$$

where the symbol $\langle\rangle_{ss}$ means expectation value in the steady state.

The time correlation $\hat{\varepsilon}^{ave\dagger}_{TLS}(\omega,t+\tau)\hat{\varepsilon}^{ave}_{TLS}(\omega,t)$ can be simplified by averaging $\hat{d}_\alpha$ isotropically and replacing the sum of TLS with an integration over the density of states. Since only the component of the induced transition dipole moment along the external electric field matters, we treat $\hat{\varepsilon}^{ave}_{TLS}(\omega,t)$ and its time correlation as a scalar in the following discussion:

$$\hat{\varepsilon}^{ave\dagger}_{TLS}(\omega,t+\tau)\hat{\varepsilon}^{ave}_{TLS}(\omega,t) \tag{2.34}$$

$$= \frac{1}{V_h^2}\sum_{\vec{r}_\alpha\in V_h}\vec{d}_\alpha\vec{d}_\alpha\vec{d}_\alpha\vec{d}_\alpha|\chi_\alpha(\omega_\epsilon,\omega)|^2\hat{\sigma}_{z,\alpha}(\omega,t+\tau)\hat{\sigma}_{z,\alpha}(\omega,t) \tag{2.35}$$

$$\to \frac{1}{V_h}\int\int\int(\vec{e}\cdot\vec{d}_\alpha)(\vec{e}\cdot\vec{d}_\alpha)(\vec{d}_\alpha\cdot\vec{e})(\vec{d}_\alpha\cdot\vec{e})|\chi_\alpha(\omega_\epsilon,\omega)|^2\hat{\sigma}_{z,\alpha}(\omega,t+\tau)\hat{\sigma}_{z,\alpha}(\omega,t)d\hat{d}_\alpha\frac{P}{\Delta_0}d\Delta_0 d\Delta \tag{2.36}$$

$$= \frac{1}{V_h}\int_0^{\Delta_{max}}d\Delta\int_{\Delta_{0,min}}^{\Delta_{0,max}}\frac{P}{\Delta_0}d\Delta_0\int_0^{\frac{\pi}{2}}\sin\theta d\theta\cos^4\theta\left(\frac{\Delta_0}{\epsilon}\right)^4 d_0^4|\chi_\alpha(\omega_\epsilon,\omega)|^2\hat{\sigma}_{z,\alpha}(\omega,t+\tau)\hat{\sigma}_{z,\alpha}(\omega,t) \tag{2.37}$$

where $\hat{e}$ is a unit vector indicating the direction of the external electric field, Δ_{max} is the cutoff of the asymmetric energy Δ, $\Delta_{0,max}$, and $\Delta_{0,min}$ are the upper and lower limits of the tunneling energy Δ_0, θ is the angle between the direction of the electric field and the transition dipole moment.

Let $u = \Delta_0/\epsilon$ and apply the following changes of variables.

$$\int_0^{\Delta_{max}} \int_{\Delta_{0,min}}^{\Delta_{0,max}} \frac{P}{\Delta_0} d\Delta_0 d\Delta = \int_0^{\epsilon_{max}} \int_{u_{min}}^{1} \frac{P_0}{u\sqrt{1-u^2}} du d\epsilon \tag{2.38}$$

The time correlation can be reduced to

$$\hat{\varepsilon}_{TLS}^{ave\dagger}(\omega, t+\tau)\hat{\varepsilon}_{TLS}^{ave}(\omega, t) \tag{2.39}$$

$$= \frac{1}{V_h} \int_0^{\epsilon_{max}} d\epsilon \int_{u_{min}}^{1} \frac{P_0}{u\sqrt{1-u^2}} u^4 du \int_0^{\frac{\pi}{2}} \cos^4\theta \sin\theta d\theta d_0^4 |\chi_\alpha(\omega_\epsilon, \omega)|^2 \hat{\sigma}_{z,\alpha}(\omega, t+\tau)\hat{\sigma}_{z,\alpha}(\omega, t) \tag{2.40}$$

$$= \frac{2}{15}\frac{P_0 d_0^4}{V_h} \int_0^{\epsilon^{max}} d\epsilon |\chi(\omega_\epsilon, \omega)|^2 \hat{\sigma}_z(\omega, t+\tau)\hat{\sigma}_z(\omega, t) \tag{2.41}$$

The subscript α in Eq. 2.40 indicates the dependence on ϵ, u, and θ of the evolution of the TLS. Note that the major contribution to the integration over u and θ comes from the region $u \sim 1$ and $\theta \sim 0$, which corresponds to the case that $|\vec{d}| \sim |\vec{d_0}|$ and $\vec{d} \parallel \vec{E}_0$. Since the dependence of the evolution of the TLS on u and θ is through the Rabi frequency $\Omega = 2\vec{d} \cdot \vec{E}_0/\hbar = 2|\vec{d_0}||\vec{E}_0|u\cos\theta$, we can safely assume all the TLS have the same Rabi frequency $\Omega = 2|\vec{d_0}||\vec{E}_0|$ to simplify the calculation. This is a good approximation for our problem. The subscript α is hence dropped from Eq. 2.41.

The power spectral density of $\hat{\varepsilon}_{TLS}^{ave}(\omega, t)$ is therefore

$$S_{\varepsilon_{TLS}^{ave}}(\nu) = \frac{2}{15}\frac{P_0 d_0^4}{V_h} \int_0^{\epsilon^{max}} d\epsilon |\chi(\omega_\epsilon, \omega)|^2 S_{\sigma_z}(\nu) \tag{2.42}$$

The dielectric constant can be decomposed into the real part and imaginary part:

$$\hat{\varepsilon}_{TLS}^{ave} = \hat{\varepsilon}'_{TLS} - j\hat{\varepsilon}''_{TLS} \tag{2.43}$$

Their power spectral densities are

$$S_{\varepsilon'_{TLS}}(\nu) = \frac{2}{15}\frac{P_0 d_0^4}{V_h} \int_0^{\epsilon^{max}} d\epsilon |\mathrm{Re}\chi(\omega_\epsilon, \omega)|^2 S_{\sigma_z}(\nu) \tag{2.44}$$

$$S_{\varepsilon''_{TLS}}(\nu) = \frac{2}{15}\frac{P_0 d_0^4}{V_h} \int_0^{\epsilon^{max}} d\epsilon |\mathrm{Im}\chi(\omega_\epsilon, \omega)|^2 S_{\sigma_z}(\nu) \tag{2.45}$$

2.3.2 Power spectral density of $\hat{\sigma}_z$ for a single TLS

To calculate the power spectral density $S_{\sigma_z}(\nu)$, we need to know the evolution of the density operator of the TLS, as it contains the information of the state populations and their time correlation. The

evolution of the density operator of the TLS can be described by the Heisenberg equation

$$\dot{\hat{\rho}} = \frac{1}{i}[\hat{H}, \hat{\rho}] + \hat{L}\hat{\rho} \tag{2.46}$$

$\hat{H}$ is the Hamiltonian of a TLS driven by an external electric field. $\hat{H}$ can be written in the interaction picture as

$$\hat{H} = -\Delta_d \hat{\sigma}_z + \frac{\Omega}{2}(\hat{\sigma}_+ + \hat{\sigma}_-) \tag{2.47}$$

where $\Delta_d = \omega_L - \omega_{TLS} = \omega - \omega_\epsilon$ is the detuning and $\Omega = 2\vec{d} \cdot \vec{E}_0/\hbar$ is the Rabi frequency.
$\hat{L}$ is the Lindblad operator that describes the effect on the TLS of its coupling with the phonon bath[23, 24, 25]. $\hat{L} = \hat{L}(\hat{c}_{em}) + \hat{L}(\hat{c}_{abs}) + \hat{L}(\hat{c}_d)$ can be decomposed into three components:

$$\hat{L}(\hat{c}_{em})\hat{\rho} = \hat{c}_{em}\hat{\rho}\hat{c}_{em}^\dagger - \frac{1}{2}(\hat{c}_{em}^\dagger \hat{c}_{em}\hat{\rho} + \hat{\rho}\hat{c}_{em}^\dagger \hat{c}_{em}) \tag{2.48}$$

$$\hat{L}(\hat{c}_{abs})\hat{\rho} = \hat{c}_{abs}\hat{\rho}\hat{c}_{abs}^\dagger - \frac{1}{2}(\hat{c}_{abs}^\dagger \hat{c}_{abs}\hat{\rho} + \hat{\rho}\hat{c}_{abs}^\dagger \hat{c}_{abs}) \tag{2.49}$$

$$\hat{L}(\hat{c}_d)\hat{\rho} = \hat{c}_d\hat{\rho}\hat{c}_d^\dagger - \frac{1}{2}(\hat{c}_d^\dagger \hat{c}_d\hat{\rho} + \hat{\rho}\hat{c}_d^\dagger \hat{c}_d) \tag{2.50}$$

where $\hat{c}_{em}$, $\hat{c}_{abs}$, and $\hat{c}_d$ correspond, respectively, to the phonon emission induced projection, phonon absorption induced projection, and ensemble dephasing induced projection. We have

$$\hat{c}_{em} = [(1+n)\Gamma]^{\frac{1}{2}}\hat{\sigma}_- \tag{2.51}$$

$$\hat{c}_{abs} = (n\Gamma)^{\frac{1}{2}}\hat{\sigma}_+ \tag{2.52}$$

$$\hat{c}_d = (2\Gamma_d)^{\frac{1}{2}}\hat{\sigma}_z \tag{2.53}$$

where ω_L is the angular frequency of the electric field or the probe signal (the subscript L indicates "laser" for general purpose), $n = (e^{\hbar\omega_L/k_BT} - 1)^{-1}$ is the number of phonon quanta at angular frequency ω_L in the thermal bath at temperature T, $\Gamma = \frac{1}{2n+1}T_1^{-1}$ is the spontaneous decay rate of the TLS due to its coupling with the phonon bath, and $\Gamma_d = (T_2^{ens})^{-1} = T_2^{-1} - \frac{1}{2}T_1^{-1}$ is the ensemble dephasing rate due to TLS-TLS interaction. As we discussed before, such a dephasing process is only meaningful for the ensemble average of many TLS. Here we consider the evolution of a single TLS, so Γ_d should not be included. The following discussion keeps the ensemble dephasing term as an extra degree of freedom in order to best fit the experimental data.

The terms in Lindblad operator have very clear physical interpretations. Take $\hat{L}(\hat{c}_{em})$ as the

example. $\hat{c}_{em}\hat{\rho}\hat{c}_{em}^{\dagger}$ represents the increase rate of the ground state probability due to phonon emission induced decay from the excited state. $-\frac{1}{2}(\hat{c}_{em}^{\dagger}\hat{c}_{em}\hat{\rho}+\hat{\rho}\hat{c}_{em}^{\dagger}\hat{c}_{em})$ represents the decrease rate of the excited state and superposition probability in the same process.

Having the equations of motion for the evolution of the density operator of the TLS, we can compute $S_{\sigma_z}(\nu)$ very efficiently with the aid of quantum optics toolbox[26].

2.4 Theoretical results about TLS noise

In this section we examine the theoretical dependences of the normalized TLS frequency noise spectral density $S_{\varepsilon'}^{n}=S_{\varepsilon'_{TLS}}(\nu)\left(\frac{2}{15}\frac{P_0 d_0^4}{V_h}\right)^{-1}$ on noise frequency ν[27], amplitude of the electric field $|\vec{E}|$[28], and temperature T[29]. We adjust the two independent free parameters Γ and Γ_d in the above model to match the experimental data.

2.4.1 Power law dependence on noise frequency

Figure 2.7 shows the theoretical normalized TLS frequency noise spectral density for $f_L = 1$ GHz, $\Gamma = 100$ Hz, $\Gamma_d = 100$ Hz, $\Omega = 0$ Hz (zero electric field) as a function of noise frequency ν at several temperatures from $T = 1\hbar\omega_L/k_B$ (50mK) to $T = 10\hbar\omega_L/k_B$ (500mK). For the curve corresponding to the lowest temperature, we observe power law dependence $S_{\varepsilon'}^{n}(\nu) \sim \nu^{-1/2}$ for $\nu = 10 \sim 1000$Hz, which is qualitatively consistent with the experimental data as shown in Figure 2.3.

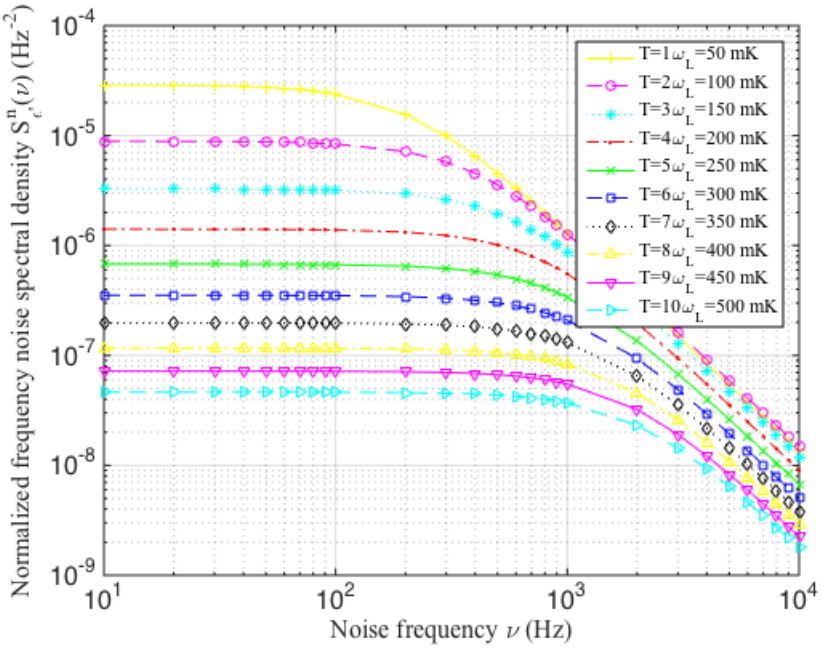

Figure 2.7: Theoretical frequency noise spectral density for $f_L = 1$ GHz, $\Gamma = 100$ Hz, $\Gamma_d = 100$ Hz, $\Omega = 0$ Hz at several temperatures.

2.4.2 Power law dependence on amplitude of the electric field

Figure 2.8 shows the theoretical normalized TLS frequency noise spectral density for $f_L = 1$ GHz, $\Gamma = 100$ Hz, $\Gamma_d = 100$ Hz, $T = 1\hbar\omega_L/k_B$ at noise frequency $\nu = 50$ Hz as a function of Rabi frequency $\Omega \sim |\vec{E}|$. We observe power law dependence $S^n_{\varepsilon'}(\nu) \sim \Omega^{-1}$ for $\Omega = \Gamma \sim 10\Gamma = 100 \sim 1000$ Hz, which is qualitatively consistent with the experimental data as shown in Figure 2.4.

The underlying physics of the monotonic dependence of TLS frequency noise on amplitude of the electric field is illustrated by Figure 2.9: the electric field shifts the peak of the spectrum of σ_z by roughly the Rabi frequency Ω. Therefore the frequency range of interest for astronomical observation (below 1000 Hz) moves further toward the tails of the spectrum, resulting in the $\sim \Omega^{-1}$ dependence.

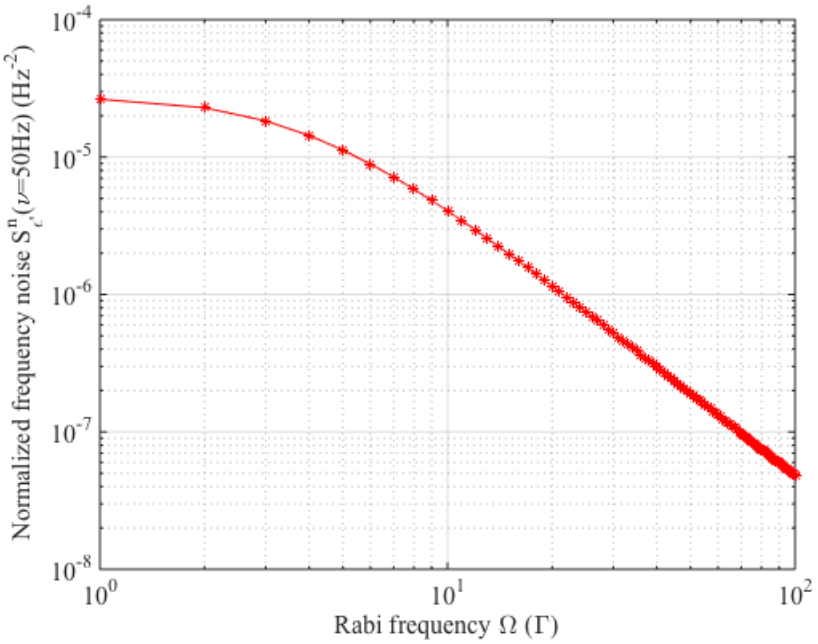

Figure 2.8: Theoretical frequency noise versus Rabi frequency for $f_L = 1$ GHz, $\Gamma = 100$ Hz, $\Gamma_d = 100$ Hz, $T = 1\omega_L$=50 mK, $\nu = 50$ Hz.

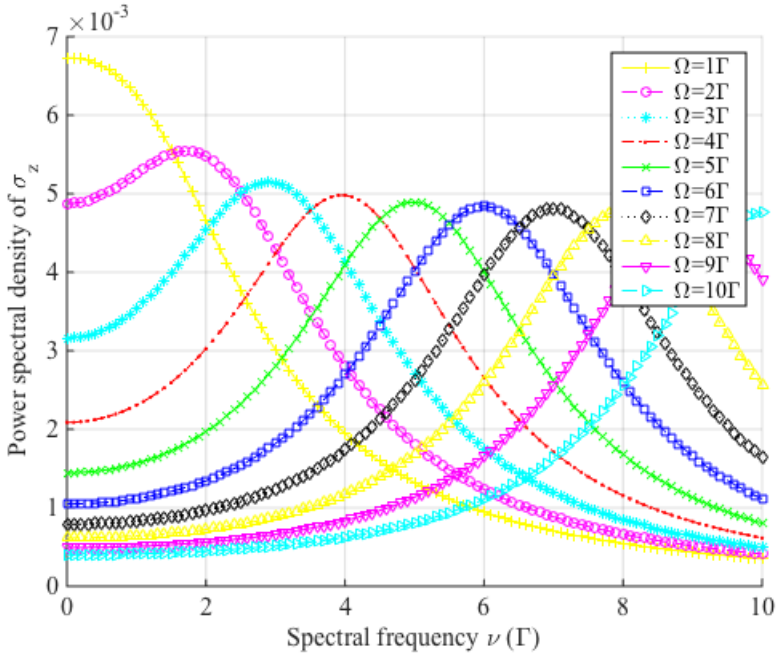

Figure 2.9: Theoretical spectral density of σ_z for $f_L = 1$ GHz, $\Gamma = 100$ Hz, $\Gamma_d = 100$ Hz, $T = 1\omega_L$=50 mK at several Rabi frequencies.

2.4.3 Power law dependence on temperature

Figure 2.10 shows the theoretical normalized TLS frequency noise spectral density for $f_L = 1$ GHz, $\Gamma = 100$ Hz, $\Gamma_d = 100$ Hz, $\Omega = 0$ Hz (zero electric field) at noise frequency $\nu = 50$ Hz as a function of temperature. We observe power law dependence $S^n_{\varepsilon'}(\nu) \sim T^{-2.5}$ from $T = 1\hbar\omega_L/k_B$ to $10\hbar\omega_L/k_B$, which is qualitatively consistent with the experimental data as show in Figure 2.5.

The underlying physics of the non-monotonic dependence on temperature is illustrated by Figure 2.11. From the definition of power spectral density, we know that $\int_{-\infty}^{\infty} S_{\sigma_z}(\nu)d\nu = 2\pi\langle\hat{\sigma}_z^2\rangle_{ss}$. In the low temperature regime $T \leq \hbar\omega_L/k_B$ when the TLS stays close to the ground state most of the time, the variance $\langle\hat{\sigma}_z^2\rangle_{ss}$ increases as temperature goes higher and so does $S_{\sigma_z}(\nu)$. In the high temperature regime $T \geq \hbar\omega_L/k_B$ when the TLS stays in the ground state and excited state with equal probability, the variance $\langle\hat{\sigma}_z^2\rangle_{ss} \approx 1$, but the bandwidth of the spectrum grows proportionally to the temperature. So $S_{\sigma_z}(\nu)$ for a fixed ν would decrease as temperature goes higher.

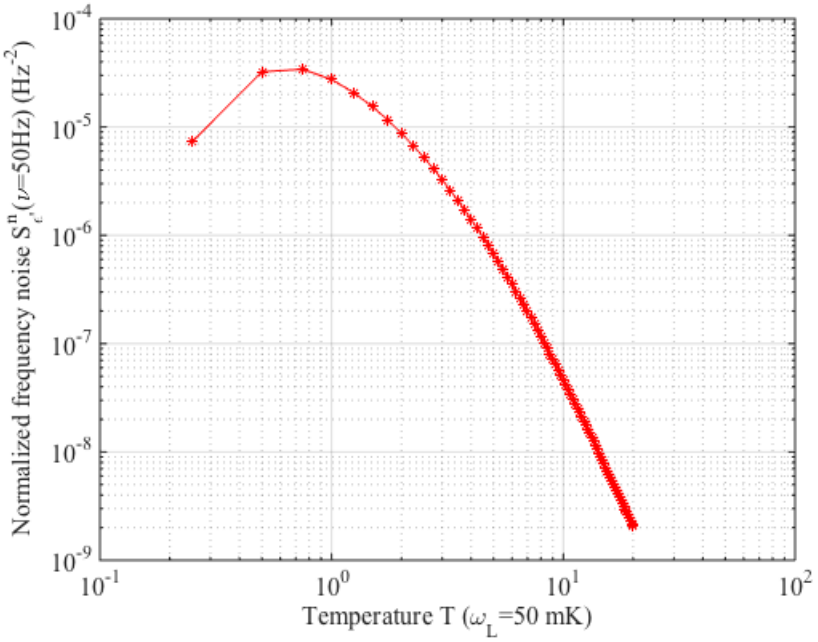

Figure 2.10: Theoretical frequency noise versus temperature for $f_L = 1$ GHz, $\Gamma = 100$ Hz, $\Gamma_d = 100$ Hz, $\Omega = 0$ Hz, $\nu = 50$ Hz.

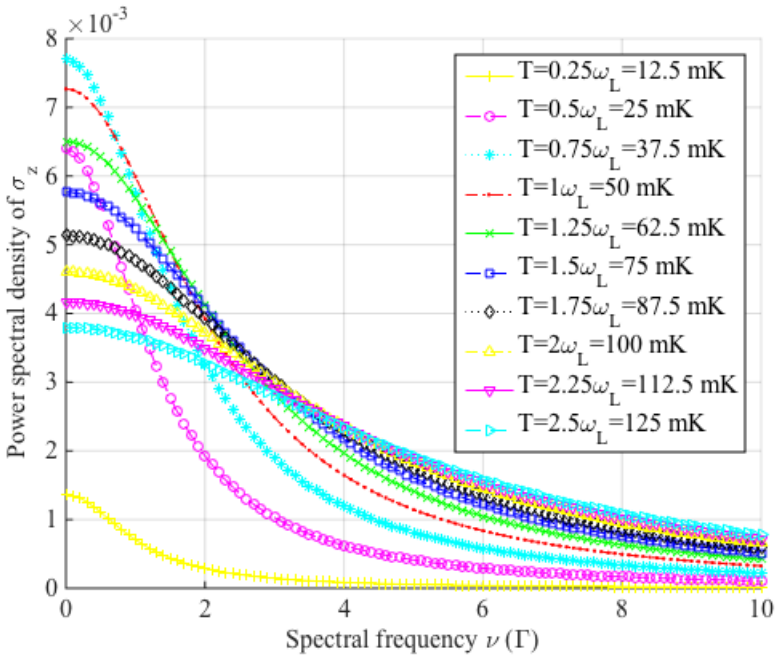

Figure 2.11: Theoretical spectral density of σ_z for $f_L = 1$ GHz, $\Gamma = 100$ Hz, $\Gamma_d = 100$ Hz, $\Omega = 0$ Hz, $\nu = 50$ Hz at several temperatures.

2.4.4 Discussion

We have successfully chosen the values for Γ_1 and Γ_d to match the theoretical predictions of TLS frequency noise with experimental data. However these "optimal" values ∼100 Hz are orders of magnitude off from the actual values ∼10 to 100 kHz for Γ estimated with Fermi's golden rule[30] and 10 MHz for Γ_d, implying that the demonstrated consistency might just be pure coincidence.

We can also derive the relative magnitude between the TLS frequency noise and amplitude noise by comparing the integrals in Eq. 2.44 and Eq. 2.45.

$$S_{\varepsilon'_{TLS}}(\nu) \sim \int_0^{\epsilon^{max}} d\epsilon |\mathrm{Re}\chi(\omega_\epsilon, \omega)|^2 S_{\sigma_z}(\nu) \sim T_\alpha \sim \int_0^{\epsilon^{max}} d\epsilon |\mathrm{Im}\chi(\omega_\epsilon, \omega)|^2 S_{\sigma_z}(\nu) \sim S_{\varepsilon''_{TLS}}(\nu) \quad (2.54)$$

Therefore, the model predicts that the frequency noise is comparable with amplitude noise. However, the experimental data shows that they are generally off by several orders of magnitude as illustrated by Figure 2.3, revealing another discrepancy.

Such inefficacy of the model can be attributed to the bad "abstraction" discussed in section 2.3.1. To understand the intrinsic noise of a single TLS free of interaction with other TLS, we might have to numerically simulate a long time series of the TLS's response to the external electric field. Recent studies suggest that to fully explain TLS noise the TLS-TLS interaction must also

be incorporated[11, 12]. Further work is still needed to justify this theory, such as whether it can reasonably relate material property to the absolute strength of the TLS noise.

Chapter 3

Architecture of the millimeter wave coupler and KID design of LWCam

In this chapter we describe 1) the architecture of the millimeter wave coupling from the microstrip transmission line exiting the antenna to the KID inductor and 2) the design of the KID resonator (inductor and capacitor) and its coupling with the microwave readout line.

3.1 Architecture of the millimeter wave coupler

In Chapter 1 we briefly explained the way that the millimeter light is received by the phased array slot antenna. A signal is created upon the absorption of a photon in the microstrip transmission line that exits the antenna. The primary prior implementation of coupling of millimeter wave from microstrip transmission line to a KID was in MUSIC[14]. MUSIC uses single-scale, single-polarization phased-array antennas, covering four spectral bands (150, 220, 290, and 350 GHz). It uses KIDs that combine a coplanar waveguide (CPW) inductor with an interdigitated capacitor (IDC). The majority of the KID is niobium, but there is a 350 μm length of aluminum at the shorted end of the CPW. To couple from microstrip transmission line to the Al KID, the Nb microstrip runs over this Al section. Since Al with $T_c \sim 1$ K is absorptive for photons with $h\nu > 2\Delta$, the millimeter wave power can be dissipated in Al to break Cooper pairs, modifying its kinetic inductance as described in earlier sections.

For LWCam, we seek to use TiN KIDs because of their higher responsivity and thus greater prospects for fundamental-noise-limited sensitivity. However, the above mentioned coupling scheme does not work for the highly resistive material TiN as opposed to Al. Normally the impedance of Nb microstrip transmission line with dimensions of a few microns is on the order of 50 Ω. Switching to TiN ground plane dramatically increases this value by a factor of ten[31] as given in Table 3.1.

The resultant impedance mismatch would cause reflection of a major fraction of the millimeter wave power from the antenna. The topic of this section is therefore about how to efficiently couple the power from the Nb microstrip transmission line to the TiN inductor/absorber[34].

We will first illustrate the general structure of the coupling circuit, including the constituent materials and geometries. The coupling process is subsequently modeled both analytically and with finite element simulation. Also in order to maximize the KID responsivity, the millimeter wave power must be guaranteed to deposit uniformly over the entire absorber. Special features involving a power splitter and half-wavelength phase shifter are proposed to address this issue. At last we present a study about the coupling efficiency over wide (several tens of GHz) bands to validate the overall performance of the design. Throughout this section, the "coupling capacitor" refers to the millimeter wave coupling capacitor unless specifically emphasized by "readout coupling capacitor".

3.1.1 Structure of the coupler

We will first describe the structure following the cross-sectional view as given by Figure 3.1. The device/coupler is composed of three dielectric layers and three patterned metal layers. Several functional components are formed within this structure: KID inductor/absorber, KID (parallel-plate) capacitor, microstrip transmission line from the antenna, and (parallel-plate) coupling capacitor (its role will be elaborated on in the latter part of this section). The thicknesses and materials of these layers (from top to bottom) are listed together with descriptions of their roles in the corresponding functional components.

- 150nm Nb: microstrip from the antenna, top plates of coupling capacitor
- 270nm amorphous Si[1]: dielectric material between the plates of coupling capacitor, dielectric material between the microstrip from the antenna and its ground plane
- 150nm Nb/20nm TiN: top plate of KID capacitor/KID inductor, bottom plates of coupling capacitor
- 800nm amorphous Si: dielectric material between the top plates and floating virtual ground of KID capacitor, dielectric material between microstrip from the antenna and its ground plane
- 200nm Nb: ground plane of the microstrip transmission from the antenna, ground plane of TiN microstrip transmission line, floating virtual ground of KID capacitor

[1]We use hydrogenated amorphous silicon α:Si-H since hydrogen can significantly reduce the dangling bonds and thus two level systems in the amorphous silicon, improving KID's sensitivity.

- crystalline Si: substrate

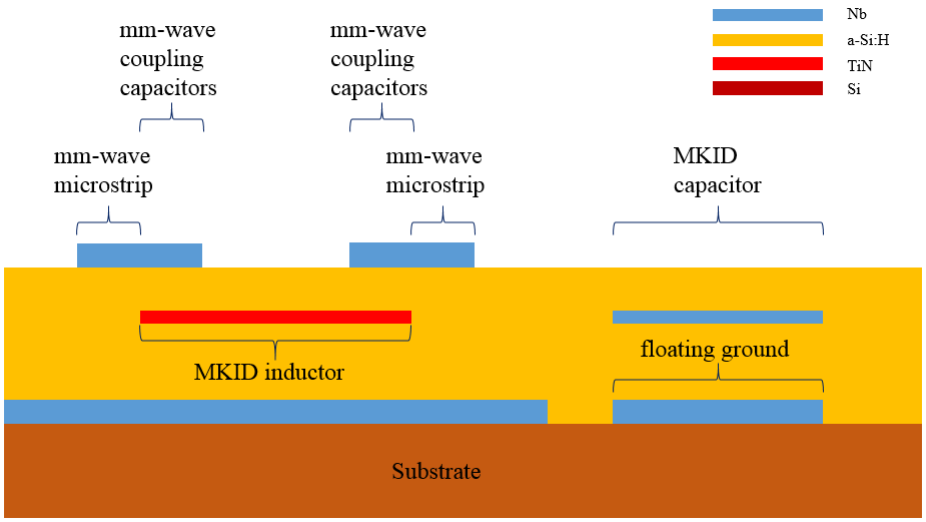

Figure 3.1: Cross-sectional view of the KID device.

Next we will describe the structure layer by layer following the plan view. In the top metal layer the 4 μm wide microstrip that carries the millimeter wave signal generated from the antenna splits into two branches with equal width. The upper (in the plan view) branch is attached to a row of 3 μm $\times$ 6 μm **rectangles** separated by 1 μm wide gap. Those are the top plates of the coupling capacitors. The lower branch (in the plan view), instead of being directly connected to the **rectangles**, first goes through a meandered region with length of half of a wavelength, which works as a phase shifter. Figure 3.2 is the plan view of the left end in the top metal layer. Both of the two branches are left unterminated at the right ends, as shown in Figure 3.3.

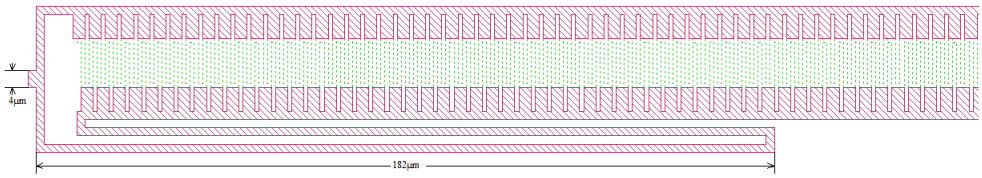

Figure 3.2: Plan view of the KID device's left end in the top metal (Nb) layer. Solid red is Nb in the top layer and dashed green is the projection of TiN from the middle layer.

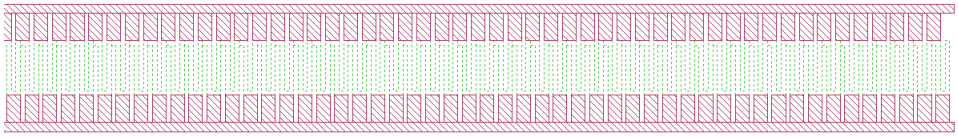

Figure 3.3: Plan view of the KID device's right end in the top metal (Nb) layer. Solid red is Nb in the top layer and dashed green is the projection of TiN from the middle layer.

In the middle metal layer, the 1 μm wide meandered TiN microstrip forms the KID inductor/absorber and a lossy transmission line with the Nb ground for the millimeter wave. A row of **polygons** with varying sizes are attached to the microstrip, which are the bottom plates of the coupling capacitors. The plan views of the middle TiN layer are shown in Figure 3.4 and 3.5.

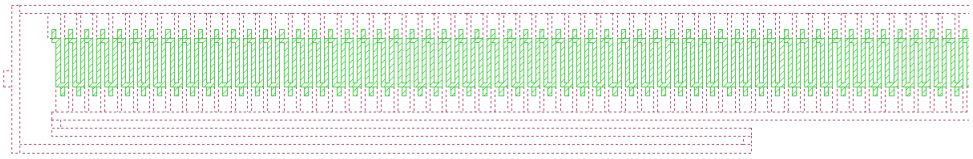

Figure 3.4: Plan view of the KID device's left end in the middle metal (TiN) layer. Dashed red is the projection of Nb from the top layer and solid green is TiN in the middle layer.

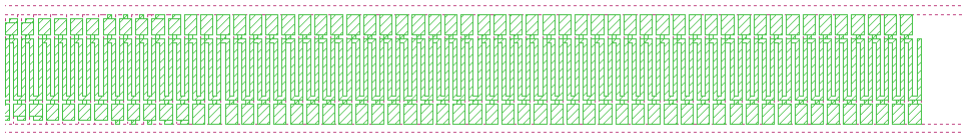

Figure 3.5: Plan view of the KID device's right end in the middle metal (TiN) layer. Dashed red is the projection of Nb from the top layer and solid green is TiN in the middle layer.

3.1.2 Model of the coupling process

The basic idea of the coupling scheme is to establish a quasi-continuous capacitive coupling C_c between the Nb microstrip transmission line from the antenna and the TiN microstrip transmission line. We make C_c by creating a series of parallel-plate coupling capacitors, with the top plates (3 μm$\times$6 μm rectangles as mentioned above) attached to Nb microstrip in the top metal layer and bottom plates (polygons as mentioned above) attached to TiN microstrip in the middle metal layer. A distributed element model is shown in Figure 3.6.

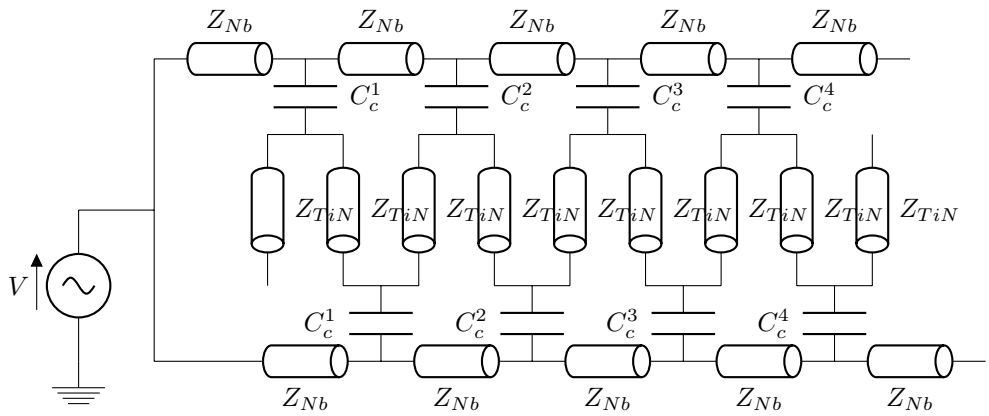

Figure 3.6: Distributed element model of the coupling scheme. Z_{Nb} denotes the impedance of Nb transmission line and Z_{TiN} denotes the impedance of TiN transmission line.

We will analyze the coupling mechanism qualitatively next based on the lumped element model as shown in Figure 3.7 and sort out which physical factor dominates the coupling process and determines the efficiency. The several relevant parameters are listed below.

- A_t=18 μm^2: area of coupling capacitor's top plate; the subscript t means "in the top metal layer"
- A_m: area of coupling capacitor's bottom plate; the subscript m means "in the middle metal layer"
- t_t: thickness of the top dielectric layer
- t_m: thickness of the middle dielectric layer
- C_{Nb}^g: capacitance between Nb microstrip and ground plane induced by the rectangle
- C_{TiN}^g: capacitance between TiN microstrip and ground plane induced by the polygon

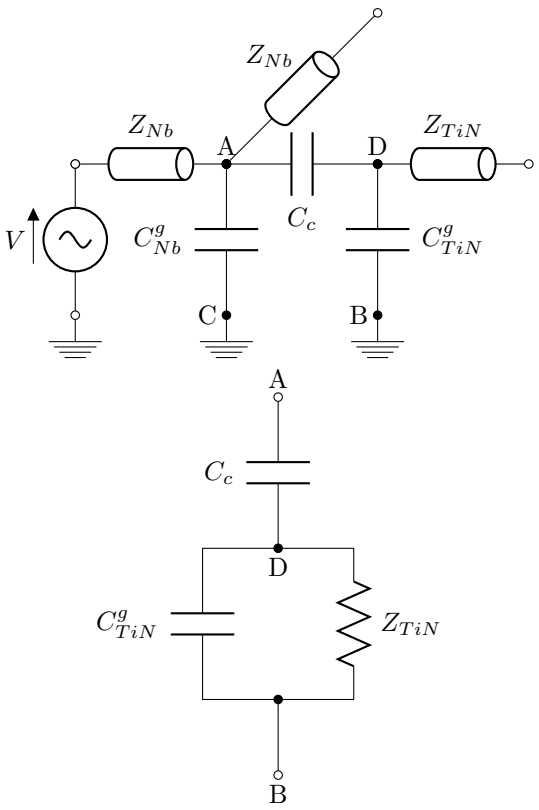

Figure 3.7: Lumped element model of the coupling scheme. Z_{Nb} denotes the impedance of Nb transmission line and Z_{TiN} denotes the impedance of TiN transmission line.

The capacitances can be expressed in terms of the geometric parameters:

$$C_c = \epsilon_{Si}\frac{A_m}{t_t} = \frac{\epsilon_{Si}A_t}{t_t}\frac{A_m}{A_t} \tag{3.1}$$

$$C^g_{Nb} = \epsilon_{Si}\frac{A_t}{t_t + t_m} = \frac{\epsilon_{Si}A_t}{t_t}\frac{1}{1 + t_m/t_t} \tag{3.2}$$

$$C^g_{TiN} = \epsilon_{Si}\frac{A_m}{t_m} = \frac{\epsilon_{Si}A_t}{t_t}\frac{A_m}{A_t}\frac{1}{t_m/t_t} \tag{3.3}$$

Table 3.1 shows the impedances of relevant components in Figure 3.7.

Component	Z_{Nb}	C^g_{Nb}	C_c	C^g_{TiN}	Z_{TiN}
Impedance (Ω)	50	0.1×10^4	0.4×10^4	1.3×10^4	800

Table 3.1: Impedances of relevant components evaluated at ν=90 GHz, $t_t = 270$ nm, $t_m = 800$ nm and A_m=1 μm^2.

Let's consider the millimeter-wave signal generated at the antenna traveling along Nb transmission line with amplitude V_0. At the junction (point A) where Nb microstrip is capacitively coupled to TiN microstrip via C_c, a fraction of the power is transferred into TiN transmission line. Since

the impedance between A and B, mainly contributed by $Z(C_c)$, is much larger than Z_{Nb}, such a fraction is very small, ensuring that no impedance mismatch is created and the millimeter wave can continue to propagate down the Nb microstrip transmission line.

Given that the coupling is weak, we know $V_{AC} \approx V_0$. The power dissipation in the TiN transmission line is therefore

$$P = I^2 Z_{TiN} = (V_0/Z(C_c))^2 Z_{TiN} \propto t_t^{-2} t_m \tag{3.4}$$

We neglect the $Z(C^g_{TiN})$ term since $Z(C^g_{TiN}) \gg Z_{TiN}$. So the ratio of dielectric thicknesses t_t/t_m also affects the coupling strength. We simulated the attenuation length of current in Nb transmission line for $t_t/t_m = 3$ and $t_t/t_m = 1/3$ with several sizes of coupling capacitor. $t_t + t_m = 1080$ nm is fixed. The results are shown in Figure 3.8. For size of 1 μm^2, the ratio between power attenuation lengths is (22 mm/6.3 mm)$^2 \sim 12$, qualitatively consistent with the above analysis as in Eq. 3.4: $((3^{-2} \times 1)/(1^{-2} \times 3))^{-1} = 27$. The actual design takes t_t/t_m=270 nm/800 nm=1/3, as it provides the right coupling strength.

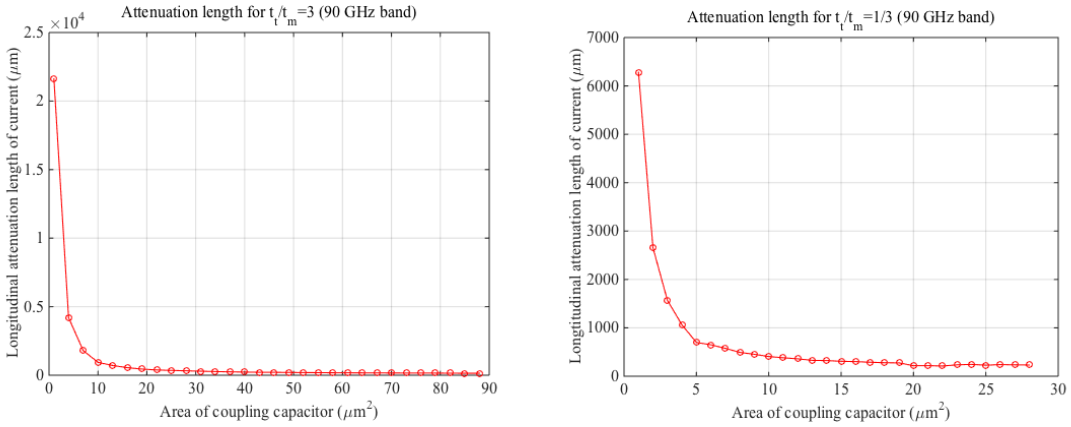

Figure 3.8: Attenuation length of current in Nb transmission line for $t_t/t_m = 3$ (left) and $t_t/t_m = 1/3$ (right).

3.1.3 Uniform power deposition

KID's responsivity (fractional shift in resonant frequency per unit optical power) is maximized only with the quasi-particles generated uniformly within the entire inductor, because in the recombination-limited regime uniform distribution of quasiparticles yields the longest effective lifetime for a given input optical power, inductor volume, and choice of material. We must therefore make sure that the power dissipation in the TiN meandered microstrip is uniform both vertically and horizontally

(from the plan view).

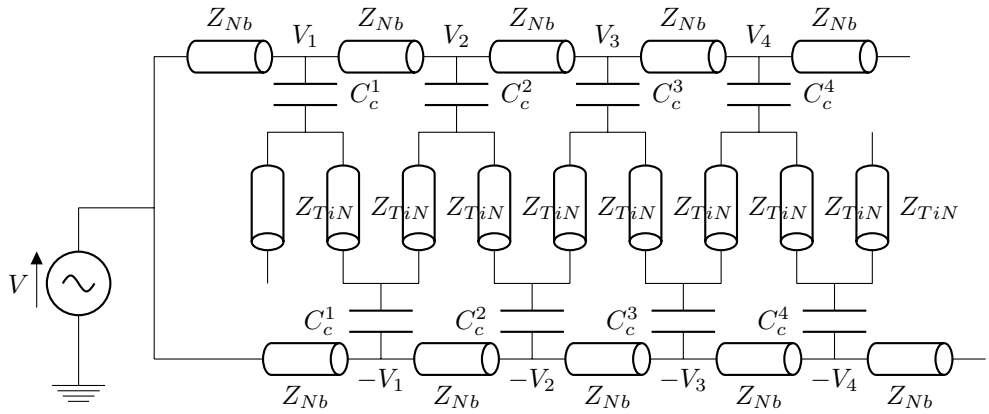

Figure 3.9: Symmetric sources of the TiN transmission line.

In the vertical direction the 50/50 power splitter and half-wavelength shifter introduced earlier in this chapter are necessary to reach this goal. As illustrated in Figure 3.4 and Figure 3.9, the two ends of each vertical section of TiN meandered microstrip are capacitively coupled to the upper and lower Nb microstrips, respectively. The splitter and shifter make the voltages at the two Nb microstrips equal in magnitude but opposite in sign. Therefore the power dissipation in TiN is guaranteed to be symmetric around the central line. Moreover, in order for the power to be absorbed uniformly in the vertical direction, the length of each vertical TiN section must also be shorter than or comparable to the power attenuation length. According to transmission line theory, we have that the propagation constant and field attenuation length are

$$\gamma = \alpha + j\beta = \sqrt{(R + j\omega L)(G + j\omega C)} \approx \sqrt{jR\omega C} \tag{3.5}$$

$$\lambda_{att} = 1/\alpha \tag{3.6}$$

where R, L, G, and C are the resistance, inductance, conductance, and capacitance per unit length of the transmission line, and λ_{att} is the attenuation length. We refer to this attenuation length as transverse attenuation length in the following discussion. The transverse attenuation lengths of a 1 μm-wide 20 nm-thick TiN microstrip on top of 800 nm amorphous Si are listed for six millimeter wave bands in Table 3.2.

In the horizontal direction the coupling capacitance C_c is adiabatically adjusted along the Nb transmission line by changing the areas of the bottom plates (a series of polygons as shown in Figure 3.13). The coupling strength can be characterized by its equivalent attenuation length of power in

Parameter	band 1	band 2	band 3	band 4	band 5	band 6
ν (GHz)	90	150	230	275	350	400
R (Ω/m)	5×10^7	5×10^7	5×10^7	5×10^7	5×10^7	5×10^7
ωL (Ω/m)	9.0×10^4	1.5×10^5	2.3×10^5	2.8×10^5	3.5×10^5	4.0×10^5
G (/Ωm)	0	0	0	0	0	0
ωC (/Ωm)	74	126	195	232	289	333
$\lambda_{att}(\mu$m)	23	18	15	13	12	11

Table 3.2: Transverse attenuation lengths in a 1 μm$\times$20 nm TiN microstrip transmission line.

the Nb transmission line. We refer to this attenuation length as the longitudinal attenuation length.

We can straightforwardly derive the relation between coupling strength and position needed to obtain uniform power absorption: the power P in Nb transmission line should decrease linearly as the millimeter wave travels:

$$P(L) = P_0(1 - \frac{L}{L_0}) \tag{3.7}$$

$$\frac{dP(L)}{dL} = -\frac{P(L)}{\lambda(L)} \tag{3.8}$$

where $P(L)$ and $\lambda(L)$ are the power and longitudinal attenuation length in Nb transmission line at position L, $P_0 = P(0)$ is the power at the starting point, and L_0 is the length of Nb section that is coupled with TiN. So we have

$$\begin{aligned} \frac{1}{\lambda(L)} &= -\frac{1}{P}\frac{dP}{dL} \\ &= \frac{1}{L_0}\frac{P_0}{P} \\ &= \frac{1}{L_0}\frac{1}{1 - L/L_0} \end{aligned} \tag{3.9}$$

We simulated the electric current density profiles in Nb microstrip with coupling capacitors from 1 μm^2 to 16 μm^2, as shown in Figure 3.13. We then fit this profile to a lossy open-ended transmission line to extract the longitudinal attenuation length. The results are summarized in Figure 3.10. Different lengths of vertical section of meandered TiN microstrip are used for different millimeter wave bands to facilitate the "coupling strength engineering", as will be discussed next.

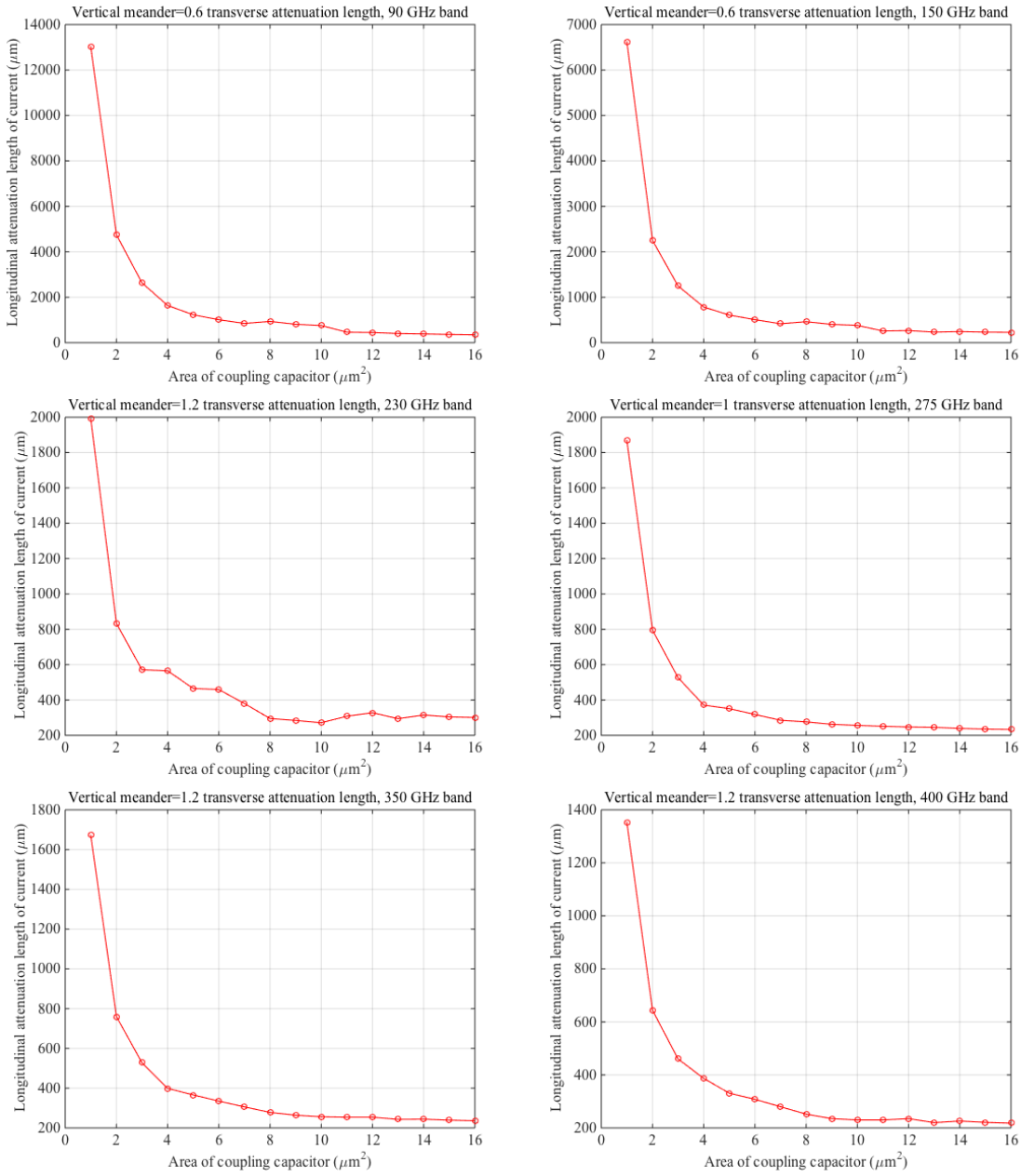

Figure 3.10: Longitudinal attenuation lengths for the 6 millimeter-wave bands.

To obtain the desired linear power absorption profile, we used the results of the above simulation to pick the coupling capacitor area that best matches the desired attenuation length (Eq. 3.9) as a function of position along the Nb transmission line for each band individually. The results are shown in Figure 3.11. The actual profile of coupling strength (staircase blue line) aligns well with the ideal profile (green line).

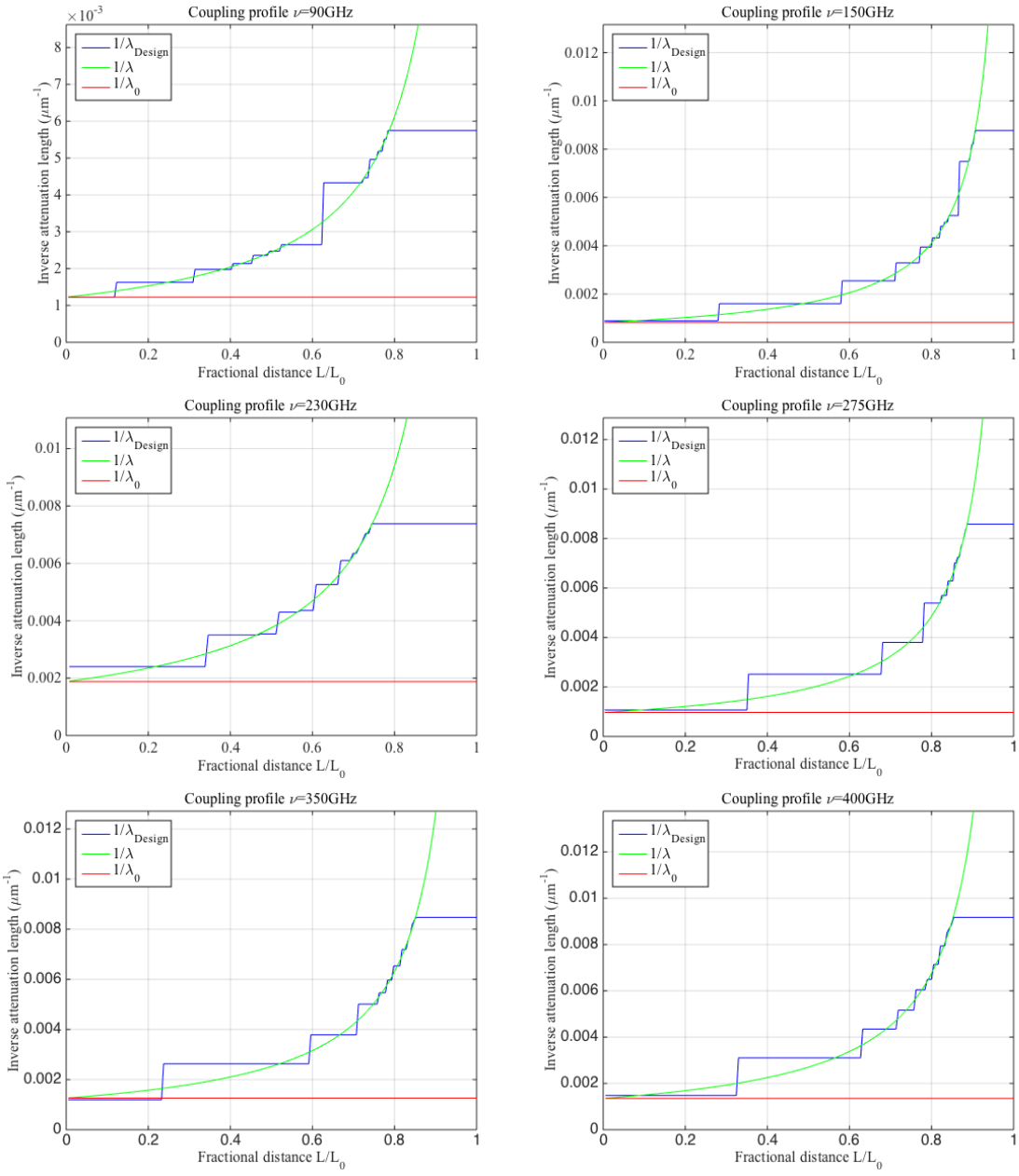

Figure 3.11: Adiabatic coupling scheme. The staircase blue line indicates the actual profile of coupling strength, the green line indicates the ideal profile, and the red line indicates $1/\lambda(0)$ in Eq. 3.9.

The resultant electric current density profiles in the two (upper and lower) Nb microstrips are illustrated in Figure 3.12 for the six bands. Such a profile is in sharp contrast to the exponential profile that one would expect for a constant coupling strength over the entire Nb transmission line. Here the power decays approximately uniformly, validating the above engineering idea of "quasi-continuous coupling". There are several other noticeable features in the profile too. First, the

current vanishes at the right end of Nb microstrip, as required by the open termination condition. Secondly, the oscillation on the scale of a wavelength comes from the interference between right traveling wave and its reflection at the open end: because of the discretization of the capacitor size in units of 1 μm^2, the attenuation length profile does not perfectly match the desired one, and the power profile is not perfectly linear, and thus some unabsorbed power remains at the end and is reflected, creating the this long length scale interference pattern. Thirdly, the oscillation on the scale of a few microns is due to the quasi-continuity of the coupling: the coupling consists of discrete steps, creating small reflections at the points where such steps occur. Fourthly, there are some "smooth" regions. It is found that these regions are coupled only with capacitors marked in red in Figure 3.13. The actual mechanism needs further investigation but is unimportant to our goal here.

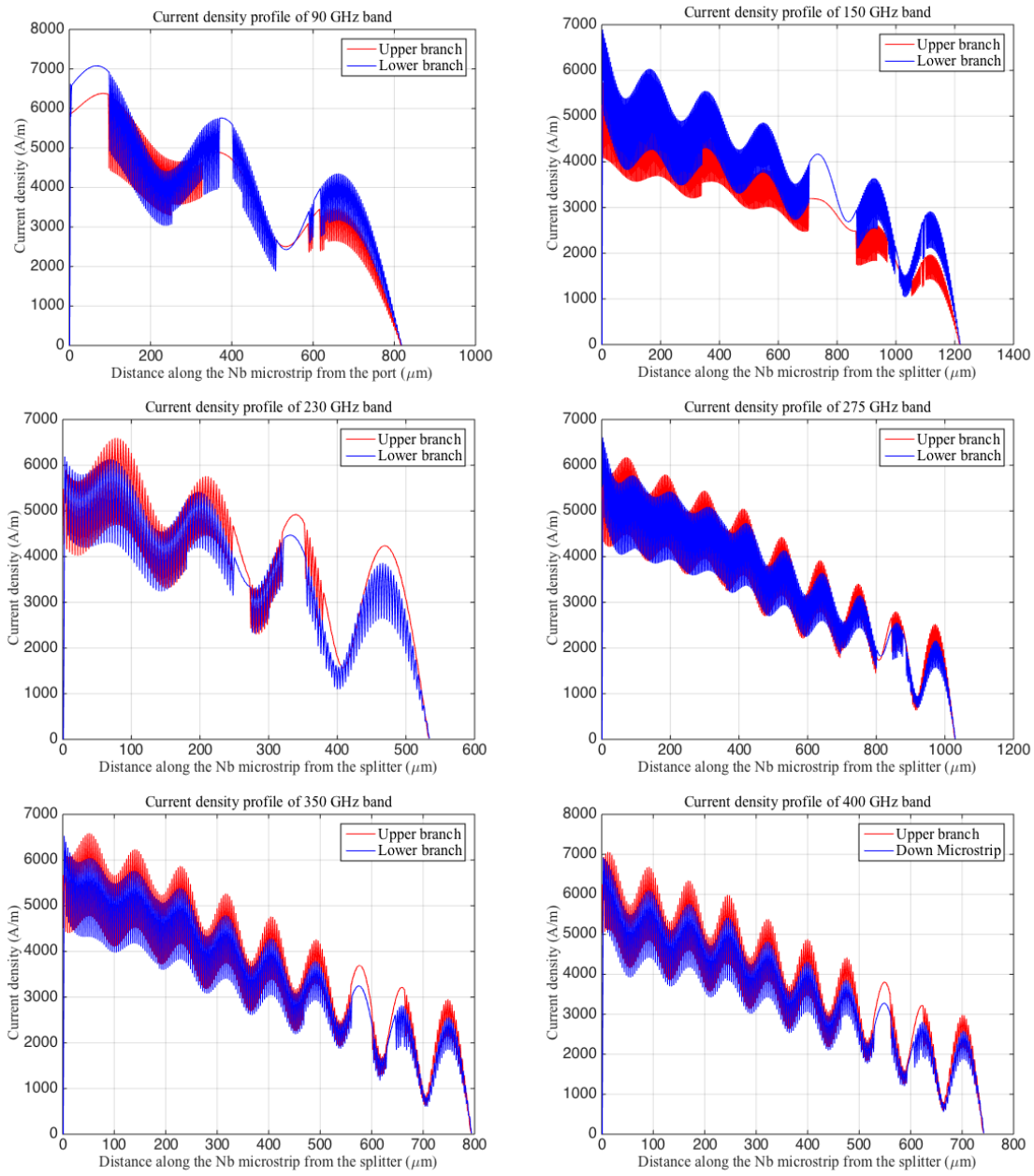

Figure 3.12: Current density in the Nb transmission lines for the six millimeter-wave bands.

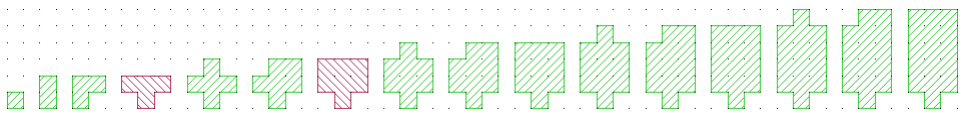

Figure 3.13: Layout of bottom plates in the 16 coupling capacitors.

The electric current density profiles in TiN microstrip for the six bands are shown in Figure 3.14-3.19. The density in each vertical section is very uniform because the length is set to be comparable

with the transverse attenuation length. In the horizontal direction the wavelength-scale oscillations shown in Figure 3.12 are also clearly visible.

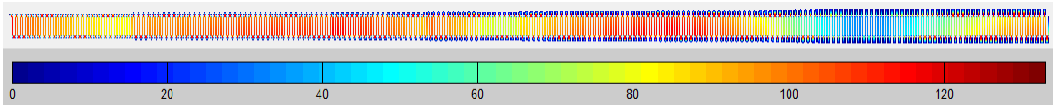

Figure 3.14: Current density in the TiN transmission line for 90 GHz band (unit: A/m).

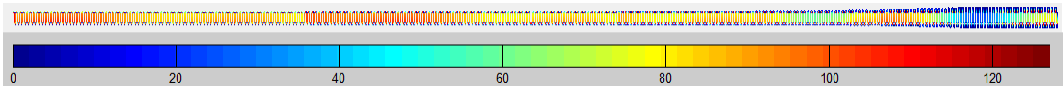

Figure 3.15: Current density in the TiN transmission line for 150 GHz band (unit: A/m).

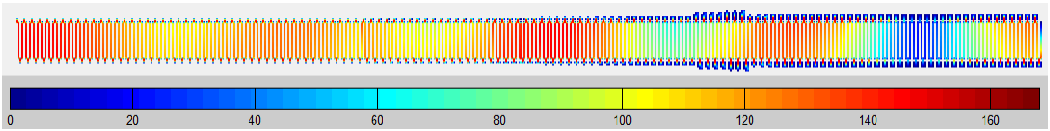

Figure 3.16: Current density in the TiN transmission line for 230 GHz band (unit: A/m).

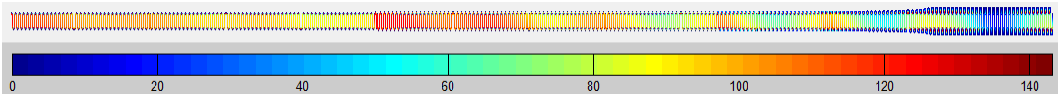

Figure 3.17: Current density in the TiN transmission line for 275 GHz band (unit: A/m).

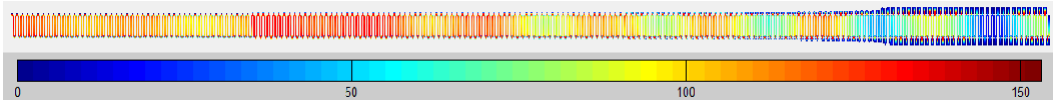

Figure 3.18: Current density in the TiN transmission line for 350 GHz band (unit: A/m).

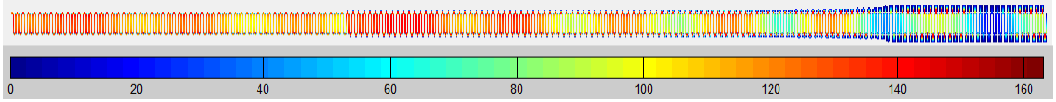

Figure 3.19: Current density in the TiN transmission line for 400 GHz band (unit: A/m).

We can examine the distribution of electric current density in TiN microstrip by creating a histogram, as given by Figure 3.20. Since the quasiparticle density goes like $\sqrt{P}$ in the recombination limited regime, the spread in electric current density gives the spread in quasiparticle density. The distribution has a sharp peak and thus small standard deviation, indicating a uniform deposition of the millimeter wave power.

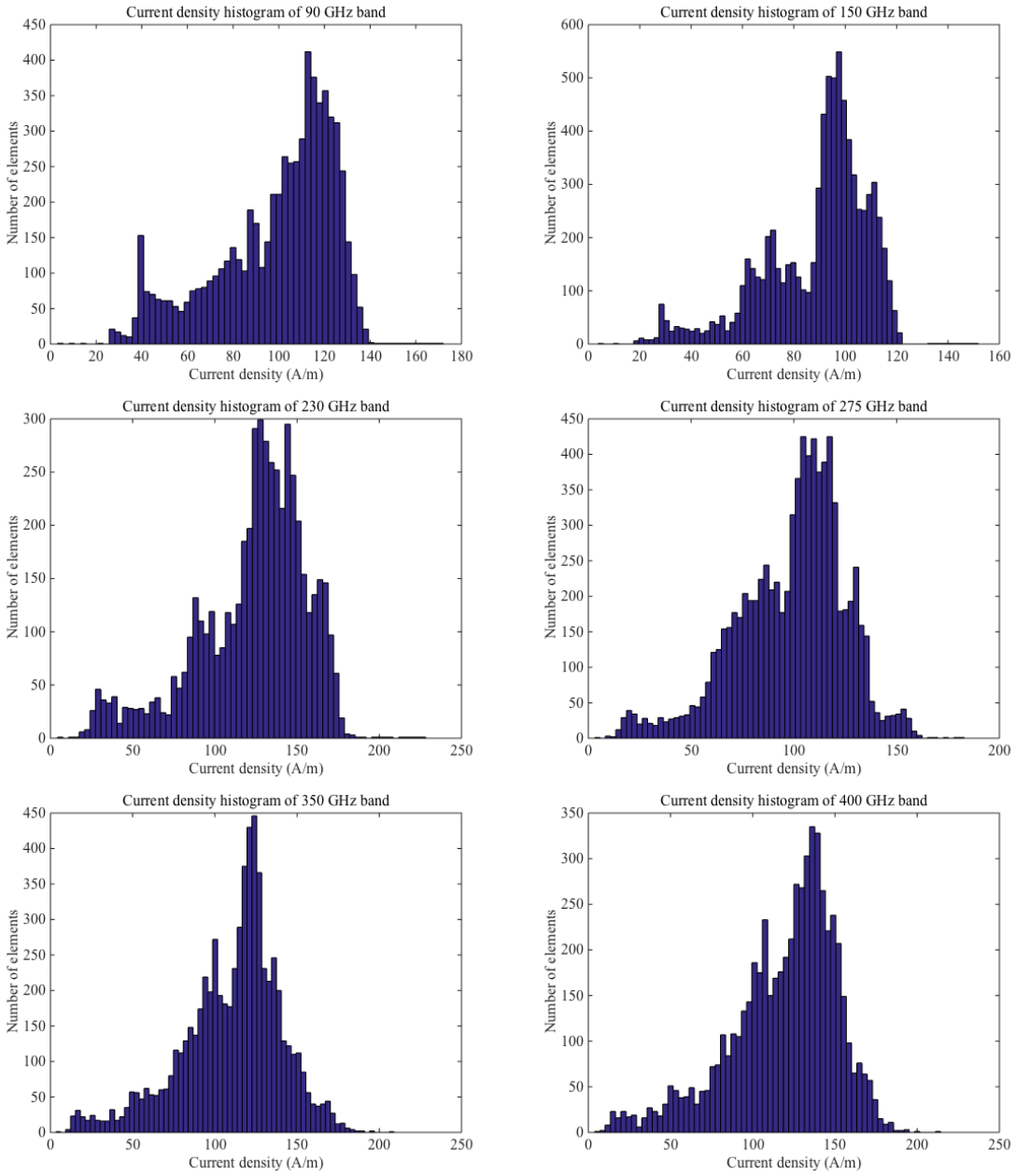

Figure 3.20: Histogram of the current density from 1 μm×1 μm squares in TiN microstrip.

3.1.4 Efficiency of the coupling

The power absorption efficiency of TiN inductor for the six bands is shown in Figure 3.21. The efficiency is generally more than 80% over the entire wide continuous band, attesting to the efficacy of the coupling scheme. The less than 20% reflection is due to slight impedance mismatch at the power splitter. If the microstrip from the antenna is 6 μm instead of 4 μm wide and still splits into two 2 μm wide branches, then the efficiency will approach 100%. It is straightforward to

adiabatically widen the microstrip between the antenna and the power splitter to 6 μm, so this near-100% efficiency can be easily obtained.

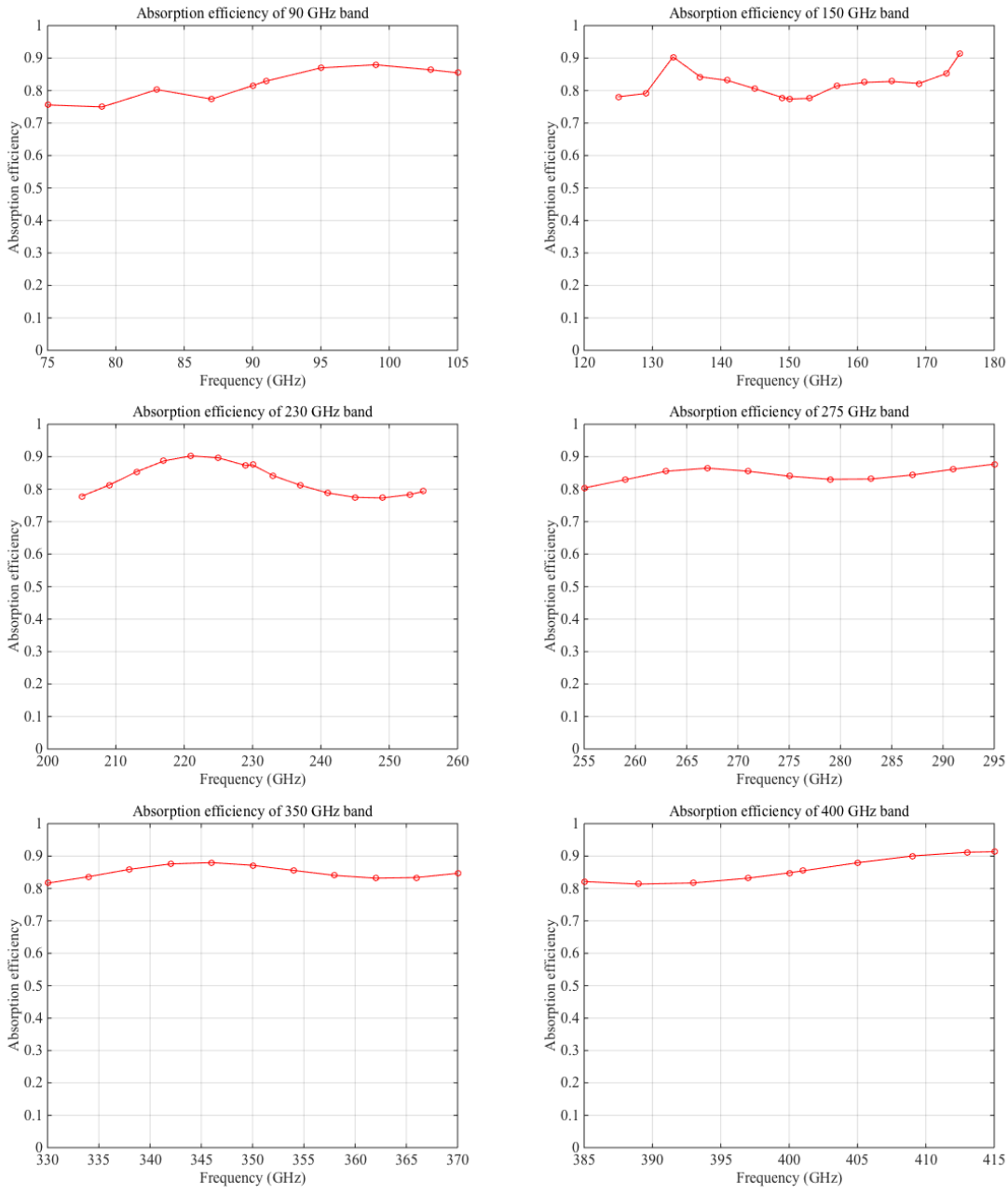

Figure 3.21: Millimeter wave absorption efficiency of TiN inductor.

3.2 Why parallel plate structure

One can make the KID capacitor using an interdigitated structure or a parallel-plate structure. The interdigitated capacitor (IDC) has well controlled TLS noise[15, 16], and it is clear how to design such

a capacitor to render TLS noise subdominant. However, an IDC acts as an antenna, directly receiving mm-wave radiation and routing it to the inductor in a way that bypasses the antenna. Though there have not been lots of tests on TLS noise properties of parallel-plate capacitor, we believe, based on TLS noise data[36] of the microstrip half wavelength resonator/KID using hydrogenated amorphous silicon, that the TLS noise of a parallel-plate capacitor with the same dielectric material can be made acceptably low too, therefore making it a promising substitute for IDC without any risk of stray light absorption. We thus choose parallel plate capacitor for the design of LWCam. We will discuss in detail its potential advantages in terms of TLS noise reduction and elimination of stray light absorption next.

3.2.1 TLS noise reduction

As we reviewed in Chapter 2, experiments have established the fact that KID's phase/frequency noise due to TLS is inversely proportional to the amplitude of electric field and number of TLS fluctuators[8]:

$$\frac{S_{\delta f_r(\nu)}}{f_r^2} \sim \frac{1}{|\vec{E}|N_{TLS}} \sim \frac{1}{|\vec{E}|V_{host}} \tag{3.10}$$

where $\vec{E}$ is the microwave electric field, N_{TLS} is the number of independent TLS fluctuators, and V_{host} is the volume of dielectric material that hosts the many TLS. The parallel-plate structure have significant advantages in terms of TLS noise reduction in both aspects: the electric field within the capacitor can be made arbitrarily strong in principle with a sufficiently thin dielectric layer (though practically there is a lower limit on the dielectric thickness due to the impedance constraint on the Nb microstrip transmission line); the structure can easily extend to large area in fabrication.

3.2.2 Elimination of stray light absorption

Stray light absorption in KID's inductor has three major impacts on its performance: increasing the optical loading and therefore impairing the responsivity (as will be discussed in Chapter 4)[35], adding extra photon noise, and circumventing the spectral and spatial filters. The first two factors would further make it harder for KID to reach the condition of background limited detection.

KID in traditional designs[14] with an IDC suffers from stray light in two ways. First, photons from the environment can be directly picked up by IDC due to its similar structure as the slot antenna and arrive at the inductor. Secondly, any stray light that makes it way around to the

backside of the wafer can bounce around and be absorbed directly by the inductor. The parallel plate capacitor adopted in our design can nicely prevent these from happening. It is obvious that such a structure won't collect light as an antenna and no light can leak through either. In addition, the ground plane only 800nm below the inductor establishes a short circuit ($\vec{E} = \mathbf{0}$) condition, rendering itself a good reflector of free-space electromagnetic field and protecting the inductor.

3.3 Design of the resonator and readout circuit

3.3.1 Components of the resonator and readout circuit

The KID (normally microwave) resonator consists of an inductor L and a capacitor C. The readout line is a standard CPW with 50Ω impedance. The resonator is capacitively coupled with the readout line via a coupling capacitor C_c as shown in Figure 3.22. Note that "coupling capacitor" and "C_c" will refer to the readout coupling capacitor throughout this section and is distinct from the millimeter wave coupling capacitor discussed in section 3.1. Both C and C_c are created by forming a parallel plate structure in the middle and bottom metal layers. The information about millimeter wave intensity is contained in the shift of the resonant frequency, which can be accessed and acquired by sending a (normally microwave) probe signal near the resonance through the readout line. Q_i denotes the internal quality factor of the resonator and Q_c denotes the external quality factor. Q_i mainly comes from the internal dissipation due to the finite quasi-particle density in the inductor, but could also be limited by metal quality or radiation. It is nonetheless not a problem for the resonator geometry discussed here[31]. Q_c comes from the coupling with the readout line via C_c. The values of L, C, Q_i, and Q_c for six millimeter wave bands are determined by an optimization aiming at maximizing the mapping speed, as will be discussed in the next chapter. C_c can be derived based on the following relation[17]. The numbers are listed in Table 3.3.

$$Q_c = \frac{8C}{\omega_0 C_e^2 Z_0} \tag{3.11}$$

$$C_e = (C_c C_g)/(C_c + C_g) \tag{3.12}$$

where C_g is the capacitance between the inductor (TiN microstrip in our case) and ground plane, ω_0 is the angular frequency of the probe signal, and Z_0 is the impedance of the readout CPW.

The dimensions of the resonator and readout circuit for six millimeter wave bands are shown in Figure 3.23 to 3.29. Probe signal travels from port 1 to port 2, coupling with the resonator via C_c.

The ratio of center strip width to the width of gap in CPW is fixed as 3:2 to obtain 50 Ω impedance for matching with the external readout cabling.

Parameter	band 1	band 2	band 3	band 4	band 5	band 6
ν (GHz)	90	150	230	275	350	400
C (pF)	27	17	18	9	9	11
C_c (pF)	1.16	1.37	1.66	2.51	4.89	15.3
C_e (pF)	0.619	0.518	0.575	0.375	0.404	0.520
Q_i	3.9×10^4	3.1×10^4	2.2×10^4	2.3×10^4	1.8×10^4	1.4×10^4

Table 3.3: Coupling capacitance C_c. ν refers to the millimeter wave center frequency.

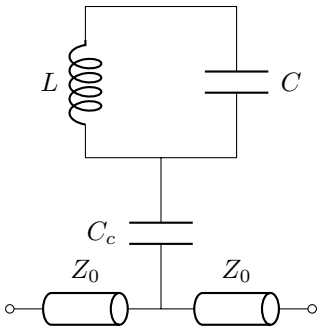

Figure 3.22: Lumped element model of KID's readout circuit.

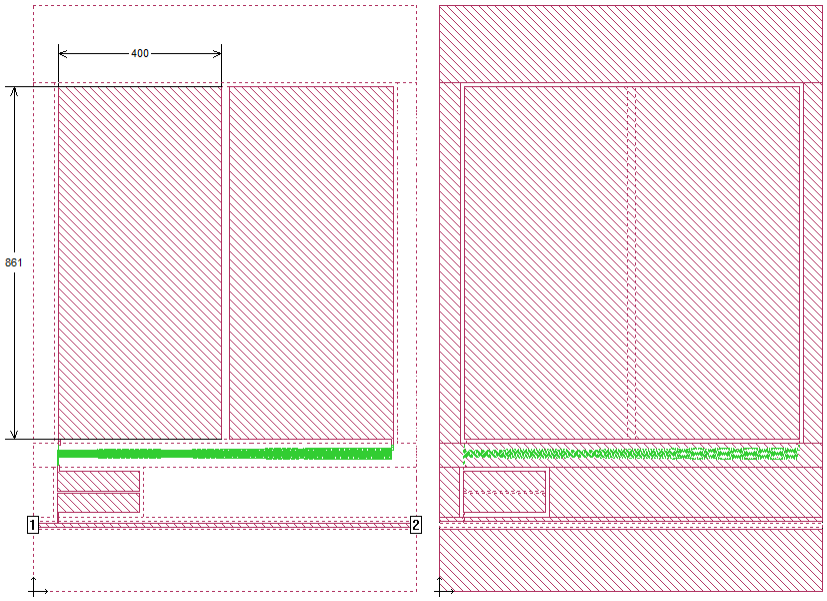

Figure 3.23: Layout of the readout circuit (90 GHz band) in the middle (left) and bottom (right) metal layers (unit: μm). Green part is TiN and red part is Nb.

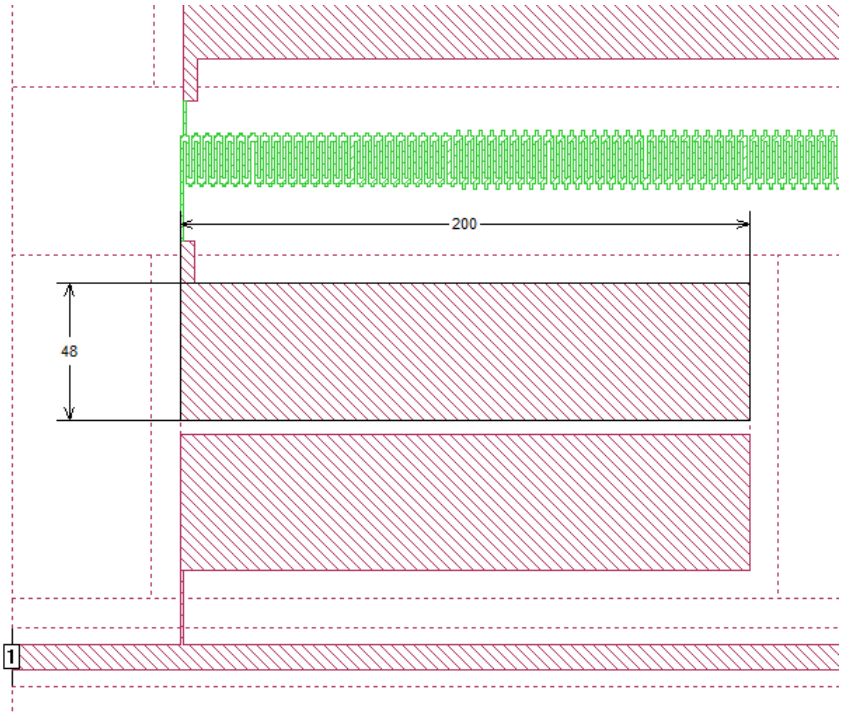

Figure 3.24: Zoomed-in view of the readout circuit (90 GHz) in the middle metal layer (unit: μm). Green part is TiN and red part is Nb.

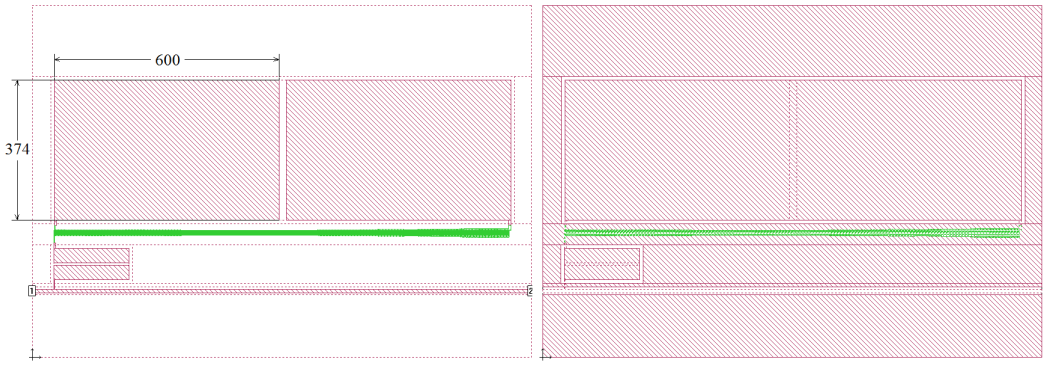

Figure 3.25: Layout of the readout circuit (150 GHz band) in the middle (left) and bottom (right) metal layers (unit: μm). Green part is TiN and red part is Nb.

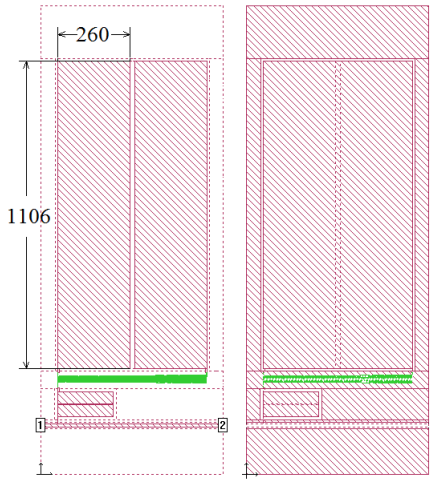

Figure 3.26: Layout of the readout circuit (230 GHz band) in the middle (left) and bottom (right) metal layers (unit: μm). Green part is TiN and red part is Nb.

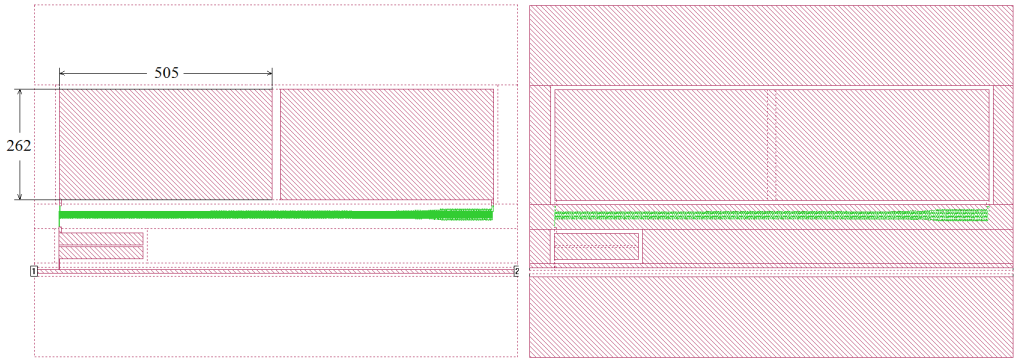

Figure 3.27: Layout of the readout circuit (275 GHz band) in the middle (left) and bottom (right) metal layers (unit: μm). Green part is TiN and red part is Nb.

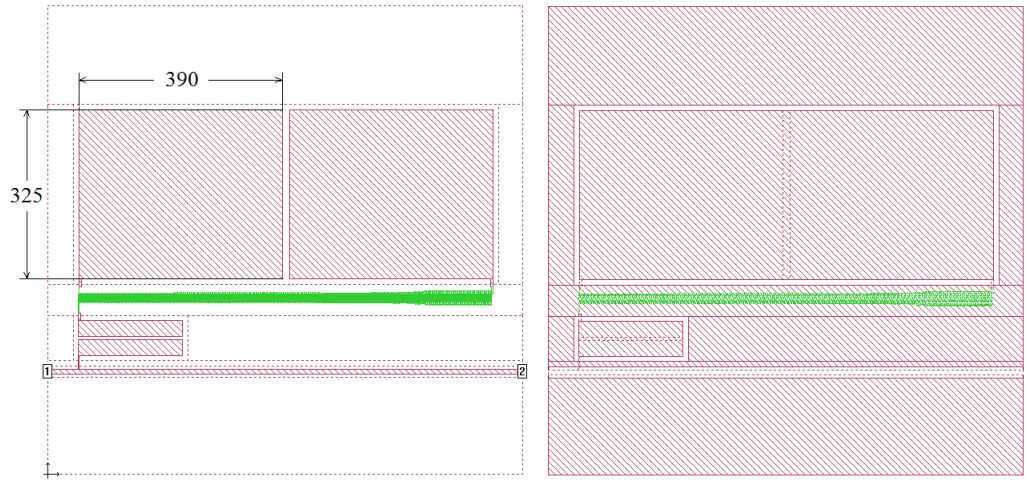

Figure 3.28: Layout of the readout circuit (350 GHz band) in the middle (left) and bottom (right) metal layers (unit: μm). Green part is TiN and red part is Nb.

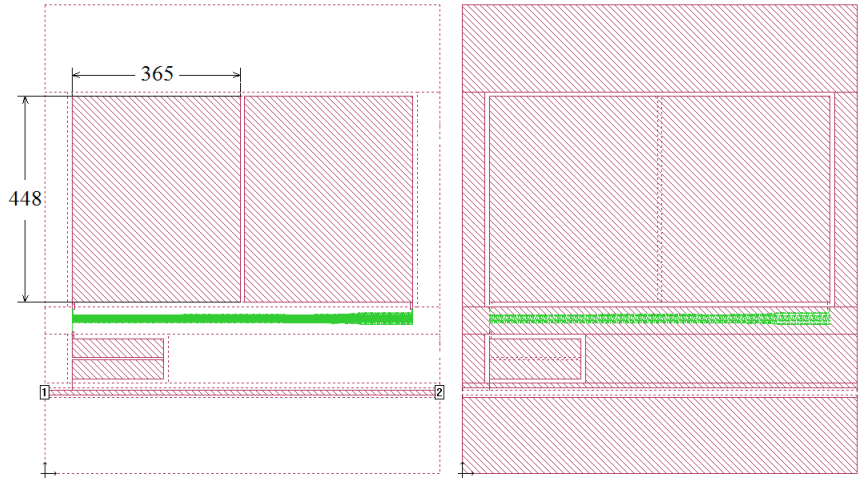

Figure 3.29: Layout of the readout circuit (400 GHz band) in the middle (left) and bottom (right) metal layers (unit: μm). Green part is TiN and red part is Nb.

3.3.2 Transmission coefficients

The transmission coefficient S_{21} of a standard resonator coupled to a readout line can be expressed as follows. We say the resonator is critically coupled when $Q_r = Q_c/2$ and at critical coupling we have $|S_{21}| = |S_{11}| = 1/2$.

$$S_{21}(f) = a(1 - \frac{Q_r/Q_c e^{j\phi_0}}{1 + 2jQ_r((f - f_0)/f_0)}) \tag{3.13}$$

where a is a complex constant accounting for the gain and phase shift through the system, Q_r is the total quality factor, Q_c is the external quality factor, ϕ_0 is the rotation factor, f_0 is the resonant frequency, and f is the frequency of the probe signal.

KID's responsivity dS_{21}/dP_{opt} and internal power (and thus amplitude of electric field in the capacitor) are both maximized when the resonator is critically coupled[8] and our circuits are therefore designed to meet this criteria. We simulated the transmission coefficients from port 1 to port 2 and the results are shown in Figure 3.30. We see that such a requirement is satisfied. The small deviations can be attributed to the non-ideality of the components with a finite size.

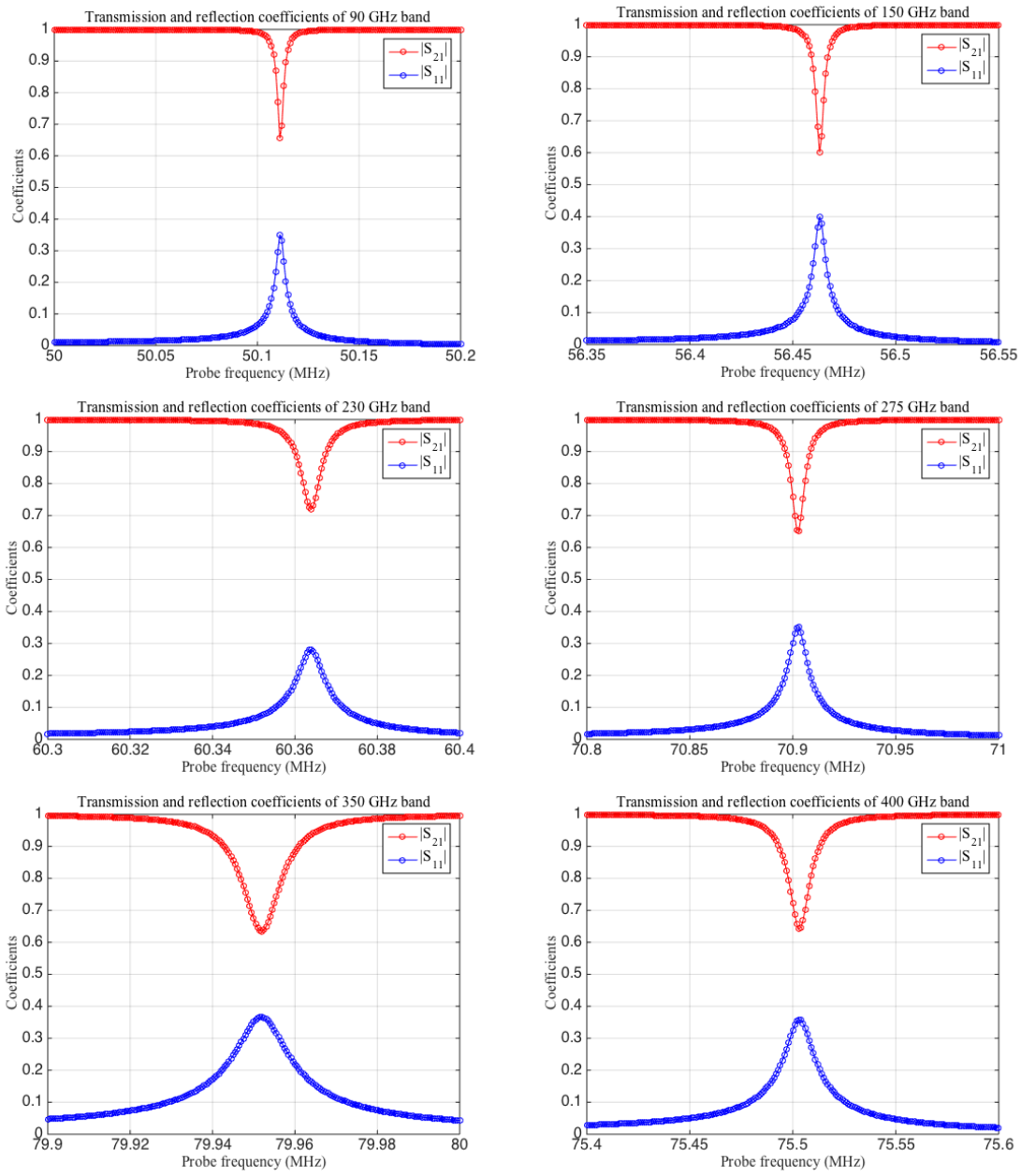

Figure 3.30: Transmission coefficients S_{11} and S_{21}, voltage ratios of reflected and transmitted signals to input signal.

3.4 Procedures of fabrication

We anticipate fabricating the structure on high-resistivity silicon substrates as follows:

1. A 150-nm thick layer of Nb will be deposited by DC-magnetron sputtering and patterned by plasma etching for the ground plane. The patterning will define the KID and readout coupling

capacitor bottom electrode islands. It will also define the edges of the ground plane of the CPW readout feedline. This layer also serves as the ground plane for phased-array antenna, and so slots will be cut in the ground plane for the antenna slots. A border around three edges of the device will also be removed to allow a gold heat-sinking layer that makes direct contact with the silicon substrate later. This heat-sinking layer is necessary to prevent the silicon wafer from heating up due to the absorption of infrared power.

2. A 800-nm thick layer of α-Si:H will be deposited by chemical vapor deposition. No patterning is necessary except to expose a border around three edges of the device for the gold heat-sink layer and at the fourth edge to allow direct electrical contact to the ground plane via wire bonds to the device holder.

3. A 20-nm thick layer of TiN_x will be deposited and patterned by plasma etching for the KID inductor.

4. The 150-nm thick layer of Nb for the KID and readout coupling capacitor top electrodes and the CPW feedline center conductor will then be deposited and patterned. It must make direct contact with the TiN_x to form the KID. It would be simplest to use liftoff for this step, but there are concerns that the Nb will become contaminated by photoresist: either during the ion mill step that is necessary to remove any oxide on the TiN_x so the TiN_x-Nb contact is fully conducting, or during the deposition of the Nb. Such contamination is known to be possible, affecting the microstrip properties. An alternate process would be to deposit SiO_2 and pattern it by plasma etching to create a stencil identical to the liftoff stencil. Ion milling and Nb deposition can then proceed as before. The Nb would be patterned using plasma etching, and then the SiO_2 removed by plasma etching.

5. A 270-nm thick layer of α-Si:H will be deposited by chemical vapor deposition to complete the microstrip dielectric. Again, a border must be removed around the edge of the device.

6. A 450-nm thick layer of Nb will be deposited by DC-magnetron sputtering and patterned by plasma etching to define the microstrip top layer of the microstrip-to-KID mm-wave coupler and for the phased-array antenna. Again, a border around three edges of the device must be removed, and also the fourth edge must be patterned to preserve the CPW feedline gap.

7. A 350-nm thick layer of Au will be deposited by DC-magnetron and patterned using liftoff process. This film provides a 1-mm border around three edges of the device that is used to

heat sink the device using Au wire bonds to the device holder. The Au film overlaps the Nb ground plane so that the wire bonds act to provide RF continuity between the ground plane and the device holder.

Chapter 4

Mapping-speed based optimization of the LWCam design

4.1 Optimization of mapping speed

In Chapter 3 we described the overall architecture of the millimeter wave coupling scheme, design of KID resonator, and readout coupling scheme for LWCam. There we have used many physical parameters such as the dimensions of TiN inductors, capacitances, and quality factors of KID resonator for six millimeter wave bands. In this chapter we will explain how we determined the values of these parameters by performing an optimization to maximize the mapping speed. We start with an introduction to the several realistic criteria that the optimization must satisfy. We then enumerate the constant quantities concerned in the optimization, identify the four parameters to be swept, and derive the several intermediate variables indispensable for the calculation of mapping speed. We walk through the determination of the optimal parameters, present the optimization result, and finally discuss about the fundamental trade-off in our design.

4.1.1 Criteria

As discussed in Chapter 1, the next generation of SZE studies of galaxy clusters will require six spectral bands from 90 GHz to 420 GHz. For this application, we are in parallel developing multi-scale phased array antennas, which use a single antenna structure to cover this wide frequency range in a single detector pixel. The pixel size is varied in a binary fashion with frequency so that all spectral bands use pixels that approximately match the corresponding frequency-dependent Airy function spot size at the focal plane. It is assumed that the antenna structure is 6.66 mm on a side and that this corresponds to a single pixel at 90 GHz and 150 GHz, 4 pixels at 220 GHz and

290 GHz, and 16 pixels at 350 GHz and 420 GHz. Based on the field-of-view constraint and the use of the 6.66 mm multi-scale antenna, the number of detectors that can be accommodated in the focal plane in the absence of any dead area is 880, 880, 3500, 3500, 14000, and 14000. Our goal is to maximize the mapping speed we obtain from this fixed available focal plane area, where the mapping speed in a given band is $N_{det}\Omega_{beam}/\mathrm{NEP}^2$. We also impose the following requirements:

- The mm wave power received at the antenna should be fully absorbed into the TiN absorber rather than being dissipated in the lossy dielectrics. This requires that the equivalent loss tangent of the TiN absorber be much larger than that of the dielectrics.
- The focal plane should be mainly filled with the antenna (live area) rather than KIDs (dead area).
- The detector should reach the fundamental-noise-limited sensitivity.
- The resonator bandwidth Δf must provide enough signal bandwidth given the desired sampling frequency f_{sample}: $\Delta f \geq f_{sample}$.

4.1.2 Constant quantities

The important constant quantities associated with each millimeter wave band are listed in Table 4.1 and we provide the corresponding detailed explanations below.

Band	1	2	3	4	5	6
$T_{sky}(K)$	5	6	10	14	30	57
$T_{dewar}(K)$	14	14	17	20	41	61
T_{tel} (K)	13	13	13	13	27	27
T_{load} (K)	32	33	40	47	98	145
λ (μm)	3300	2000	1330	1050	850	750
ν (GHz)	90	150	230	275	350	400
$\Delta\nu$ (GHz)	35	47	45	40	34	30
FWHM_{Beam} ($'$)	0.53	0.37	0.22	0.20	0.14	0.12
f_{sample} (kHz)	0.68	0.97	1.6	1.8	2.6	3.0
η_{opt}	0.26	0.40	0.34	0.38	0.26	0.29
P_{opt} (pW)	4.0	8.6	8.5	9.9	12	17
η_{ph}	0.81	0.57	0.57	0.57	0.57	0.57
$\mathrm{l}_{antenna}$ (mm)	6.66	6.66	3.33	3.33	1.66	1.66
$\mathrm{N}_{antenna}$	880	880	3500	3500	14000	14000

Table 4.1: Relevant physical constants in the optimization.

- Loading temperatures T_{sky}, T_{dewar} and T_{tel}

  T_{sky}, T_{dewar}, and T_{tel} are the equivalent Rayleigh-Jeans temperatures of the sky, the dewar, and

the telescope. T_{sky} is set by the measured atmospheric precipitable water vapor column at the site (we assumed a 0.55 mm best case based on the data) and an atmospheric model that maps this to opacities and thus optical loading in each band. T_{tel} is set by an estimate of how emissive the telescope will be (5% at $\lambda \geq$1 mm, 10% at $\lambda \leq$1 mm) due to cracks, panel emissivity, and the secondary feed leg structures (which scatter light to 300 K). T_{dewar} is chosen in a somewhat ad hoc way such that $(T_{tel} + T_{sky} + T_{dewar}) = \sqrt{3}(T_{tel} + T_{sky})$. It's hard to predict T_{dewar} ahead of time, but this gives reasonable values based on experience. They together give the loading temperature T_{load} at the detector.

- Millimeter wave center frequency ν and bandwidth $\Delta\nu$

  ν and $\Delta\nu$ are set by the atmospheric windows.

- Full width at half maximum of the Airy disk FWHM_{Beam}

- Sampling frequency f_{sample}

  CCAT's scanning velocity is v=1°/s.

$$f_{sample} = (\mathrm{FWHM}_{Beam}/v/3)^{-1} \times 2 \tag{4.1}$$

- Optical efficiency η_{opt}

  η_{opt} is the overall optical efficiency in the optics from the dewar window to the KID.

- Optical power P_{opt}

  P_{opt} is the optical power received by the KID. Since the antenna is sensitive to only a single polarization, we use the single-polarization form:

$$\mathrm{P}_{opt} = \eta_{opt}(k_B T_{load} \Delta\nu) \tag{4.2}$$

- Photon conversion efficiency η_{ph}

  η_{ph} is the fraction of photon energy that can be converted to excite quasiparticles in the superconductor.

- Side length of the antenna $l_{antenna}$

- Number of antennas $N_{antenna}$

  $N_{antenna}$ is the number of antennas that can be placed in the focal plane for each millimeter wave band assuming no dead area.

Next we list the constant quantities universal for all six millimeter wave bands.

- Superconducting critical temperature of TiN T_c and energy gap Δ

  T_c is tunable pending on the detailed procedure of fabrication[31]. We use $T_c = 1.1$K such that the 90GHz photon is energetically sufficient to break the Cooper pairs. The energy gap is related to critical temperature in BCS theory by the following relation.

$$\Delta = 1.76 k_B T_c \tag{4.3}$$

- Kinetic inductance fraction α

  In KID resonator there are both kinetic inductance and geometric inductance. The ratio of kinetic inductance to total inductance is defined as the kinetic inductance fraction, represented by α. TiN film thinner than 100nm is demonstrated in experiments to exhibit large kinetic inductance with α generally greater than 90%. We thus assume $\alpha = 0.9$ throughout the optimization.

- The γ factor

  γ is defined as the ratio of fractional surface impedance change to fractional conductivity change. In the thin film limit and local limit[8], we know

$$\frac{\delta Z_s}{Z_s} = \gamma \frac{\delta \sigma}{\sigma} \tag{4.4}$$

$$\gamma = -1 \tag{4.5}$$

- Quasiparticle recombination rate R

  R is measured experimentally to be around 100 μm^3/s[31].

- Intrinsic quasiparticle lifetime τ_0

  τ_0 is measured experimentally to be around 0.1 ms[31].

- Operating temperature of the dewar T

  We use $T = 100$ mK$\ll T_c = 1.1$ K so that the density of thermally generated quasi-particles are negligible.

- Single spin electron density of states at the Fermi level N_0

  N_0 is experimentally measured to be around 3.5×10^{10} eVμm^{-3}[32].

- Thermal quasi-particle density n_{qp}^{th}

According to BCS theory we know

$$n_{qp}^{th} = 2N_0\Delta\left(\frac{2\pi k_B T}{\Delta}\right)^{1/2}\exp\left(-\frac{\Delta}{k_B T}\right) = 0.025\ \mu\mathrm{m}^{-3} \tag{4.6}$$

We will see that this is negligible compared to the optically generated quasiparticle density.

- The readout power P_{read} and power dissipated in the resonator P_l

  P_{read} is the power of the probe (normally microwave) signal in the readout line. P_l is the microwave power dissipated in the inductor due to finite density of quasi-particles. Though high power can reduce both TLS and amplifier noises, it does cause problems too. It is known that the kinetic inductance of a superconductor is a nonlinear function of the current. Due to such a nonlinearity, as the readout power is increased, the transmission curve S_{21} becomes distorted and asymmetric, and eventually bifurcates. In the bifurcation regime, response exhibits discontinuous jumps[7]. Therefore, P_{read} and P_l should be kept low enough so that bifurcation does not occur. We choose 1 pW (-90 dBm) based on experience, but we will see later that it could be increased considerably before the bifurcation starts for this design work.

$$\mathrm{P}_{read} = 1\ \mathrm{pW} \tag{4.7}$$

$$\mathrm{P}_l = \mathrm{P}_{read}/2 \tag{4.8}$$

- Amplifier noise temperature T_n

  T_n is measured experimentally to be around 4 K for SiGe BJT amplifiers. We use the BJT because it has good noise temperature in the 100 MHz regime, which is the driving requirement. HEMTs' noise temperatures rise below 1 GHz. In addition, BJTs have good $1/f$ noise.

- Attenuation length of millimeter wave in amorphous Si λ_{Si}^{att}

  The loss tangent δ of a material is given by

$$\tan\delta = \frac{\omega\epsilon'' + \sigma}{\omega\epsilon'} \tag{4.9}$$

  where ω is the angular frequency of the wave, $\epsilon = \epsilon' - j\epsilon''$ is the permittivity, and σ is the

conductivity. In the material power decays exponentially as

$$P(z) = P_0 e^{-\delta k z} \tag{4.10}$$

$$k = 2\pi/\lambda \tag{4.11}$$

where z is the distance that the wave travels in the material and k is the wave number. We can derive the attenuation length for amorphous Si.

$$\delta_{Si} = 7.1 \times 10^{-4} \tag{4.12}$$

$$\lambda_{Si}^{att} = \frac{1}{\delta_{Si}} \frac{\lambda_{free}}{2\pi\sqrt{\epsilon_r^{Si}}} \sim 75\lambda_{free} \tag{4.13}$$

where λ_{free} is the wavelength in free space. δ_{Si} is measured for JPL-deposited amorphous silicon using microstrip resonator structure (private communication, Peter Day). It turns out that in our design the dielectric loss is much smaller than the power dissipation in TiN inductor.

4.1.3 Independent parameters swept during the optimization

In this section we define the four independent parameters swept during the optimization. The optimization will be carried out for six millimeter wave bands separately.

- Attenuation length of millimeter wave in TiN inductor/absorber λ_{TiN}^{att}

  For convenience, we scale λ_{TiN}^{att} by $0.5\lambda_{Si}^{att}$ and consider a discrete set of values of the ratio $\lambda_{TiN}^{att}/0.5\lambda_{Si}^{att}$: 1/1, 1/2, 1/4, 1/8, 1/16, 1/32, 1/64, 1/128, 1/256.

- Length of TiN inductor/absorber l_{abs}

  We sweep l_{abs} over $0.2\lambda_{tot}^{att}$ to $1.8\lambda_{tot}^{att}$, where $\lambda_{tot}^{att} = (\lambda_{Si}^{att-1} + \lambda_{TiN}^{att-1})^{-1}$ refers to the total attenuation length. Such a range corresponds to an absorption efficiency η_{abs} from 20% to 80% assuming the exponential attenuation profile as indicated by Eq. 4.10. We do not go up to η_{abs}=100% because that corresponds to an infinite l_{abs}, which is not doable for an optimization.

- Density of quasiparticles in TiN inductor/absorber n_{qp}

  We sweep n_{qp} over 100 $\mu\mathrm{m}^{-3}$ to 5000 $\mu\mathrm{m}^{-3}$ in step of 100 $\mu\mathrm{m}^{-3}$.

- Thickness of TiN inductor/absorber t_{abs}

  We sweep t_{abs} over 20 nm to 100 nm in step of 10 nm. 20 nm is the minimum thickness of TiN film that can be reliably fabricated so far[31].

While the parameters being swept are not the parameters we directly control physically, they are the parameters over which it is most convenient to do the optimization. Then, from the optimized values, we can extract the physical parameters of the design.

4.1.4 Intermediate variables

In this section we derive the intermediate variables for the calculation of mapping speed.

- Static quasiparticle lifetime τ_{qp} and dynamic quasiparticle lifetime τ_{eff}

$$\tau_{qp} = (Rn_{qp} + 1/\tau_0)^{-1} \tag{4.14}$$

$$\tau_{eff} = (2Rn_{qp} + 1/\tau_0)^{-1} \tag{4.15}$$

- Millimeter wave absorption efficiency in TiN inductor/absorber η_{abs}

$$\eta_{abs} = (1 - \exp\left(-\frac{l_{abs}}{\lambda_{tot}}\right)) \times \frac{\lambda_{TiN}^{att-1}}{\lambda_{tot}^{att-1}} \tag{4.16}$$

- Volume of TiN inductor V

$$\frac{n_{qp}V\Delta}{\tau_{qp}} = \eta_{ph}\eta_{abs}\mathrm{P}_{opt} \tag{4.17}$$

$$V = \frac{\eta_{ph}\eta_{abs}\mathrm{P}_{opt}\tau_{qp}}{n_{qp}\Delta} \tag{4.18}$$

  Note that these equations assume uniform distribution of quasiparticles, which is only approximately true.

- The area of TiN inductor/absorber A_L

$$A_L = \frac{V}{t_{abs}} \tag{4.19}$$

- The width of TiN inductor/absorber w_{abs}

$$w_{abs} = \frac{V}{t_{abs}l_{abs}} \tag{4.20}$$

- The resonant frequency f_0 of KID resonator

Mattis-Bardeen theory gives the relation between f_0 and Q_i of a KID resonator.

$$Q_i = \frac{1}{\alpha|\gamma|\kappa_1(f_0)n_{qp}} \tag{4.21}$$

$$\kappa_1(f_0) = \frac{1}{\pi N_0 \Delta}\left(\frac{2\Delta}{\pi k_B T}\right)^{1/2} \sinh\left(\frac{hf_0}{2k_B T}\right) K_0\left(\frac{hf_0}{2k_B T}\right) \tag{4.22}$$

There is also the requirement that relates sampling frequency f_{sample} with resonator bandwidth Δf, as discussed at the beginning of this chapter.

$$Q_i = 2Q_r = \frac{2f_0}{\Delta f} \leq \frac{2f_0}{f_{sample}} \tag{4.23}$$

By coupling Eq. 4.21 and Eq. 4.23 we can find out a lower bound for f_0 numerically. Figure 4.1 shows the intersection between the two functions of f_0.

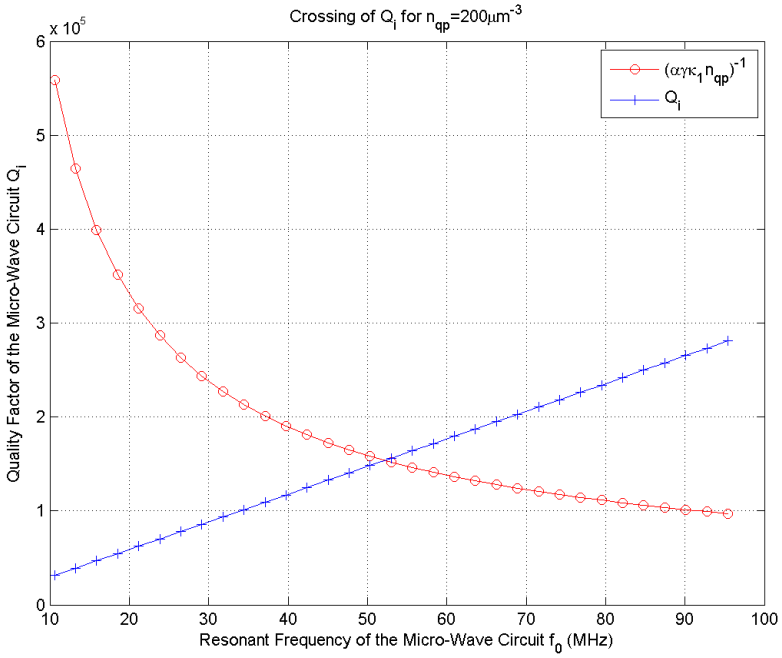

Figure 4.1: Intersections of the two Q_i-related functions. Blue line is the maximum Q_i allowed given the desired sampling frequency and red line is the Q_i implied by the quasiparticle density. The resonant frequency must therefore be in the region where the blue line is higher than the red line. Responsivity increases as f_0 decreases, so we always choose the f_0 at which the two curves intersect except for cases specifically emphasized.

- The internal quality factor Q_i

$$Q_i = \frac{2f_0}{f_{sampling}} \tag{4.24}$$

- The ratio of the imaginary part to the real part of the complex conductivity r_κ

$$\kappa = \frac{\delta\sigma/|\sigma|}{\delta n_{qp}} = \kappa_1 + j\kappa_2 \tag{4.25}$$

$$r_\kappa = \frac{\kappa_2}{\kappa_1} = \frac{\pi}{4}(\frac{2\pi k_B T}{\Delta})^{1/2} \frac{1 + (\frac{2\Delta}{\pi k_B T})^{-1/2} \exp(-\frac{hf_0}{2k_B T}) I_0(\frac{hf_0}{2k_B T})}{\sinh(\frac{hf_0}{2k_B T}) K_0(\frac{hf_0}{2k_B T})} \tag{4.26}$$

where σ is the complex conductivity of the superconductor.

- Total inductance of TiN inductor L

$$L = \mu_0 \lambda_{eff}(t_{abs}) \frac{l_{abs}}{w_{abs}} \frac{1}{\alpha} \tag{4.27}$$

where $\lambda_{eff}(t_{abs})$ is the effective penetration depth of TiN.

- Capacitance of KID capacitor C

$$C = \frac{1}{(2\pi f_0)^2 L} \tag{4.28}$$

- Area of the ideal (parallel plate structure without virtual floating ground) KID capacitor A_C

$$A_C = \frac{C t_{Si}}{\epsilon_r^{Si} \epsilon_0} \tag{4.29}$$

where $t_{Si} = 0.8$ μm is the thickness of middle dielectric layer.

- Area of the actual (parallel plate structure with a virtual floating ground) KID capacitor A_C^{Tot}

$$A_C^{Tot} = 4A_C \tag{4.30}$$

This factor of 4 appears because the true area of the capacitor is split into two capacitors and they are put in series.

- Side length of the coupling capacitor l_{C_c}

$$Q_c = Q_i \tag{4.31}$$

$$Z_0 = 50\Omega \tag{4.32}$$

$$C_c = \left(\frac{8C}{2\pi f_0 Q_c Z_0}\right)^{1/2} \tag{4.33}$$

$$l_{C_c} = \left(\frac{C_c}{C} A_C\right)^{1/2} \tag{4.34}$$

- Photon noise equivalent power NEP_{ph}

$$\mathrm{NEP}_{ph} = \left(2P_{opt}h\nu + \frac{2P_{opt}^2}{\Delta\nu}\right)^{1/2} \tag{4.35}$$

The incident millimeter wave photons from the background (dewar, telescope, and sky) obey Bose-Einstein statistics and have an intrinsic fluctuation in each mode: $\bar{n}_{ph}(1+\bar{n}_{ph})$, where $\bar{n}_{ph} = (e^{h\nu/k_BT} - 1)^{-1}$. This is the photon noise.

- Recombination noise equivalent power NEP_r

$$\mathrm{NEP}_r = \left(\left(\frac{dP_{opt}}{dn_{qp}}\right)^2 \tau_{eff}^2 S_r\right)^{1/2} = \left(\left(\frac{V\Delta}{\eta_{abs}\eta_{ph}\tau_{eff}}\right)^2 \tau_{eff}^2 \left(\frac{4}{V} R n_{qp}^2\right)\right)^{1/2} \tag{4.36}$$

where S_r is the power spectral density of quasiparticle recombination rate $r(t)$. In the steady state under optical loading the detector maintains a dynamic equilibrium of the quasiparticles. $R(t) = \frac{1}{2}r(t)V$ is the rate at which the recombination events occur in volume V. Such a process is a point Poisson process $\langle R(t)R(t')\rangle = \langle R(t)\rangle\delta(t-t')$, which induces the fluctuation in quasiparticle density and recombination noise.

- Generation noise equivalent power NEP_g

$$\mathrm{NEP}_r = \left(\left(\frac{dP_{opt}}{dn_{qp}}\right)^2 \tau_{eff}^2 S_g\right)^{1/2} = \left(\left(\frac{V\Delta}{\eta_{abs}\eta_{ph}\tau_{eff}}\right)^2 \tau_{eff}^2 \left(\frac{4}{V} R \left(n_{qp}^{th}\right)^2\right)\right)^{1/2} \tag{4.37}$$

The reverse process, in which thermal phonons break Cooper pairs, gives the generation noise. The generation noise is often negligible since the operating temperature is usually much lower than the transition temperature $T \ll T_c$ and $n_{qp}^{th} \ll n_{qp}$.

- Decay noise equivalent power NEP_d

$$\mathrm{NEP}_d = \left(\left(\frac{dP_{opt}}{dn_{qp}} \right)^2 \tau_{eff}^2 S_d \right)^{1/2} = \left(\left(\frac{V\Delta}{\eta_{abs}\eta_{ph}\tau_{eff}} \right)^2 \tau_{eff}^2 \frac{2}{V} \frac{n_{qp}}{\tau_0} \right)^{1/2} \tag{4.38}$$

The quasiparticles can decay through an intrinsic process (as opposed to recombination process) characterized by a lifetime τ_0. Similarly such a point Poisson process induces the decay noise. Decay noise is negligible compared with the recombination noise in the high quasiparticle density limit.

- Amplifier noise equivalent power NEP_{amp}

$$\mathrm{NEP}_{amp} = \sqrt{S^{\mathrm{HEMT}}_{\delta n_{qp}/n_{qp}}} \left| \frac{dn_{qp}/n_{qp}}{dp} \right|^{-1} = \left(\frac{8k_B T_n}{P_l r_\kappa^2} \right)^{1/2} \left(\frac{V\Delta}{\eta_{abs}\eta_{ph}\tau_{eff}} n_{qp} \right) \tag{4.39}$$

KID uses uses a cryogenic low noise amplifier, either a high-electron-mobility transistor (HEMT) or a silicon-germanium bipolar-junction transistor (BJT), to amplify the transmitted signal. The amplifier adds white noise with the above NEP. The amplifier can also have $1/f$ gain fluctuation noise, which we do not consider since it can be subtracted using off-resonance monitor tones.

- Amplitude of the electric field in KID capacitor E

$$Energy = \frac{Q_i P_l}{2\pi f_0} \tag{4.40}$$

$$U = \left(\frac{2Energy}{C} \right)^{1/2} \tag{4.41}$$

$$E = \frac{U}{t_{abs}} \tag{4.42}$$

where $Energy$ is the maximum energy stored in KID capacitor, U is the voltage in KID capacitor.

- Actual current density in KID inductor J, critical current density J_c for bifurcation

$$I = \left(\frac{2Energy}{L} \right)^{1/2} \tag{4.43}$$

$$J = \frac{I}{w_{abs} t_{abs}} \tag{4.44}$$

$$\rho = \mu_0 \lambda_{eff} \frac{\pi \Delta t_{abs}}{\hbar} \tag{4.45}$$

$$J_c = 0.42 \left(\frac{\pi N_0 \Delta^3}{\hbar \rho} \right)^{1/2} \tag{4.46}$$

where I is the magnitude of current in KID inductor.

- TLS noise power spectral density S_f^{TLS} and associated noise equivalent power $\mathrm{NEP}_{TLS}^{phase}$

$$S_{f_{exp}}^{TLS} = 4.1 \times 10^{-18}\ \mathrm{Hz}^{-1} \tag{4.47}$$

$$E_{exp} = 6000\ \mathrm{V/m} \tag{4.48}$$

$$f_{exp} = 1000\ \mathrm{Hz} \tag{4.49}$$

$$f_{LWCam} = 10\ \mathrm{Hz} \tag{4.50}$$

$$S_f^{TLS} = S_{f_{exp}}^{TLS} \left(\frac{T}{100\ \mathrm{mK}}\right)^{-1.7} \left(\frac{A_c^{Tot}}{0.016\ \mathrm{mm}^2/2}\right)^{-1} \left(\frac{f_{LWCam}}{f_{exp}}\right)^{-1/2} \left(\frac{E}{E_{exp}}\right)^{-1} \tag{4.51}$$

$$\mathrm{NEP}_{TLS}^{phase} = \left(S_{f_{exp}}^{TLS}\right)^{1/2} \left|\frac{\delta f_r/f_r}{\delta p}\right|^{-1} = \left(S_{f_{exp}}^{TLS}\right)^{1/2} \left|-\frac{r_\kappa}{2Q_i}\frac{1}{2P_{opt}}\right|^{-1} \tag{4.52}$$

where $S_{f_{exp}}^{TLS}, E_{exp}, f_{exp}$ are the experimentally measured TLS noise power spectral density, inferred amplitude of the electric field, and operating frequency[36]. In the reference, the MKID is a half wavelength microstrip resonator made of Al with amorphous Si as the dielectric material. One end of the microstrip resonator overlaps with the center strip of the CPW (readout line) to create a capacitive coupling while the other end is left unterminated. The electric field E_{exp} we used here is the inferred amplitude of the electric field at the open end. f_{LWCam} is the operating frequency or the frequency of the astronomical signal of LWCam.

- Fundamental noise equivalent power NEP_{fund}

$$\mathrm{NEP}_{fund} = (\mathrm{NEP}_{ph}^2 + \mathrm{NEP}_g^2 + \mathrm{NEP}_r^2 + \mathrm{NEP}_d^2)^{1/2} \tag{4.53}$$

- Area of a single pixel

$$A_{Pixel} = A_{Antenna} + 25 \times (A_C^{Tot} + A_L) \tag{4.54}$$

The factor 25 is to account for the fact that a single antenna couples to detectors from multiple spectral bands. It comes from the following estimation: $25 = [A_C^{Tot}(\nu = 90\ \mathrm{GHz}) \times 1 + A_C^{Tot}(\nu = 150\ \mathrm{GHz}) \times 1 + A_C^{Tot}(\nu = 230\ \mathrm{GHz}) \times 4 + A_C^{Tot}(\nu = 275\ \mathrm{GHz}) \times 4 + A_C^{Tot}(\nu = 350\ \mathrm{GHz}) \times 16 + A_C^{Tot}(\nu = 400\ \mathrm{GHz}) \times 16]/[A_C^{Tot}(\nu = 90\ \mathrm{GHz}) + A_C^{Tot}(\nu = 150\ \mathrm{GHz}) + A_C^{Tot}(\nu = 230\ \mathrm{GHz}) + A_C^{Tot}(\nu = 275\ \mathrm{GHz}) + A_C^{Tot}(\nu = 350\ \mathrm{GHz}) + A_C^{Tot}(\nu = 400\ \mathrm{GHz})]$.

- Actual number of pixels

$$N_{pixel} = \frac{A_{FocalPlane}}{A_{Pixel}} \tag{4.55}$$

- Mapping speed v_{Mapping}

$$v_{\text{Mapping}} \sim \frac{N_{Pixel}}{\left(\text{NEP}^{Tot}_{phase}\right)^2} = \frac{N_{Pixel}}{\left(\text{NEP}^{TLS}_{phase}\right)^2 + \text{NEP}^2_{amp} + \text{NEP}^2_{fund}} \tag{4.56}$$

The mapping speed normally includes a factor of Ω_{beam} but we have dropped it because it is a constant irrelevant to the optimization.

4.1.5 Determination of optimal parameters

Among the four parameters swept, we will first examine and interpret the dependence of several intermediate variables and finally mapping speed of the six millimeter wave bands on n_{qp} and l_{abs} for fixed $\lambda^{att}_{TiN}/0.5\lambda^{att}_{Si}$ and t_{abs}. We take $\lambda^{att}_{TiN}/0.5\lambda^{att}_{Si} = 1/32$ (or $\lambda^{att}_{TiN} = 3.6$ mm) and $t_{abs} = 20$ nm of 90 GHz band as an example. Similar conclusions hold for the rest of the parameter space.

- Inductance L and side length l_C of the capacitor

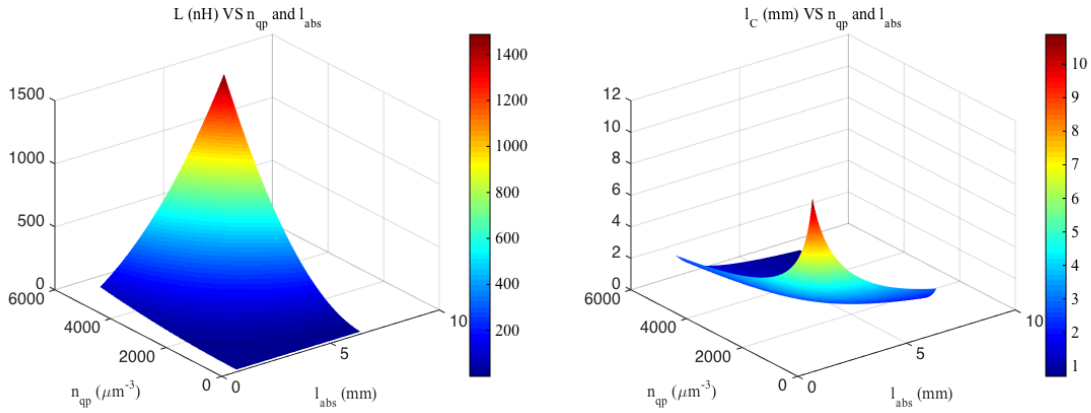

Figure 4.2: Inductance L and side length l_C of the capacitor (90 GHz band) for the case of $\lambda^{att}_{TiN}/0.5\lambda^{att}_{Si} = 1/32$ and $t_{abs} = 20$ nm.

We can make the following qualitative analysis for L and C.

$$L \propto \frac{l_{abs}}{w_{abs}} \propto \frac{l_{abs}}{\frac{V}{t_{abs} l_{abs}}} \propto \frac{l_{abs}^2}{V} \propto l_{abs}^2 n_{qp}^2 \tag{4.57}$$

$$C = \frac{1}{(2\pi f_0)^2 L} \propto \frac{n_{qp}}{L} \propto l_{abs}^{-2} n_{qp}^{-1} \tag{4.58}$$

Therefore with low quasiparticle density and short inductor the area of KID capacitor tends to be large and reduces the filling fraction of live (antenna) area in the focal plane.

- Filling fraction of live area A_{Live}/A_{Pixel} and number of pixels N_{Pixel}

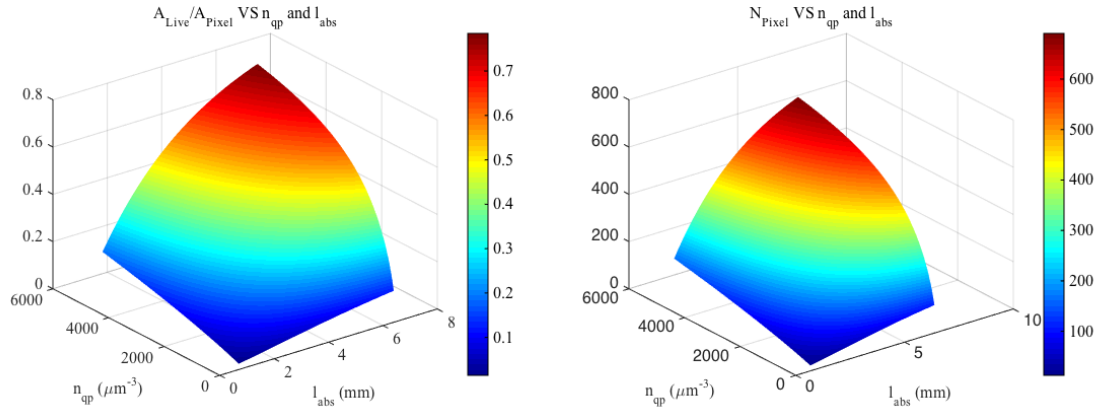

Figure 4.3: Filling fraction of live area A_{Live}/A_{Pixel} and number of pixels N_{Pixel} (90 GHz band) for the case of $\lambda_{TiN}^{att}/0.5\lambda_{Si}^{att} = 1/32$ and $t_{abs} = 20$ nm.

Figure 4.3 shows that the filling fraction of live area in the focal plane A_{Live}/A_{Pixel} is approximately inversely proportional to A_C^{Tot}, consistent with our expectation. Therefore, with higher quasiparticle density and longer inductor the focal plane can accomodate more pixels.

- Responsivity and TLS noise equivalent power NEP_{phase}^{TLS}

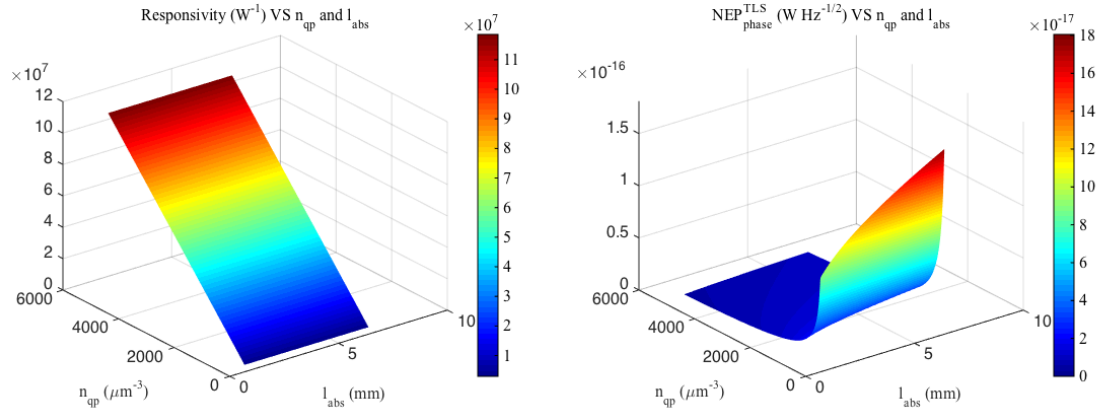

Figure 4.4: Responsivity and TLS noise equivalent power NEP^{TLS}_{phase} (90 GHz band) for the case of $\lambda^{att}_{TiN}/0.5\lambda^{att}_{Si} = 1/32$ and $t_{abs} = 20$ nm.

We can make the following qualitative analysis for responsivity and TLS noise equivalent power NEP^{TLS}_{phase}:

$$\frac{\delta f_r/f_r}{\delta p} = \frac{\delta f_r/f_r}{\delta n_{qp}/n_{qp}} \frac{\delta n_{qp}/n_{qp}}{\delta p} = -\frac{\gamma_\kappa}{2Q_i} \frac{1}{2P_{opt}} \propto Q_i^{-1} \propto n_{qp} \tag{4.59}$$

$$\text{NEP}_{\text{TLS}} \propto \left| \frac{\delta f_r/f_r}{\delta p} \right|^{-1} \propto n_{qp}^{-1} \tag{4.60}$$

Therefore, the TLS noise equivalent power is approximately inversely proportional to the quasi-particle density. We also see that TLS noise has nothing to do with the lifetime of quasi-particles τ_{qp} in the system according to the conversion factor $\frac{\delta f_r/f_r}{\delta p}$. The low quasiparticle density corresponds to a big inductor.

- Fundamental noise equivalent power NEP_{fund} and total noise equivalent power NEP^{Tot}_{phase}

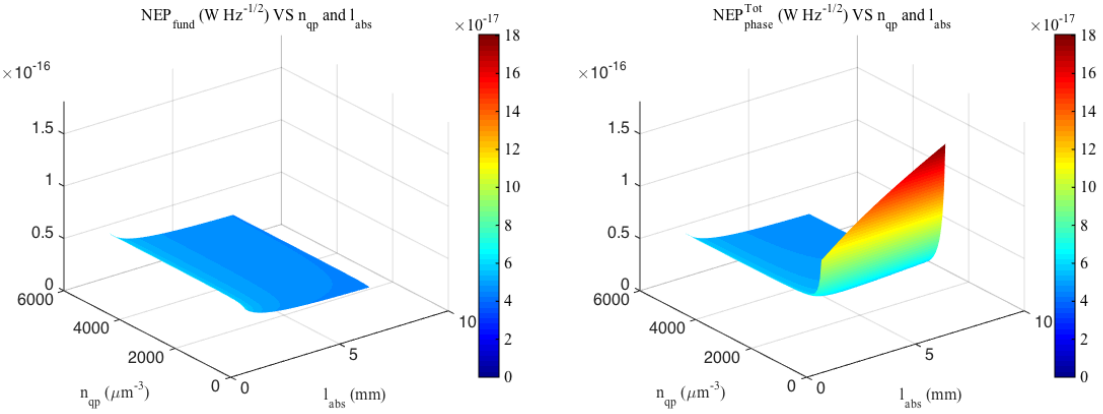

Figure 4.5: Fundamental noise equivalent power NEP_{fund} and total noise equivalent power NEP^{Tot}_{phase} (90 GHz band) for the case of $\lambda^{att}_{TiN}/0.5\lambda^{att}_{Si} = 1/32$ and $t_{abs} = 20$ nm.

Figure 4.5 shows that the fundamental noise equivalent power is almost constant and the total noise equivalent power rises up quickly when the quasiparticle density drops below certain value. Such a rise is due to the dominance of TLS noise over the fundamental noise at low quasiparticle density.

- Critical current density J_c and actual current density J

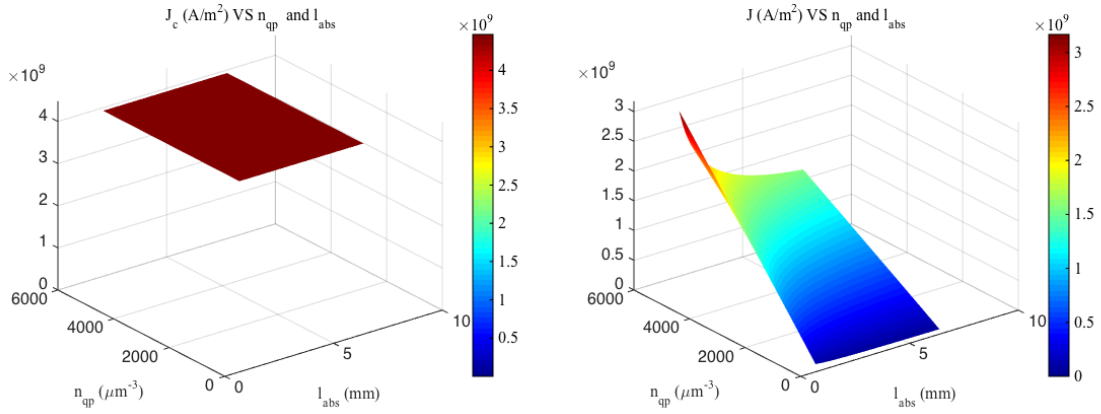

Figure 4.6: Critical current density J_c and actual current density J (90 GHz band) for the case of $\lambda_{TiN}^{att}/0.5\lambda_{Si}^{att} = 1/32$ and $t_{abs} = 20$ nm.

Figure 4.6 shows that for high density of quasiparticles and long inductor the actual current density J is significantly lower than the critical value $0.88J_c$, where the bifurcation starts.

- Width of TiN inductor/absorber w_{abs} and mapping speed

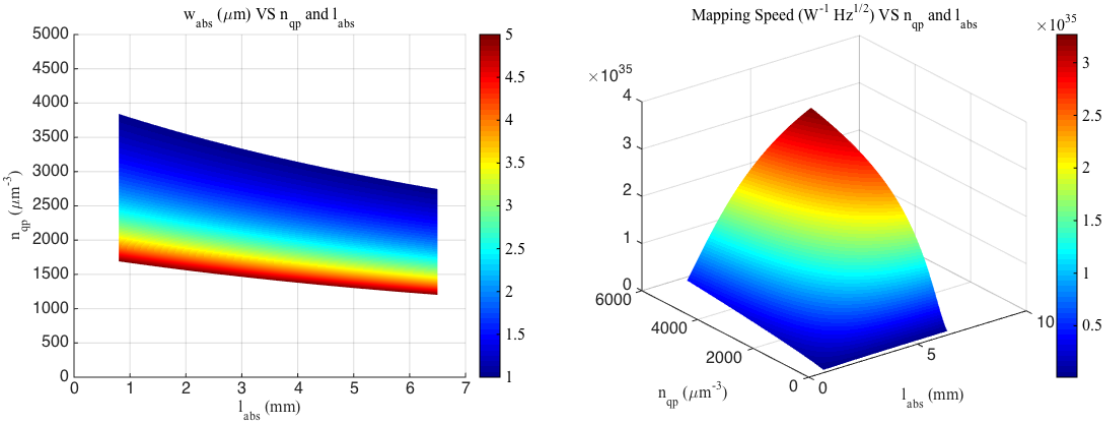

Figure 4.7: Width of TiN inductor/absorber w_{abs} and mapping speed (90 GHz band) for the case of $\lambda_{TiN}^{att}/0.5\lambda_{Si}^{att} = 1/32$ and $t_{abs} = 20$ nm.

Figure 4.7 shows that the mapping speed grows with higher density of quasiparticles and longer inductor. We also know that inductors with width less than 1μm can not be reliably fabricated.

Therefore we can conclude that for fixed $\lambda_{TiN}^{att}/0.5\lambda_{Si}^{att}$ and t_{abs}, the largest mapping speed corresponds to $w_{abs} = 1$ μm and $l_{abs} = 1.8\lambda_{TiN}^{att}$.

Next we check the dependence of mapping speed on $\lambda_{TiN}^{att}/0.5\lambda_{Si}^{att}$ and t_{abs} with fixed $w_{abs} = 1$ μm and $l_{abs} = 1.8\lambda_{TiN}^{att}$. Figure 4.8 shows that the maximum mapping speed corresponds to the thinnest inductor (20 nm) and different $\lambda_{TiN}^{att}/0.5\lambda_{Si}^{att}$. Table 4.2 summarizes the resultant parameters of the six millimeter wave bands. In all cases, the total sensitivities are within 10% to 25% of the fundamental noise limit and the number of pixels in each band is over 75% of the expected number of pixels assuming no dead area, as was our goal.

Since our parameter sweep only goes up to η_{abs}=80%, a natural question to ask is would 100% efficiency be better in terms of mapping speed. We think the answer is positive based on the trend revealed by our analysis (and by common sense). This can be readily checked by tweaking the parameter space to include η_{abs}=100% in this optimization. Nonetheless, it is worth pointing out that the conclusion that η_{abs}=80% is optimal does not dictate the actual millimeter wave absorption efficiency in the design. This is just a "guidance". The actual efficiency depends on how we engineer the profile of the coupling capacitors as discussed in last chapter and it is essentially decoupled from the result of the optimization. It has the freedom to be any value between 0% and 100%. Assuming we adopt the physical dimensions and quality factors listed in Table 4.2 for the KID, if we make η_{abs}=80% by properly engineering the coupling capacitors, we then get the great mapping speed as yielded exactly from the optimization. We can certainly make η_{abs}=100% too and the resultant mapping speed might be slightly better.

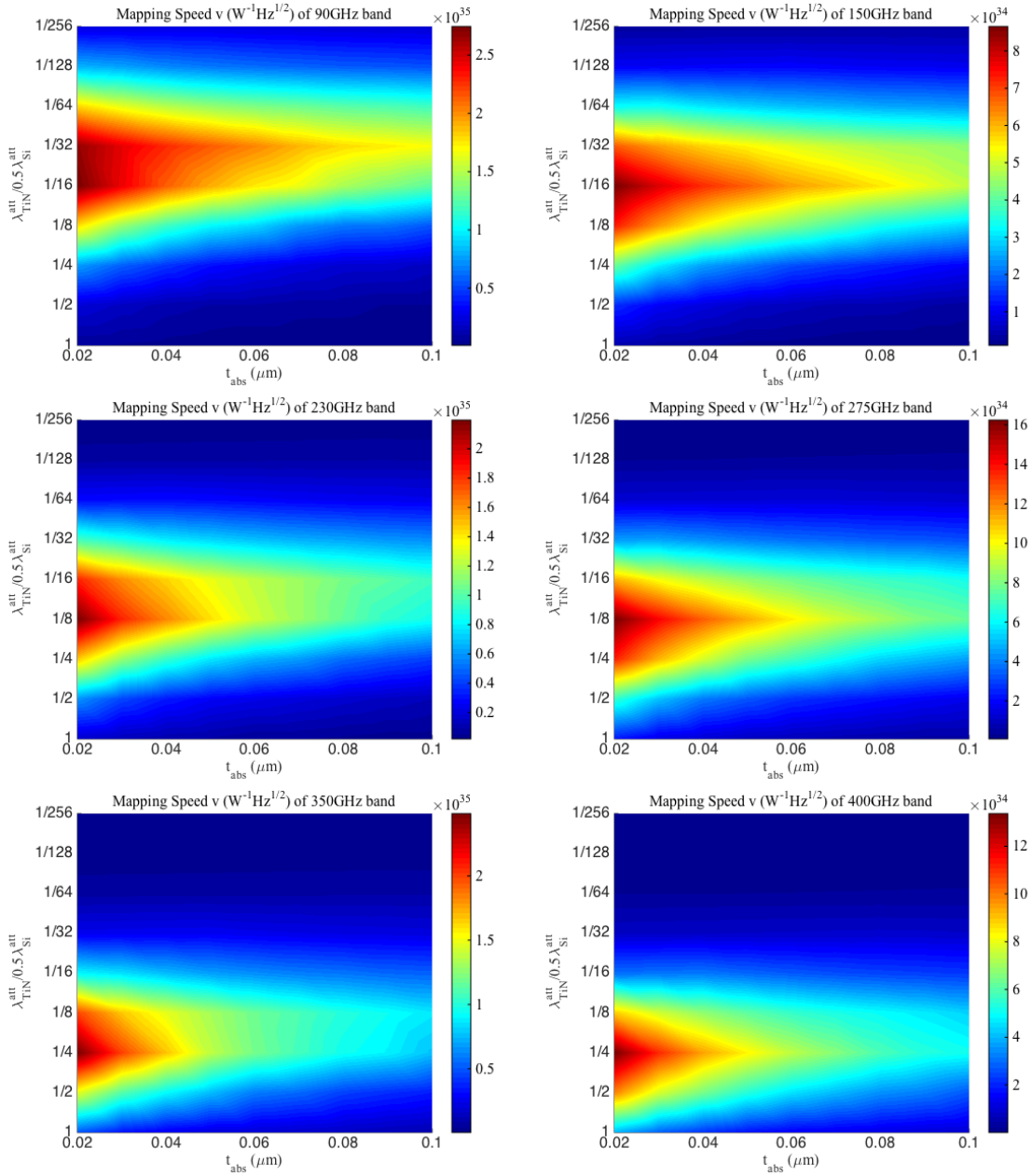

Figure 4.8: Dependence of mapping speed on $\lambda_{TiN}^{att}/0.5\lambda_{Si}^{att}$ and t_{abs} with fixed $w_{abs} = 1$ μm and $l_{abs} = 1.8\lambda_{TiN}^{att}$ for six millimeter wave bands.

Band	1	2	3	4	5	6
l_{abs} (mm)	6.5	7.9	5.3	8.2	6.7	5.9
w_{abs} (μm)	1.0	1.0	1.0	1.0	1.0	1.0
t_{abs} (nm)	20	20	20	20	20	20
A_C (mm^2)	0.83	0.51	0.53	0.26	0.27	0.34
f_0 (MHz)	46	52	63	71	78	74
L (nH)	441	553	368	573	464	404
C (pF)	27	17	18	9	9	11
Q_i	3.9×10^4	3.1×10^4	2.2×10^4	2.3×10^4	1.8×10^4	1.4×10^4
A_{Live}/A_{Pixel}	0.75	0.75	0.75	0.75	0.75	0.75
N_{Pixel}	658	658	2632	2632	10528	10528
J_c (mA/μm^2)	4.5	4.5	4.5	4.5	4.5	4.5
J (mA/μm^2)	0.85	0.65	0.61	0.47	0.44	0.43
$\frac{df/f}{dP}$ (W^{-1})	6.4×10^7	3.4×10^7	4.2×10^7	3.1×10^7	3.1×10^7	2.7×10^7
E (V/m)	2770	2959	2238	3050	2514	2059
$S_{\delta f/f}$ (Hz^{-1})	8.6×10^{-19}	1.3×10^{-18}	1.7×10^{-18}	2.5×10^{-18}	2.9×10^{-18}	2.8×10^{-18}
n_{qp} (μm^{-3})	2700	3050	3700	3200	3900	5000
τ_{eff} (μs)	1.8	1.6	1.3	1.5	1.3	1.0
NEP$_{ph}$ (aW Hz$^{-1/2}$)	37	69	76	92	118	172
NEP$_r$ (aW Hz$^{-1/2}$)	25	43	43	47	51	62
NEP$_g$ (aW Hz$^{-1/2}$)	2.4×10^{-4}	3.7×10^{-4}	3.0×10^{-4}	3.8×10^{-4}	3.4×10^{-4}	3.2×10^{-4}
NEP$_d$ (aW Hz$^{-1/2}$)	3.4	5.5	5.0	5.8	5.8	6.2
NEP$_{amp}$ (aW Hz$^{-1/2}$)	6.0	14	16	21	27	38
NEP$_{TLS}$ (aW Hz$^{-1/2}$)	14	34	31	51	55	61
NEP$_{fund}$ (aW Hz$^{-1/2}$)	45	82	87	103	129	183
NEP$_{Tot}$ (aW Hz$^{-1/2}$)	47	89	93	115	140	193
NEFD (mJy s$^{1/2}$)	1.8	2.2	2.4	2.6	5.6	8.1

Table 4.2: Results of optimization.

4.2 Fundamental tradeoff

We find that the fundamental tradeoff in our design lies between the filling fraction of live area in the focal plane and TLS noise. Individual detector sensitivity is maximized (NEP minimized)

when fundamental noise dominates over TLS and amplifier noise. The TLS noise contribution to the individual detector NEP goes down as the capacitor area increases, but this also increases the dead fraction of the focal plane and thus reduces mapping speed. Figure 4.9 demonstrates such a tradeoff.

It is worth pointing out that the readout power could be increased by a good amount (factor of 5 to 10 in J and so 25 to 100 in P_{read}), which would then reduce TLS noise contribution by a large amount and push toward larger fill factor.

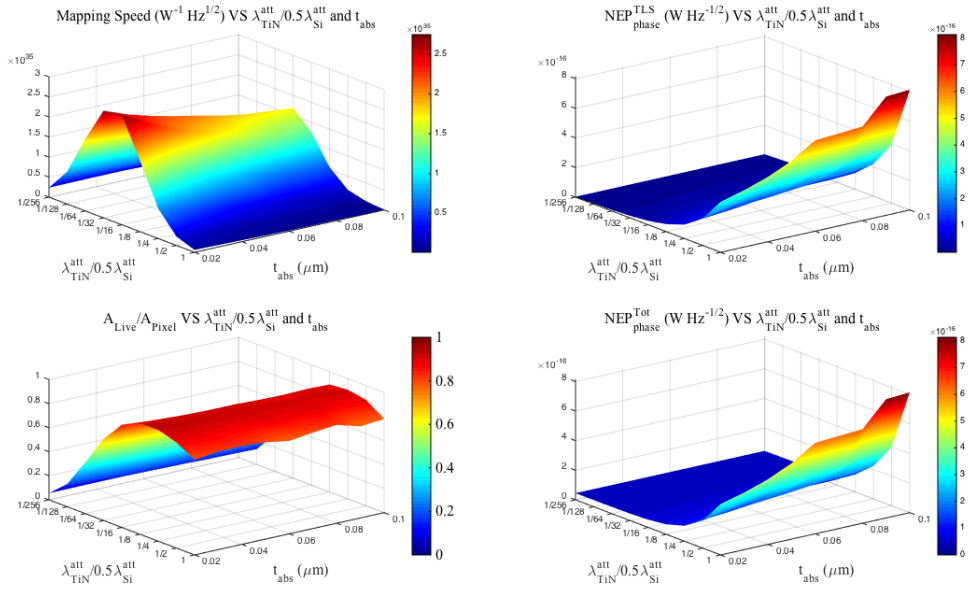

Figure 4.9: Tradeoff between filling fraction of live area and TLS noise.

Chapter 5

Conclusion and outlook

Future observational astronomy in the sub-millimeter/millimeter regime will demand a large format of array of pixels, generally with $10^5 \sim 10^6$ or more detectors. The kinetic inductance detector (KID) being actively developed over the past decade provides a promising route to easy and cheap multiplexing. This thesis explores 1) the physical mechanism of two level system (TLS) noise, the dominant limiting factor of KID's sensitivity and 2) designs the interface that efficiently couples the sub/millimeter photons collected at the antenna to the KID made of highly resistive material TiN for simultaneously six wide continuous bands, as required by the study of dusty star-forming galaxy population and galaxy clusters.

Chapter 2 starts from the microscopic model[8] of dielectric constant based on the independent TLS assumption, derives the frequency noise spectral density resulting from the TLS-phonon bath coupling and checks its dependence on the noise frequency, amplitude of the electric field in the KID capacitor, as well as the system temperature, all of which have already been extensively calibrated experimentally. A certain level of consistency between the model and data is found. However, in-depth examination uncovers the incorrectness of the model and the demonstrated consistency is speculated to be merely coincidence. The study of noise spectral density from a single independent TLS might require numerical simulation of long time series of its dipole moment. Furthermore, recent literature indicates that TLS-TLS interaction via strain field might be the actual origin of TLS noise, and quantitative characterization of the noise strength has yet to be developed[11, 12, 13].

Chapter 3 describes in detail the millimeter wave photon coupling architecture from the antenna to KID. The output of the antenna, a Nb microstrip, is generally in a huge impedance mismatch with TiN, the material that generates the best responsivity of KID to date in the traditional coupling scheme as in MUSIC[14]. In order to reconcile such a discrepancy, an adiabatic, efficient, and flexibly tunable (to accommodate six spectral bands simultaneously) coupling method must be invented.

We performed a thorough study of the absorption process of millimeter wave power and verified the absorption efficiency in the novel coupling scheme both analytically and numerically with finite element software Sonnet[34]. The shortcoming of such a design lies in the complexity of the geometry consisting of five layers of metal and dielectric material, which might present significant problems in terms of device yield. Further systematic experiments under optical loading need definitely to be carried out as the ultimate justification of the design viability.

Chapter 4 derives the physical dimensions of the TiN absorber/inductor, KID capacitor, and readout coupling capacitor, which were used in chapter 3, for the six spectral bands by performing an optimization pivoting around the goal of maximizing the mapping speed. Important independent parameters investigated include the length, width, millimeter wave power attenuation length, and quasi-particle density of the TiN absorber/inductor. The solution ensures an absorption efficiency of millimeter wave power over 80% and a noise equivalent power close to background-limited performance without any risk of bifurcation.

In conclusion, we have successfully achieved all the initial design expectations of the long wavelength imager (LWCam) proposed for CCAT in 2012 by developing the KID technology. We hope the design work can be validated by future experiments.

Bibliography

[1] I. I. Zinchenko, "Contemporary millimeter- and submillimeter- wave astronom," *Radiophysics and Quantum Electronics*, vol. **46**, nos. 8-9, 577-593 (2003).

[2] A. W. Blain, I. Smail, R. J. Ivison, J. P. Kneib, and D. T. Frayer, "Submillimeter galaxies," *Phys. Rep.*, **369**, 111 (2002).

[3] M. Zemcov et al, "High Spectral Resolution Measurement of the Sunyaev-Zel'dovich Effect Null with Z-Spec," *Astrophys. J.*, 749, 114.

[4] A. Pénin, O. Doré, G. Lagache, and M. Béthermin, "Modeling the evolution of infrared galaxies: clustering of galaxies in the cosmic infrared background," *Astron. Astroph.* **537**, A137/1 (2012).

[5] J. McMahon, J. Beall, D. Becker, H. M. Cho, R. Datta, A. Fox, N. Halverson, J. Hubmayr, K. Irwin, J. Nibarger, M. Niemack, and H. Smith, "Multi-chroic feed-horn coupled TES polarimeters," *J Low Temp Phys* **167**, 879 (2012).

[6] P. K. Day, H. G. LeDuc, B. A. Mazin, A. Vayonakis, and J. Zmuidzinas, "A broadband superconducting detector suitable for use in large arrays," *Nature* **425**, no. 6960, 817-821 (2003).

[7] J. Zmuidzinas, "Superconducting microresonators: physics and applications," *J. Annu. Rev. Condens. Matter Phys.* **3**, 169 (2012).

[8] J. Gao, "The physics of superconducting microwave resonators," PhD thesis, California Institute of Technology (2008).

[9] J. Gao, M. Daal, J. M. Martinis, A. Vayonakis, J. Zmuidzinas, B. Sadoulet, B. A. Mazin, P. K. Day, and H. G. Leduc, "A semiempirical model for two-level system noise in superconducting microresonators," *Applied Physics Letters* **92**, 212504 (2008).

[10] O. Noroozian, J. Gao, J. Zmuidzinas, H. G. LeDuc, and B. A. Mazin, "Two-level system noise reduction for microwave kinetic inductance detectors," *AIP Conf. Proc*, 1185, 148 (2009).

[11] J. Burnett, L. Faoro, I. Wisby, V. L. Gurtovoi, A. V. Chernykh, G. M. Mikhailov, V. A. Tulin, R. Shaikhaidarov, V. Antonov, P. J. Meeson, A. Ya. Tzalenchuk, and T. Lindström, "Evidence for interacting two-level systems from the 1/f noise of a superconducting resonator," *Nat. Commun.* **5**, 4419 (2014).

[12] L. Faoro and L. B. Ioffe, "Interacting tunneling model for two-level systems in amorphous materials and its predictions for their dephasing and noise in superconducting microresonators," *Phys. Rev. B* **91**, 014201 (2015).

[13] L. Faoro and L. B. Ioffe, "Internal loss of superconducting resonators induced by interacting two-level systems," *Phys. Rev. Lett.* **109**, 157005 (2012).

[14] S. Golwala et al., "Status of MUSIC, the multiwavelength sub/millimeter Inductance camera," *Proceedings SPIE-the International Society of Optical Engineering*, vol. **8452** (2012).

[15] L. J. Swenson et al, "MAKO: a pathfinder instrument for on-sky demonstration of low-cost 350 micron imaging arrays," *Proceedings SPIE-the International Society of Optical Engineering*, vol. **8452** (2012).

[16] C. M. McKenney et al, "Design considerations for a background limited 350 micron pixel array using lumped element superconducting microresonators," *Proceedings SPIE-the International Society of Optical Engineering*, vol. **8452** (2012).

[17] E. Shirokoff et al, "MKID development for SuperSpec: an on-chip, mm-wave, filter-bank spectrometer," *Proceedings SPIE-the International Society of Optical Engineering*, vol. **8452** (2012).

[18] E. Shirokoff et al, "Design and performance of SuperSpec: an on-chip, KID-based, mm-wavelength spectrometer," *J Low Temp Phys* **176**, 657 (2014).

[19] B. A. Mazin, M. E. Eckart, B. Bumble, S. Golwala, P. K. Day, J. Gao, and J. Zmuidzinas, "Optical/UV and X-Ray microwave kinetic inductance strip detectors," *J Low Temp Phys* **151**, 537 (2008).

[20] S. Golwala, J. Gao, D. Moore, B. Mazin, M. Eckart, B. Bumble, P. Day, H. G. LeDuc, and J. Zmuidzinas, "A WIMP dark matter detector using MKIDs," *J Low Temp Phys* **151**, 550 (2008).

[21] D. C. Moore, S. R. Golwala, B. Bumble, B. Cornell, P. K. Day, H. G. LeDuc, and J. Zmuidzinas, "Position and energy-resolved particle detection using phonon-mediated microwave kinetic inductance detectors," *Applied Physics Letters* **100**, 232601 (2012).

[22] W. A. Phillips, "Tunneling states in amorphous solids," *Reports on Progress in Physics* **50**, 1657-1708 (1987).

[23] T. A. Brun, "A simple model of quantum trajectories," *Am. J. Phys.* **70**, 719 (2002).

[24] J. Dalibard, Y. Castin, and K. Mølmer, "Wave-function approach to dissipative processes in quantum optics," *Phys. Rev. Lett.* **68**, 580 (1992).

[25] K. Mølmer, Y. Castin, and J. Dalibard, "Monte Carlo wave-function method in quantum optics," *JOSA B* **10**, 3, 524-538 (1993).

[26] S. M. Tan, "A computational toolbox for quantum and atomic optics."

[27] S. Kumar, P. Day, H. LeDuc, B. Mazin, M. Eckart, J. Gao, and J. Zmuidzinas, "Frequency noise in superconducting thin-film resonators," *APS March Meeting abstract* (2006).

[28] J. Gao, J. Zmuidzinas, B. A. Mazin, P. K. Day, and H. G. LeDuc, "Noise properties of superconducting coplanar waveguide microwave resonators," *Applied Physics Letters* **90**, 102507 (2007).

[29] S. Kumar, J. Gao, J. Zmuidzinas, B. A. Mazin, H. G. Leduc, and P. K. Day, "Temperature dependence of the frequency and noise of superconducting coplanar waveguide resonators," *Applied Physics Letters* **92**, 123503 (2008).

[30] J. L. Black and B. I. Halperin, "Spectral diffusion, phonon echoes and saturation recovery in glasses at low temperature," *Phys. Rev. B* **16**, 2879 (1977).

[31] H. G. Leduc et al, "Titanium nitride films for ultrasensitive microresonator detectors," *Applied Physics Letters* **97**, 102509 (2010).

[32] Z. Dridi, B. Bouhafs, P. Ruterana, and H. Aourag, "First-principles calculations of vacancy effects on structural and electronic properties of TiC_x and TiN_x," *J. Phys.: Condens. Matter* **14**, 10237 (2002).

[33] M. Calvo et al, "Niobium silicon alloys for kinetic inductance detectors", *15th International Workshop on Low Temperature Detectors (LTD15)*, Jun 2013, Pasadena, United States. **176**, 518 (2014).

[34] C. Ji, A. Beyer, S. Golwala, and J. Sayers, "Design of antenna-coupled lumped-element titanium nitride KIDs for long-wavelength multi-band continuum imaging," *Proceedings SPIE-the International Society of Optical Engineering*, vol. **9153** (2014).

[35] J. A. Schlaerth et al, "The status of MUSIC: a multicolor sub/millimeter MKID instrument," *J Low Temp Phys* **167**, 347 (2012).

[36] Benjamin A. Mazin et al, "Thin film dielectric microstrip kinetic inductance detectors," *Applied Physics Letters* **96**, 102504 (2010).